Aalto University
School of Chemical
Engineering

SCHOOL OF CHEMICAL ENGINEERING

Master's Programme in Chemical, Biochemical and Materials Engineering

Paavo Raittinen

MICROFABRICATED SINGLE-CELL CAPTURE TECHNOLOGY

Diplomityö, joka on jätetty opinnäytteenä tarkastettavaksi diplomi-insinöörin tutkintoa varten Espoossa 21.05.2018

Valvoja: Professori Sami Franssila

Ohjaaja: FT Ville Jokinen

Tekijä Paavo Raittinen

Työn nimi Mikrotyöstetty yksittäisen solun erotteluteknologia

Korkeakoulu Kemian Tekniikan Korkeakoulu

Professuuri Materiaalitiede (CHEM3025)

Valvoja Sami Franssila

Ohjaaja Ville Jokinen

Päiväys 18.5.2018 **Sivuja** 75 **Kieli** Englanti

Tiivistelmä

Yksittäisen solun ribonukleenihapon (RNA) analyysi on mahdollinen seuraavan sukupolven teknologia, jonka avulla genotyyppi on mahdollista määritellä yhden solun tarkkuudella. Avain kriteerinä yksittäisen solun analyysissä on ensin erotella yksittäinen solu solupopulaatiosta. Kaksi tämän hetken lupaavinta teknologiaa yksittäisen solun erottelemiseen perustuvat mikrofluidistiikkaan ja rinnakkaisiin mikrokaivoihin. Tässä työssä kehitettiin uusi lähestymistapa yksittäisen solun erottelemiseen. Menetelmä perustuu kostumiseen ja mikrotyöstöllä valmistettuun kuvioituun pii ja musta-pii pintaan. Yksittäisen solun erottelemiseen valmistettu laite valmistettiin ja sen toimivuutta tutkittiin onnistuneesti. Laitteen ja sitä varten kehitetyn protokollan avulla saavutettiin jopa 30 %:n yksittäisen soluerottelun tehokkuus. Lisäksi eroteltujen solujen joukossa yhtä useampia soluja oli lähes 0 %. Kuvioidun pinnan muototekijä osoittautui kriittiseksi parametriksi, jonka avulla pystytään varmistamaan, että eroteltujen solujen joukossa on vain yksittäisiä soluja.

Avainsanat soluerottelu, kuvioitu hydrofiilinen hydrofobinen pinta, musta pii, yksittäisen solun analyysi

Author Paavo Raittinen

Title of thesis Microfabricated Single-Cell Capture Technology

Department Chemistry and Materials Science

Professorship Materials science (CHEM3025)

Thesis supervisor Sami Franssila

Thesis advisor / Thesis examiner Ville Jokinen

Date 18.5.2018 **Number of pages** 75 **Language** English

Abstract

Single cell ribonucleic acid (RNA) analysis is a next generation sequencing method where the genotype is defined in a single cell resolution. First criteria in single cell analysis is to capture precisely single cell for analysis. Two most promising capture methods are based on microfluidic devices, and microwell array. In this work, a new approach to single cell capture is investigated. The method is based on wetting and microfabricated patterned silicon and black silicon surfaces. The single cell capture device was successfully fabricated and tested. The device and protocol developed here reached up to 30 % single cell capture rate with almost zero double cells captured. The size factor of the patterned shape was found to be robust parameter controlling that only single cells were captured.

Key words cell capture, patterned hydrophilic hydrophobic surfaces, black silicon, single cell analysis

Acknowledges

First, I would like to thank the supervising Professor Sami Franssila for giving me the opportunity to work in his research group and with this ambitious thesis topic. The multiple group and one-on-one discussions with him has been extremely fruitful and insightful in my way towards a research scientist. Second, I would like to thank my thesis advisor Dr. Ville Jokinen who tirelessly guided me through this process. I appreciate that he trusted me to work independently, but whenever I needed discussion and guidance, he and his brilliance was available. The discussions always took the work forward and he had an amazing ability to pick only the relevant points from my sometimes unconstructed narrative. Of course I would like to thank the entire Microfabrication group and its brilliant people, whom I have had a privilege to share discussions, laughs, and ideas. It truly felt like home for the moment.

I would also like to address special thank you to MSc. Pinja Elomaa, with whom I had privilege to work with. Her deep knowledge about cell biology and genetics enabled this thesis to achieve entirely another level. Her time and interest invested in this project is something which I am deeply grateful. Dr. Päivi Saavalainen and Dr. Benedek Poor has also been a key part of this project, thank you. Finally, I would like to thank the courageous director of Micronova cleanroom Mika Koskenvuori, who allowed us to take living cells inside the cleanroom, which truly was a key decision, making this thesis experiment part better. Without the Micronova cleanroom, this thesis would not have happened in this scale and quality.

Of course, I would like to thank my significant other, BSc. Viveka Vihavainen who has nothing but supported me in my pursue to become a research scientist. When I don't believe in myself, somehow you always do, which is something that I am extremely grateful about.

Table of Contents

1. Introduction

Single-cell analysis is an emerging ribonucleic acid (RNA) sequencing technology which aims to genotype cells in a single cell level instead of genotyping cells in a population level [1]. A cell population sample usually demonstrates inter-cellular heterogeneity in terms of genetic composition, which is not detected in non-single-cell RNA sequencing [2]. A scenario where the increased resolution can be relevant is cancer cell analysis [3]. As a disease, cancer usually displays non-aggressive and aggressive subtypes and within these subtypes, the cells often demonstrate genetic heterogeneity as well [4, 5]. Consequently, the single-cell resolution RNA sequencing of these genetic subtypes can provide new understanding about cancer cell immune system leading towards targeted and effective cancer drugs [6].

The initial step in single-cell analysis is single-cell capture. The capture protocol can be manual one-by-one picking, or high throughput capturing isolating thousands of single-cells in one run making practical applications possible. Current high throughput single-cell capture technologies are based either on microwells or microfluidics. In the microwell approach, cells are captured into microwells by placing a cell suspension on top of a microwell array and consequently cells sediment into individual wells. Microfluidics based single-cell capture is achieved by confining single-cells inside a water droplet in an emulsion of oil and water using microfluidic chips and micropumps. The main benefit of microfluidic based single cell capturing is minimal cell-to-cell cross contamination, while it suffers from poor capture rate [7, 8]. Microwell approach demonstrates better capture rate, but it suffers from cell-to-cell RNA cross contamination [7, 9, 10]. From the single cell analysis perspective, the cross contamination might weight more than capture rate, since it directly effects to the reliability of the single cell analysis results [9].

In this thesis, a new alternative approach to achieve single cell capture is investigated. A device based on patterned hydrophilic and hydrophobic black silicon and patterned planar silicon surface is developed and tested. The well-established wetting physics works as the theoretical foundation behind this approach, while array of well-defined microfabrication techniques and silicon micromanipulation methods are harnessed to fabricate the device.

Our single-cell capture device developed here proved successful concept and outperformed some of the current microwell based technologies in terms of single-cell capture rate. We show that the single-cell isolation can be robustly controlled by adjusting the

pattern size to correspond the cell size with simple design rule. Furthermore, we have developed a predictive stochastic model to provide insight to the underlying random element in the single-cell isolation process using patterned hydrophilic and hydrophobic surfaces.

2. Theoretical background

2.1. Wetting

Wetting is a fundamental every-day phenomenon visually observable, and sensational via skin contact. A common scenario is a single drop of water falling on a solid, rigid substrate, such as a common kitchen sink table, the moment before contact, the water droplet topology resembles spherical shape while surrounded by air; however, after the initial contact with solid plane, it begins to deform towards some different topology, flat, in this example scenario. What seems like an arbitrary deformation at first, is in fact well defined and deterministic process.

Two most fundamental concepts in water-solid surface wetting context are hydrophobicity and hydrophilicity. The solid phase in the previously presented kitchen-sink example demonstrates hydrophilic nature, which means that it offers such conditions to the system that water droplet preferably deforms and spreads on the surface. Hydrophobic is the opposite case, where the solid phase sets such conditions that the water droplet will retain *some* of its spherical topology more preferentially than completely spreading, sticking, and flattening to the surface. However, rather than being binary wet – do-not-wet state, wetting is dynamic phenomenon and is most commonly described in terms of contact angle θ_{CA} [11]. Contact angle is the angle between the solid normal and tangent of principal arc of sessile water droplet at solid-liquid-vapour contact point [11]. In general, a surface is hydrophilic when static $\theta_{CA} < 90^{o}$ and hydrophobic when static $\theta_{CA} > 90^{o}$; extreme cases are termed superhydrophobic and superhydrophilic, when static $\theta_{CA} > 150^{o}$ [11] and static $\theta_{CA} \approx 0^{o}$ respectively. Figure 1 below elaborates the concept of contact angle.

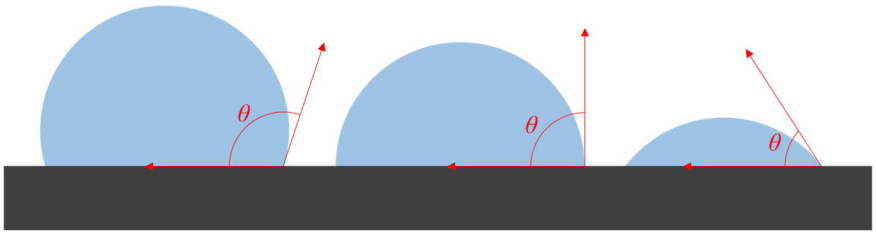

Figure 1: Left droplet displays contact angle > 90°, middle droplet displays contact angle = 90°, and right droplet shows contact angle < 90°.

In addition to static contact angle, so-called advancing $\theta_{Adv.}$ and receding $\theta_{Rec.}$ contact angle defines minimum and maximum contact angle of a droplet. Advancing contact angle is defined at point when adding more liquid to a drop, the droplet contact line does

not move (advance): the maximum is reached *just* before the droplet contact line begins to advance if more liquid is added. Similarly, receding contact angle is defined as the point *just* before when removing liquid from the droplet causes the pinned contact line to recede. The difference θ_{Adv} - θ_{Rec} is referred as contact angle hysteresis [11].

The underlying physics of wetting is surface tension, and thermodynamic tendency towards minimal energy. An individual molecule inside the liquid bulk undergoes cohesive interaction with its neighbouring molecules, while molecules on the surface lose half of their cohesive interactions, which is the primary cause why liquid adjust its topology to reach smallest possible surface area [11]. More precisely, let the cohesive energy of a bulk molecule be u_I, then energy of surface molecule is approximately $u_I/2$; the surface tension is a measure of this energy shortfall per unit surface area [11]. Essentially, surface tension is a molecular level phenomenon, which is often not directly measured. Instead, to describe surface wetting properties the observed contact angle is measured [11, 12]. The interfacial tensions between vapour, liquid, and solid phase at the line of contact defines the magnitude of contact angle, which is formulated for an ideal surface as *Young's Law:*

$$\cos\theta_{CA} = \frac{\gamma_{SV} - \gamma_{SL}}{\gamma_{LV}} \quad (1)$$

Young's Law states that cosine of contact angle is ratio of surface tensions γ_{ij} between solid (S), liquid (L), and vapour (V) interfaces. Theoretically, contact angle could be predicted with Young's Law should the knowledge of interface tension between the phases be available. However, Young's law was derived as early as 1805 and assumes an ideal surface [13]. More recently (1964) Johnson and Dettre studied the effect of surface roughness to contact angle [14, 15]. In their experiment, water droplets were generated on wax surfaces and contact angles measured. The key finding was that as surface roughness increases, the contact angle increases as well; furthermore, the difference between advancing and receding contact angle is high at low surface roughness, while the contact angle hysteresis nearly vanishes at high surface roughness region [14, 15].

2.2. Wenzel model and Cassie-Baxter model

Prior to Johnson and Dettre, improvements to understand wetting on surfaces was suggested by Wenzel and Cassie and Baxter where surfaces would no longer be ideal. Wenzel's model assumes chemically homogeneous rough surface and that local contact angle at *dx* is governed by Young's law (equation 1), while the aim is to explain the apparent

(global) contact angle θ'_{CA}. The surface roughness r on local surface energy dE is defined by:

$$dE = r(\gamma_{SL} - \gamma_{SV})dx + \gamma_{LV}dx\cos\theta'_{CA} \quad (2)$$

This simplifies back to Young's Law on smooth surfaces ($r = 1$):

$$\cos\theta_{CA} = \frac{\gamma_{SV} - \gamma_{SL}}{\gamma_{LV}}, when\ r = 1 \quad (3)$$

And finally to Wenzel's relation when surface is rough ($r > 1$):

$$\cos\theta'_{CA} = r\cos\theta_{CA}, when\ r > 1 \quad (4)$$

Wenzel's relation (equation 4) states that surface roughness r magnifies the wetting behaviour whether the solid surface demonstrates hydrophilic or hydrophobic nature. Wenzel model also assumes that liquid-solid contact interface is a continuous and conformal along the physical liquid droplet and solid surface, wetting all the trenches. Such state is referred as *Wenzel state,* illustrated in figure 2.

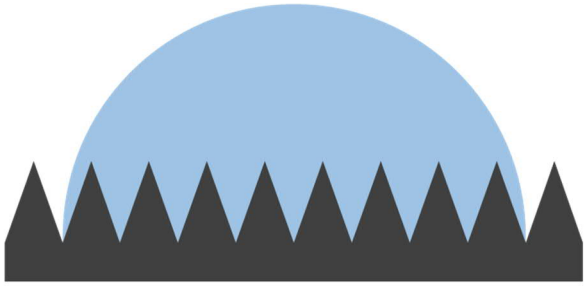

Figure 2: Liquid droplet in Wenzel state on a rough surface.

Nevertheless, Wenzel's relation is limited to chemically homogeneous rough surfaces only. The Cassie and Baxter model extends Wenzel's model to chemically heterogeneous and porous surfaces [16]. To determine the apparent contact angle on a solid surface consisting of two components, the area fraction a_1 and a_2 of each two component have to be taken into account, such that $a_1 + a_2 = 1$. Cassie-Baxter relation states that the energy difference between differentially small displacements dx is:

$$dE = a_1(\gamma_{SL,1} - \gamma_{SV,1})dx + a_2(\gamma_{SL,2} - \gamma_{SV,2})dx + \gamma_{LV}dx\cos\theta' \quad (5)$$

The area fraction a_1 and a_2 can be interpret as probabilities how likely the liquid droplet encounters with either solid phase. Applying Young's Law and considering minimum energy E_{min}, the equation 5 reduces to Cassie-Baxter relation of apparent contact angle θ':

$$\cos\theta' = a_1 \cos\theta_1 + a_2 \cos\theta_2 \quad (6)$$

Now, considering a heterogeneous surface case where solid substrate contains open holes "filled" with air, then area fraction of the solid is a_1 and area fraction of air is a_2. With appropriate conditions, the liquid droplet does not fill the holes, but forms liquid-air interface(s); such state is referred as Cassie-Baxter state. Contrary to Wenzel's state, a droplet in Cassie-Baxter state tends to rest on top of solid pillars while leaving air gaps between the trench and the liquid droplet. Figure 3 illustrates liquid droplet with contact angle > 90° in a Cassie-Baxter state on a heterogeneous solid surface:

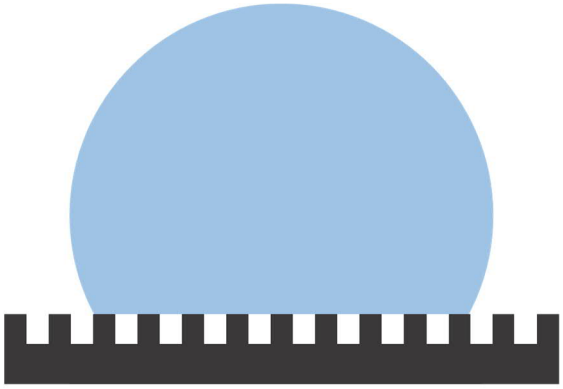

Figure 3: Liquid droplet in Cassie-Baxter state on a rough surface.

Furthermore, the contact angle between water and air is 180° [17]; however, according to Cassie-Baxter relation, such contact angle is impossible, since some part, even infinitesimally small, of the heterogeneous surface is always solid even if only the very tip of the pillar(s) form solid-liquid interface with the droplet. Besides, it can be argued that 180° contact angle really is not in contact with any surface, since no interface exists between the two.

2.3. Natural and artificial hydrophobic surfaces

In the case of hydrophobic and superhydrophobic surfaces, the Cassie-Baxter relation can be interpreted such that it suggests minimizing the solid-liquid contact area and maximising liquid-vapour contact area. To achieve such optimization, the surface topography must be controlled. A famous biological example of superhydrophobic surface is the so-called lotus effect, which stems from the observed phenomenon of self-cleaning. Self-cleaning refers to a situation where water droplet rolls on a superhydrophobic surface, and when encountering an adparticle, the adparticle migrates into the water droplet and both roll off from the surface. With the droplet, the motivation from the perspective of

plant is to ensure sunlight gain and to mitigate any heavy burden. However, the underlying enabler is the *ingenious* surface topography. Scanning electron microscope (SEM) images collected in figure 4 below reveals the microstructure of a lotus leaf (adopted from [18]:

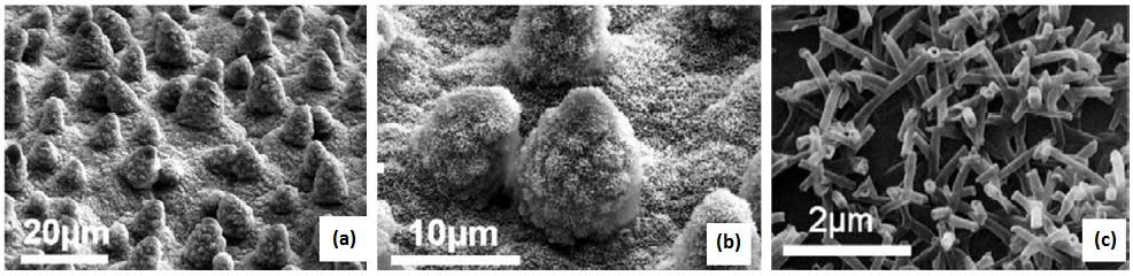

Figure 4: a, b) SEM images of a lotus leaf showing ordered cone-like structures on the surface. c) Increased magnification reveals smaller microstructure (wax tubules) covering the cone-like structures. [18]

The surface microstructure demonstrates closely packed "ordered" rough surface as can be observed from figure 4a and 4b. However, in addition to rough microstructure, the lotus leaf shows even smaller microstructure displayed in figure 4c, on top of cone-like structures, called cell papillae, displayed in figures 4a and 4b, i.e., lotus leaf shows hierarchical structure. The constituents of the smaller microstructure in figure 4c are so-called epicuticular wax tubules, which demonstrates high water repellency due to their chemical composition [19], thus representing the chemically hydrophobic part of the lotus leaf surface. Moreover, Koch *et al.* conducted series of tests aiming to artificially replicate lotus leaf hierarchical structure and found out that flat silicon covered with lotus leaf wax tubules demonstrated static contact angles of only 119°, while lotus leaf itself shows static contact angles > 160° [20].

In their next attempt to mimic Lotus leaf structures, they used a moulding technique where micropatterned Si worked as a master template (14 µm diameter, 30 µm height, 23 µm pitch –pillars) to first create so-called negative mold. After that, the negative mold was used to fabricate an epoxy replicate which mimicked Lotus leaf microstructure. In the final step, they used thermal evaporation to cover the replicate surface with wax tubule nanostructure to obtain the final Lotus-like hierarchical microstructure. The resulting replica demonstrated static contact angle of 173° with low (~1°) contact angle hysteresis [18]. Their conclusion is that a hierarchical structure provides the air gap formation, which minimizes the contact area between solid-liquid interfaces. This shows that surface topography acts a key role in terms of achieving hydrophobicity and superhydrophobicity.

One path to fabricate artificial superhydrophobic surfaces is silicon microfabrication, which is well established, studied, and robust microfabrication field [21]. Qi *et al.* [22] fabricated superhydrophobic surfaces via two step anisotropic wet etching process of silicon (Si). Etching with potassium-hydroxide (KOH) provided well defined micropyramid surface due to anisotropic wet etching properties of Si and KOH combination; then, a thin film of silver particles was deposited on Si micropyramids to work as a catalyst, while consequent wet etching in hydrofluoric-acid / hydrogen peroxide solution rendered the pyramid surface "porous". The resulting hierarchical micro-nanostructure exhibited a contact angle of 169°. Contact angles measured from the pyramid structure without the nanostructure demonstrated contact angles of 130° to 157°, giving justification to the extra etching step to reach hierarchical structure to reduce the contact area.

Hierarchical structure can be considered as sufficient but not necessary condition, since solid phase surface area minimization can also be achieved with only a single level nanostructure. Sainiemi *et al.* [23] used cryogenic deep reactive ion etching (cDRIE) to fabricate well defined pyramid nanostructure on silicon. Due to the nanostructured surface topography, the silicon becomes to non-reflective silicon referred to as black silicon (b-Si). As-processed black silicon demonstrates hydrophilicity due to high surface energy (1240 mJ/m^2) of Si [24]; however, consecutive surface polymerization via plasma enhanced chemical vapour deposition (PECVD) using CHF_3 plasma, converts the surface into low-energy (in the range of 19-20 nN/m) fluorocarbon (PTFE) surface demonstrating extremely high static contact angles around 170° due to combination of minimal surface area and low surface energy of the material. It is important to note that the previously described method does not yield hierarchical micro-nanostructures, and instead a single low surface energy nanostructure is formed exhibiting superhydrophobicity. Figure 5 illustrates both microfabrication methods in a schematic fashion (not in scale):

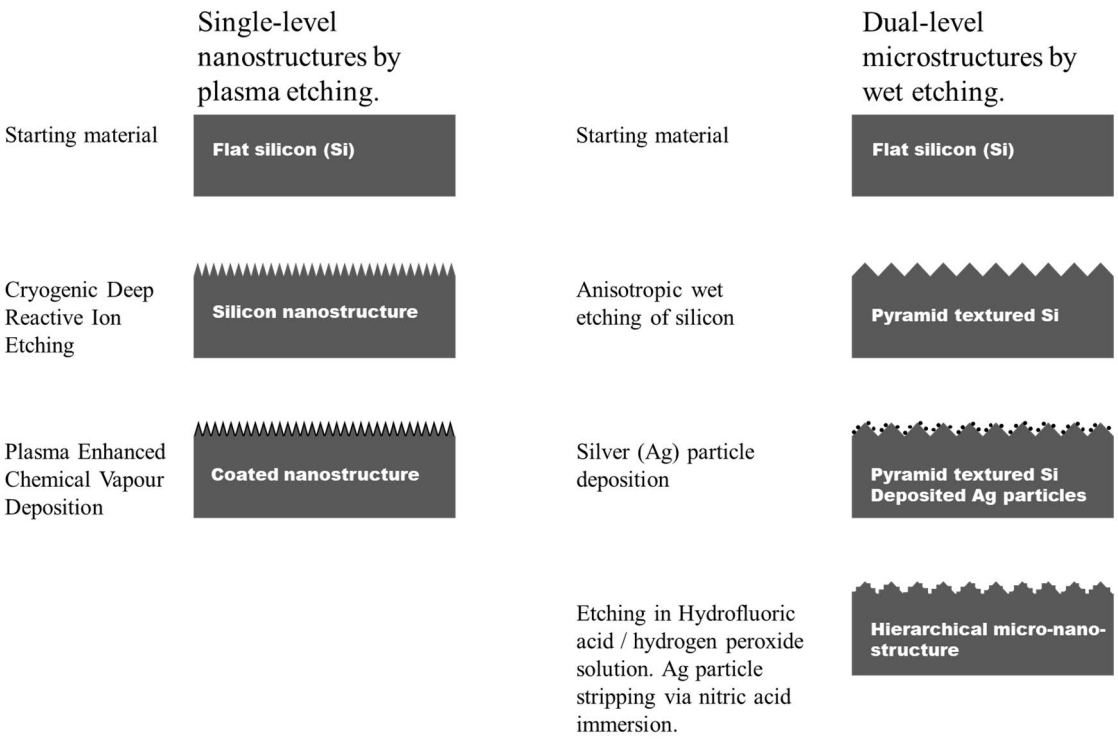

Figure 5: Schematic representation of the process flows governing the hydrophobic surface microfabrication of two different approaches. Left: hydrophobic black silicon surface by Sainiemi et al. [23] Right: hydrophobic silicon surface based on hierarchical micro structure [22].

Typical pyramid width, depicted in figure 5, on b-Si is around one micrometer and height around 1.2 micrometres, and fluoropolymer film thickness around 60 nm; while the pyramids on hierarchical pyramid structure Silicon (hp-Si) are significantly larger at around 6 micrometer wide and 3 to 4 micrometer high (figure 5, right process flow). However, the nanostructure on top of hp-Si is some 200 nanometer high and around 100 nanometer wide. From the microfabrication process flow perspective, two methods illustrated in figure 5 are different mainly due to etching process; b-Si is fabricated via plasma etching, while hp-Si is achieved using chemical wet etching. Furthermore, b-Si fabrication requires one less step in comparison to hp-Si. However, the static contact angles are high (both around 170^{o}) and contact angle hysteresis are low (both around 2^{o}). Finally, figure 6 displays SEM images of as-fabricated b-Si and hp-Si, adopted from the original papers:

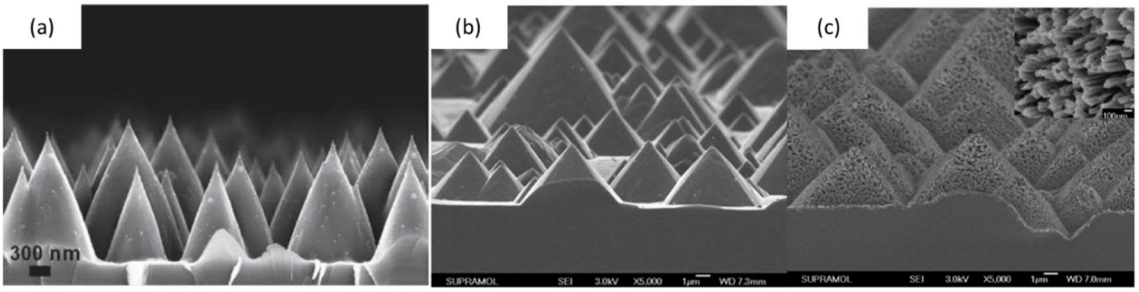

Figure 6: a) hydrophobic black silicon. [23] b) hp-Si surface after first wet etching showing clean pyramid-like shape. c) hp-Si surface after second wet etching displays microcavities on the pyramid structure [22].

Figure 6c (hp-Si) reveals similar hierarchical structure resembling lotus leaf in figure 4, while figure 6a displays fine nanostructure resembling the finer *upmost* structure of lotus leaf rather than hierarchical structure. Furthermore, both surface topographies definitely minimize the solid phase surface area promoting Cassie-Baxter state and air pocket formation, and importantly, both are relatively easy to achieve via well-known and robust microfabrication processes.

2.4. Patterned hydrophilic-hydrophobic surfaces

The idea of hydrophobic and hydrophilic surfaces can be extended to patterned hydrophobic-hydrophilic surfaces, referred now on as HB/HL. Such patterned surface is simply a surface where some of the area is hydrophilic and some of the area hydrophobic. On such surface, water droplet tends to spread and stick onto a hydrophilic area, while the water droplet preferably retains its spherical topology and slides off from the hydrophobic areas.

Since water droplet immobilizes onto hydrophilic surface while remaining mobile on hydrophobic surfaces, it is possible to controllably split water droplets into two, by creating hydrophobic patterns on otherwise hydrophilic surfaces. Song *et al.* presented a droplet splitting method based on narrow (~1 mm) hydrophobic stripes on a hydrophilic surface; when a water droplet is dropped perpendicular to the patterned surface, the hydrophobic stripe functions in a blade-like fashion cutting the so-called mother droplet into daughter droplets due to imbalanced surface tension between hydrophilic and hydrophobic areas. Furthermore, by controlling the size and geometry of the hydrophobic stripes, and the impact point of the water droplet relative to stripes, the secondary droplet volume fractions are extremely well defined [25].

However, patterned hydrophilic-hydrophobic surfaces can be used for droplet splitting in a more high-throughput way as well. By creating and array of hydrophilic areas with well-

defined geometries on a hydrophobic surface and sliding a water droplet on such surface, it is possible to trap well-defined daughter droplets onto such hydrophilic spots. In the sliding droplet case on patterned surfaces, the pinning force acting against the gravitational force (or other force assisting forward motion), is governed by imbalanced Young's force and contact angle hysteresis which can be described by [26]:

$$F_Y = L\gamma_{LV}(\cos\theta_r - \cos\theta_a) \quad (7)$$

In equation 7, L is length of the droplet, γ_{LV} is liquid surface tension, θ_r and θ_a are receding and advancing contact angles respectively. Clearly the pinning force emerges from surface wetting properties and effectively causes the fission of the sliding droplet into smaller droplets. Chang *et al.* measured sliding velocities and deposited daughter droplet volumes on hydrophilic patterns and found out that the distance between hydrophilic spots is a critical factor determining the deposited droplet volume [27]. Furthermore, in a similar endeavour to generate well-defined microdroplets with patterned surfaces, Li *et al.* found that the sliding velocity and the contact force of the droplet affect deposited droplet volume [28]. Furthermore, daughter droplets were strictly confined within hydrophilic areas, while hydrophobic area functioned as a limiting boundary, analogous to coffee cup walls holding liquid exactly inside the cup volume. The predictable behaviour gives confidence in the applicability of the micropattern concept for high accuracy applications.

3. Microarray technologies

3.1. Basics, functional principles, and single cell analysis

Microarray technologies refer to a lab-on-a-chip application where *some reactions* take place simultaneously on a two-dimensional array-like substrate, or *something* is selectively collected on to a specific location(s) in high quantities. Furthermore, microarray is often connected to biomedical context; more specifically it includes, but is not limited to, cellular microarrays, DNA microarrays, and chemical compound microarray [29, 30, 31]. Microarrays are commonly made via silicon microfabrication or by surface functionalising glass or plastic substrate [32, 33].

The main goal of microarrays is simply to enable high-throughput and in-depth analysis. For example, US based company Illumina provides a commercial solution for single nucleotide polymorphism (SNP) analysis capable of reading one million SNP variants per one microarray slide from a single DNA sample [34, 35]. Illumina technology is based on solid substrate surface functionalization; specifically, the surface contains an array of unique counterparts (often referred as tags), or deposition sites, for single nucleotide polymorphisms to bind to. The array-format enables high-throughput analysis while surface functionalization provides the selectivity. Furthermore, the selectivity mechanism should preferably be as robust as possible, since it could be a critical factor affecting to the reliability of the analysis.

Essential goal in single cell analysis is to analyse exactly one cell at the time, i.e., to increase resolution from “bulk” cell population to individual single cell. Motivation to develop single cell analysis technologies stems from the fundamental biological observation of cell population heterogeneity, which is due to random expression of genes and proteins [36]. Due to random gene expression, the true cell population distribution is often unknown. [36]. However, single cell analysis is still relatively nascent technology from the microarray technology perspective.

Single cell analysis could enable new level of understanding of human biomedical state and lead to more precise and individual healthcare. The ability to observe and analyse single cells in high-throughput fashion could replace some heuristic based diagnosis with more accurate means to conduct diagnosis. Such accurate diagnosis could lead to major changes in medical treatment by enabling personalized treatment plan [37], or it could aid

in epidemiological research [38], or even aid with developing new drugs [39]. The following three chapters introduce different single cell array technologies currently under investigation.

3.2. Microwells

Cell array technologies based on microwells refer to a concept where micrometer scale wells are fabricated in an array format on a substrate. Typical substrate material is silicone rubber, polydimethylsiloxane (PDMS), which is commonly used in soft lithography process. PDMS processing is well established and the material itself is flexible, biocompatible, and mouldable [40], making it well suitable material for microwell fabrication, where accurate dimension, spatial control, and biocompatibility are imperative.

The aim of a microwell array is to capture a single cell to each individual microwell, and preferably each microwell contains exactly one cell. However, usually microwell array contains empty wells, wells with single cells, and wells with multiple cells, after cell seeding. Efficiency of microwell device is often measured in terms of occupancy rate, which translates into number of wells containing cells per total number of wells on the array; single cell occupancy rate is simply the ratio of single cells per total number of wells. Typically, cells are seeded in a cell suspension, which is applied on top of a microwell array and let to settle via sedimentation [10].

Two of the most critical parameters to consider in the microwell concept are cell suspension cell concentration and microwell topology. Intuitively, high cell concentration leads to increased probability that a cell would settle into a microwell; however, an optimization study [10] found out that there is little to no effect to occupancy rate after doubling the cell density over well density. The well dimension played a critical role in terms of single cell occupancy rate. For adherent NIH3T3 cells the most optimal microwell dimensions are 25 µm diameter and 27 µm depth, leading to 80 % single cell occupancy rate and 10 % multiple-cell occupancy rate, according to [10]. Typical diameter of an individual NIH3T3 cell is around 14 µm [41] indicating optimal cell diameter to well diameter ratio around 1:2 in both vertical and horizontal dimensions. Figure 7 illustrates common microwell single cell array and corresponding seeding mechanism:

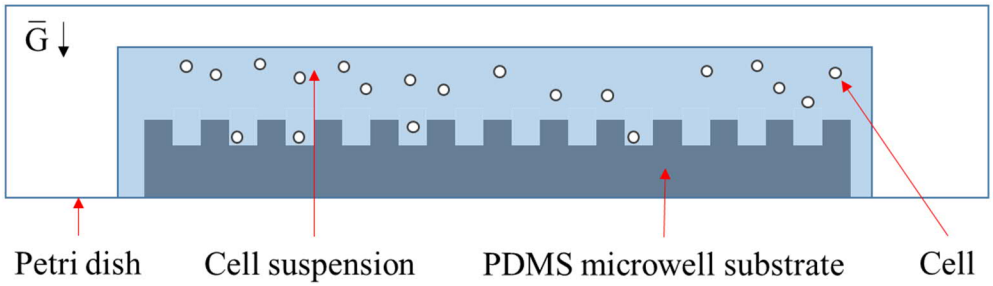

Figure 7: Schematic illustration of a typical microwell array showing few captured cell on the bottom of the well. The cell seeding is gravity assisted – all cells do not necessarily hit their target (single well), or multiple cells hit the same target.

In the microwell array illustration in figure 7, cells and microwells are drawn into scale with respect to each other (considering that cell is NIH3T3 cell, and well dimension adopted from the related study [10]) to elaborate the intuition about cell suspension cell concentration / density and occupancy rate correlation. Clearly a microwell must be designed in such a way that it provides enough space for one cell, while impedes two or more cells fitting inside.

From the single cell analysis perspective, the cell capture is only the initial phase, while consequent phase is to conduct, for example, RNA sequencing to individually genotype captured cells [42, 43]. Bose *et al.* [44] used PDMS microwells successfully for single cell RNA sequencing by initially capturing single cells into microwells using gravity assisted seeding similar to the one used by [10], leading to 10 % single cell occupancy rate and only 0.5 % multiple cell occupancy rate [44]. After the capture, the cells are lysed (killed) in order to release their mRNA by switching the environmental fluid with chemical lysis buffer. Microwells are then sealed with a glass slide to prevent cell-to-cell cross contamination. The glass slide is surface functionalised with oligo(dT) primers which immobilizes the freely flowing mRNA for the actual single-cell analysis [44]. Figure 8 displays a representation of microwell capture device, consequent lysis step, and mRNA printing, introduced in [44]:

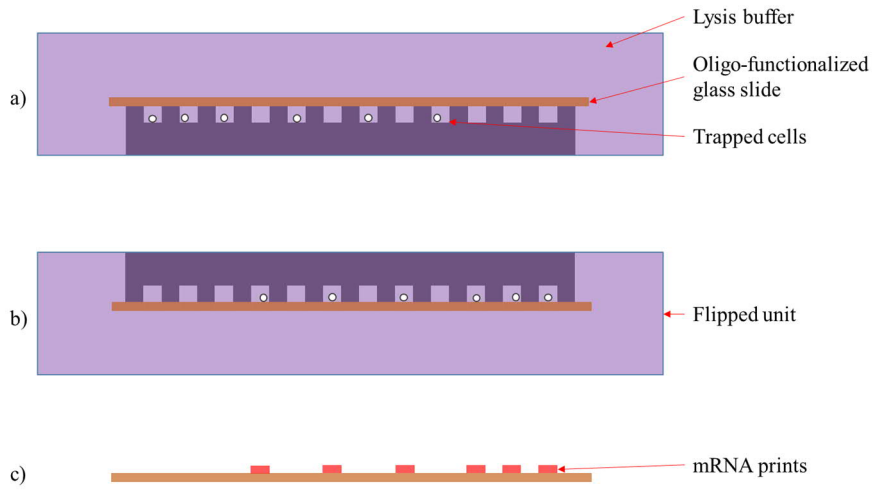

Figure 8: Microwell based single cell capture and analysis workflow. a) The captured single cell are at the bottom of the wells where the cells are chemically lysed. b) Lysed cell have released their mRNA and the unit is flipped which brings them to contact with oligo(dT) functionalized substrate. c) mRNA is attached to the oligo(dT)-functionalized substrate. Schematics are modified from [44].

The critical steps depicted in figure 8 are: a) capture single cell into each well, b) chemical cell lysis to expose mRNA, c) collect mRNA prints to a separate oligo(dT)-functionalised substrate. After that, the mRNA "prints" are ready for reading, i.e., actual single cell analysis. It is essential to mitigate possible inter-cellular contamination after cell lysis, since it would directly affect to the quality of the analysis. [44]

One recent advance in the microwell concept has been introduced by Massachusetts Institute of Technology (MIT) group, dubbed as SeqWell [9]. The unique feature in their concept is the ability to reversibly attach and detach a semi-permeable polycarbonate membrane on top of microwells after cell capture. This feature is achieved with different surface chemistry modification between microwells and the rest of the surface. The inner surface of microwell is functionalised with poly(glutamate) to mitigate non-specific binding of mRNA. The top edge surface is functionalised with chitosan to promote efficient sealing of the microwells, and to enable the detachment of the semi-permeable polycarbonate membrane. The membrane is designed to allow passing of the lysis buffer while retaining the captured cells and released mRNA in each discrete well. Figure 9 illustrates their concept:

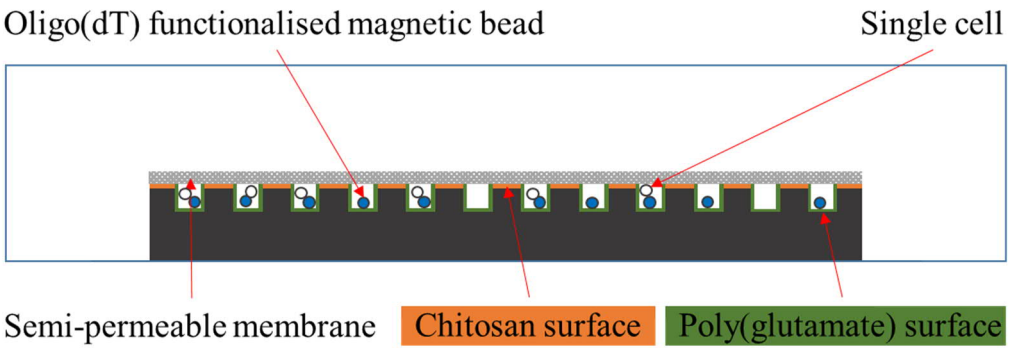

Figure 9: Microwell based single cell capture and analysis device. Oligo tag beads and cells are trapped inside microwells. The semi-permeable membrane prevents cross-contamination between cells during the cell lysis and consequent mRNA collection. Schematic image adapted from [9].

The process begins with magnetic bead loading which is achieved via intermittent rocking. Next, cell suspension is introduced leading to gravity assisted single cell capture with around 17 % single cell occupancy rate out of total number of microwells per array [9]. These steps are followed by attachment of the semi-permeable membrane, and introduction of cell lysis buffer. Semi-permeable membrane provides efficient in-and-out pathway for the cell lysis, while impeding biological macromolecule (including mRNA) migration from the microwell, which in turn prevents well-to-well contamination. The final step is to remove the semi-permeable membrane and collect oligo-functionalised magnetic beads which are now covered with covalently bonded mRNA ready for single cell analysis.

3.3. Droplet microfluidics

Droplet microfluidics may not categorically belong under microarray family technologies; however, droplet microfluidics are also used in similar biomedical context than microarrays are, thus droplet microfluidics is reviewed here under microarray category and mainly discussed from single cell analysis perspective.

The main goal in droplet microfluidics is to generate and manipulate high number of micrometre-sized droplets in a swift manner. Critical components of such device are channels, pumps, and inlets / outlets. The main unit is referred as microfluidic chip which is typically fabricated from PDMS, which benefits from cost-efficiency, moldability, and hydrophobicity. However, in microfluidic context, PDMS may undergo swelling and deformation when strong organic solvents are used, which is a drawback. Thus, glass and silicon are also used as fabrication materials should the application require so [45].

The channel design is most critical in terms of device functionality, since channel width, diameter, and turns affect to the flowrate and the droplet generation aspect. Furthermore,

droplet microfluidics devices usually use two work fluid phases, which form an emulsion, such as water and oil. One is so-called continuous fluid while other is termed as dispersed fluid. This translates in to a situation where either oil droplets are generated into continuous water phase, or vice versa. Typical channel design approaches to induce systematic droplet generation includes T-junction and flow-focusing [45], illustrated in figure 10:

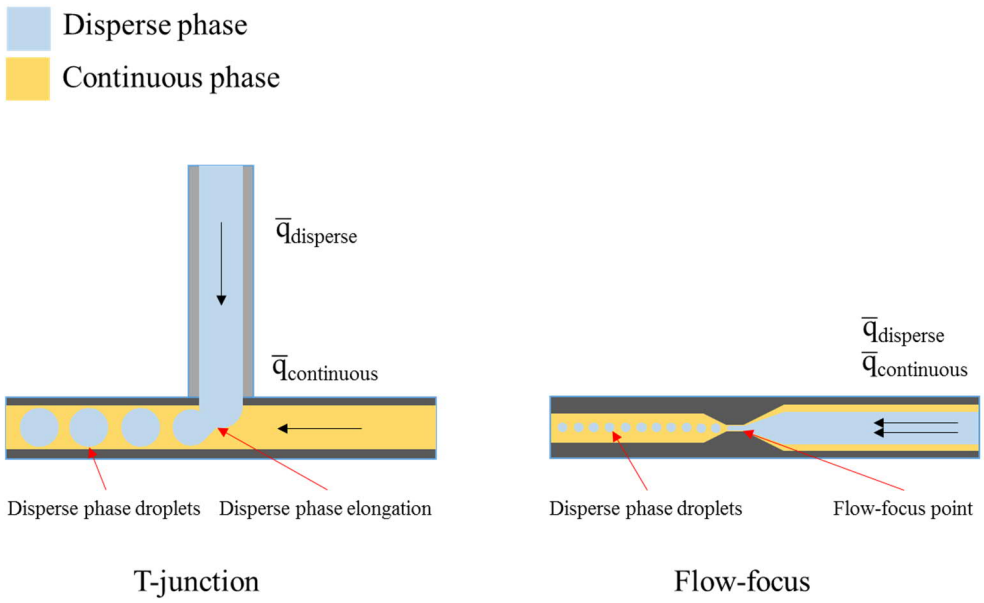

Figure 10: Schematic illustrations of microfluidic droplet generators. Left: droplet generator based on T-junction. Right: droplet generator based on flow-focus point.

In T-junction, the dispersed phase channel is perpendicular to the continuous channel; when dispersed fluid is introduced into the system via channel inlet, it forms an interface with the continuous fluid flow at the T-junction, and consequently begins to elongate along the continuous channel due to shear forces generated by the continuous phase. The dispersed phase fluid elongates along the continuous channel until the droplet neck breaks, resulting in discrete droplet. The droplet size can be adjusted by altering the flowrates of both fluids, tuning the channel geometry in design stage, and adjusting fluid viscosity when that is possible. Furthermore, single microfluidic chip can contain multiple T-junctions with different inlets to enable more complex functions.

Flow-focusing design is also based on harnessing shear forces; however, rather than forcing two perpendicular fluid streams to form an interface, the aim of flow-focusing is to force dispersed and continuous phases through an increasingly narrow cone-like channel to induce symmetric shearing. Before the flow-focusing cone, both phases are continuous,

while at the end-tip of the cone, the middle phase begins to form mono-disperse micro-droplets. Flow-focusing and T-junction design are both based on shear force, thus droplet size is governed by similar parameters in each approach.

Due to its capability to generate mono-disperse micro droplets with high-throughput, droplet microfluidics is a suitable technology for single cell analysis. A noteworthy functional difference between droplet microfluidics and microwells is that while in microwells the capture of the cell, cell lysis, and mRNA harvesting are done sequentially in different unit processes, in droplet microfluidics they are done simultaneously in one focus point, i.e., when the cell, lysis buffer, and oligo tag are within a single "reactor" droplet.

Two separate groups, Zilionis *et al.* [7] and Macosko *et al.* [8], designed and fabricated droplet microfluidic systems for single cell analysis purposes. The carrying idea behind both designs is to pin point and replicate an event where single microfluidic droplet is generated confining a single cell and a single barcoding beads (i.e., oligo(dT) functionalised bead) within. To achieve this, both teams used microfluidic PDMS chips with a combination of T-junctions and flow-focuser units to control the confinement event. The fluid phases used are oil as the continuous phase, and cell suspension and lysis buffer as disperse fluids. Figure 11 illustrates a simplified chip design behind Zilionis *et al.* and Mackosco *et al.* discoveries:

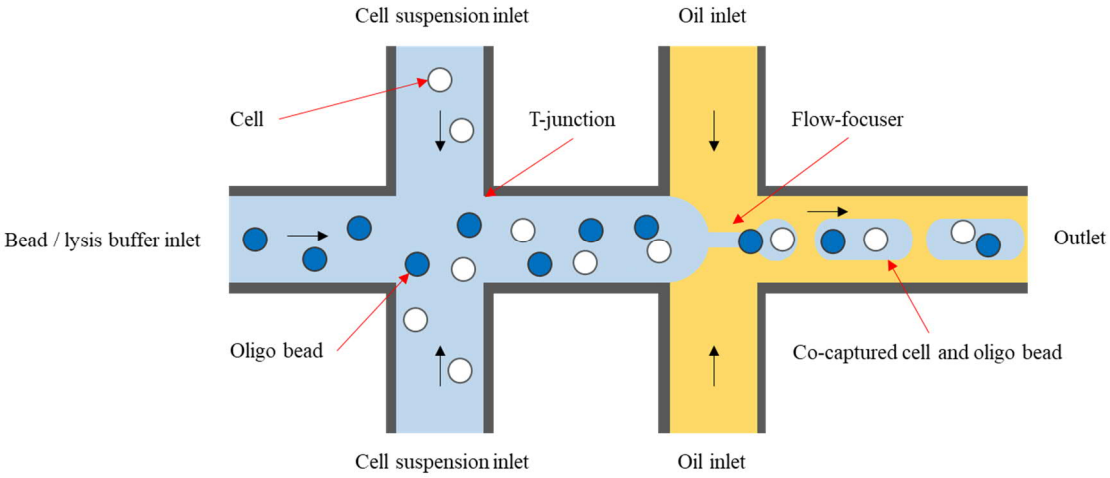

Figure 11: Single cell capture and analysis device based on separate inlets for cell suspension, tag beads and lysis buffer, and oil. Schematic illustration based on work by Macosko et al. [8].

The critical event occurs at the flow-focuser, where cells and beads are confined within one discrete microdroplet. To ensure the co-encapsulation, flowrates and timing are controlled with the help of digitally controlled micropump system [45, 46] while cell / bead concentrations are tuned optimally prior running the process [8, 46]. One of the main

benefit with droplet microfluidics is that the cell capture, bead capture, and cell lysis occurs at the same time and place. The cell and oligo functionalized bead are captured inside one discrete droplet which already contains cell lysis buffer, since it is added into second disperse phase, so the mRNA harvesting begins right after the co-capture. Due to single unit process, it can be argued to be more parallel process in comparison to microwell architecture where cell capture, cell lysis, and mRNA harvesting occur sequentially in separate unit processes.

However, the overall efficiency in terms of occupancy rate is significantly lower when compared to a microwell design. While Macosko *et al.* device is capable of generating more than 100 000 microdroplets per minute, most of the generated droplets are empty, some contain exactly one cell and one bead, few contain only bead or cell, and on rare occasion multiple beads / cells are confined within same microdroplet. Consequently, the single cell and bead occupancy rate can be extremely low, around 0.1 % [8]. Rotem *et al.* claims to have reached 5 % cell and bead occupancy rate with similar microfluidic droplet design [46]. Nevertheless, droplet microfluidics falls behind in terms of occupancy rate in comparison to a microwell design.

For example, Macosko *et al.* device can generate 10^4 droplets containing a cell and a bead enough for RNA sequencing [7], while 10^6 empty droplets may be generated aside; however, the excess empty droplets are not that detrimental. To capture and harvest mRNA from 10^4 cells, the microarray must contain at least 7.0 x 10^4 individual microwells [9], when empty wells are unused, which is not necessarily detrimental either. The previous comparison leads to observation that existing microwell and droplet microfluidic designs are similar in terms of single cell analysis throughput efficiency. However, microwells can capture multiple cells simultaneously, limited (in principle) only by the *n x m* number of wells in the array (analogous to possible scenario of multiple channels in droplet microfluidics), whereas in droplet microfluidics the single cell output is strictly limited to one channel.

3.4. Patterned hydrophilic-hydrophobic surfaces in single cell analysis

Patterned hydrophilic-hydrophobic surfaces (HB/HL) have been successfully used as a design premise in cell capture applications [47]. HB/HL are also used to systematically split a droplet into defined volume fractions, and to consistently deposit small microdroplets in a high-throughput manner with well-defined volumes via sliding droplets over

hydrophilic spots [27]. In the single-cell capture context, HB/HL feasibility has been explored by simply adding particles-to-be captured into the seeding droplet.

Jogia *et al.* demonstrated HB/HL created via surface functionalising regular glass slides via thiol-yne photo-click reaction [48]. In short, the glass substrate was first coated with porous alkyne polymer layer, followed by applying two different ultraviolet (UV) sensitive –thiols. First, perfluorodecanethiol was applied and exposed with UV for 60 seconds through a photomask; second, b-mercaptoethanol was applied to the surface and exposed to UV for another 60 seconds. The resulting HB/HL displayed static contact angles of around 165^{o} and 0^{o} for the hydrophobic and hydrophilic parts respectively [49]; the corresponding thiols were perfluorodecanethiol for the hydrophobic part, and b-mercaptoethanol for the hydrophilic part.

Their hypothesis was that the occupancy would follow Poisson distribution. They studied three parameters known to have effect on the final distribution: spot size, cell suspension cell concentration, and seeding time. The hydrophilic spot sizes were 1000 µm, 500 µm, and 350 µm per side of a square, and the width of the hydrophobic area between the spots were 500 µm, 250 µm, and 175 µm correspondingly, i.e., half-spacing. Cell suspension concentrations were $1*10^4$ cells / mL, $4*10^4$ cells / mL, $7*10^4$ cells / mL, and seeding times used were 45, 60, and 75 s.

Technically, cell seeding was done by forming a sessile cell suspension droplet on top of the HB/HL positioned horizontally, followed by tilting the HB/HL which resulted formation of daughter droplets on the hydrophilic spots. Since small daughter droplets would evaporate quickly in normal atmospheric conditions, a humidified environment was created by covering Petri dish with tissue paper and phosphate-buffered saline (BPS) solution; while the HB/HL array rested on the bottom of the Petri dish. Furthermore, the HeLa cells used were fluorescently stained in order to response under fluorescent microscope for occupancy rate validation.

Jogia's best result from the single cell occupancy rate perspective was obtained with 500 µm spots, $4*10^4$ cells / mL, and 60 s seeding time leading to: 34.6 % empty spots, 19.4 % single cell occupancy rate, 14.6 % double cell occupancy rate, and 31.4 % multiple (3, 4, 5, more than 5) cell occupancy rate. While majority of the spots contained more than one single cell, HB/HL has demonstrated to be a valid technology for single cell capture. However, further optimization could lead to more preferable results: to reduce multiple

cells per spots, and increase the partition of single cell cases. Furthermore, in the light of previous findings in the microwell studies, the cell suspension concentration was found to be insignificant after certain *saturation* point, meaning that after some point, any increase to concentration would not increase the single cell occupancy rate. A saturation point might be supported by Jogia *et al.* In their study the increase of the concentration did not increase the single cell occupancy rate; however, it did slightly increase the multiple cell occupancy rate, while seeding time demonstrated similar trend as well. Furthermore, the hydrophilic spot size appeared to have most radical impact to differences in single cell occupancy rate between the selected sizes, in contrast to other parameters with same comparison. Therefore, the spot geometry may play a more critical role, or even decouple the occupancy rate from Poisson distribution should it prove to be absolutely impeding factor in formation of multiple cells per spot.

4. Concept design and modelling

4.1. The concept in brief

Our design premises of the single cell capture device presented here stem from wetting physics and robust microfabrication of hydrophilic-hydrophobic patterned surfaces. First design premise: surface with minimal liquid-solid contact and low surface energy exhibits superhydrophobicity, while otherwise the same surface, but with high surface energy, demonstrates superhydrophilicity. Second premise: standard lithography, thin film deposition, and etching processes provides means to consistently create HB/HL in a way that pattern geometry and surface contact angles can be systematically controlled. Consequently, the performance of such a device should be consistent and predictable. Furthermore, the trap / spot geometry can be optimised such that only single objects (particles or cells) are deposited per spot, rather than multiple. The objects-to-be-captured are now on referred in more general term "objects", and a clear distinction of objects are explicitly made between "particles" and "cells".

Objects are introduced to the HB/HL in an aqueous suspension by sliding suspension droplet on top of the HB/HL. This suspension droplet is termed as the mother droplet and the event is called seeding. By sliding the mother droplet along the HB/HL the mother droplet undergoes droplet fission due to imbalanced Young's force between hydrophilic and hydrophobic regions. Consequently, fissile droplets are deposited on to hydrophilic spots, and such droplets are referred to as daughter droplets. Figure 12 illustrates the HB/HL and the planned seeding strategy.

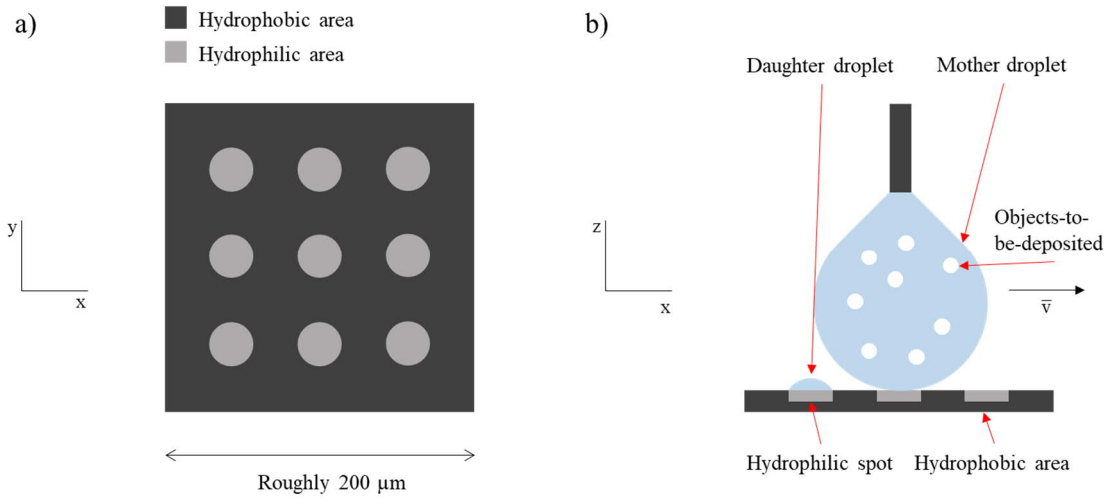

Figure 12: a) Schematic illustration of hydrophilic spots on hydrophobic background. The scale bar is a rough estimation to provide a sense of scale. b) Object (cell or particle) seeding is achieved by moving a

cell suspension droplet on HB/HL. The moving droplet splits into mother droplet and daughter droplet due to imbalanced Young's force. The droplet and the objects-to-be-deposited are not in scale.

In the figure 12a above, the hydrophobic part is fluoro-polymer coated black silicon (b-Si) depicted as dark grey colour, while the hydrophilic part is bare b-Si (i.e., without fluoro-polymer coating) depicted as light grey. The materials are discussed in more detail in the experimental part.

Furthermore, the daughter droplets are selectively formed on top of hydrophilic spots. The process control parameters in this seeding strategy are the seeding velocity and spot diameter, and the aim is to optimize the process with those parameters, while the suspension concentration is kept constant. Following sub chapters discuss deposition mechanism and optimisation in more detail.

4.2. Pattern geometry and sedimentation

The diameter of the hydrophilic area is expected to be the key factor in terms of selective single cell capture. In the microwell concept, the diameter worked as limiting factor so that individual well does not provide enough space for more than one cell [9, 10, 44] . Furthermore, cell diameter / well diameter ratio was found out to be approximately 1:2 [10, 44]. However, the HB/HL design by Jogia *et al.*[48] implicitly suggest that the volume of the daughter droplets may act as critical factor in terms of selective single cell capture, thus since the daughter droplet volume is governed by the size of the hydrophilic spots. The spots were significantly larger than 1:2, particle:spot ratio would suggest in [48]. Comparing the cell-count-per-spot distributions between the microwell and pattern designs in [10, 48], the microwell appears to demonstrate a better selectivity in terms of single cell capture. These observations lead to hypothesis that the optimal hydrophilic spot size for selective single cell trapping is much smaller than used in Levkin *et al.* [48] and are more close to the diameter ratio here [10].

One critical argument is that if a hydrophilic spot is already occupied by one object which fills most of the area, that object prohibits any second object deposition on to the same spot; analogous to coulomb blockade in small scale, or in large scale, a second basketball trying to enter into a closed basket already occupied by one basketball. This leads to a 1-to-2 design principle which means that selective single object capture based on this method is achieved when size of the object is approximately half, relative to hydrophilic spot size. Figure 13 illustrates the design of the single cell capture device following 1-to-2 design principle and design where the spot is more than twice as large:

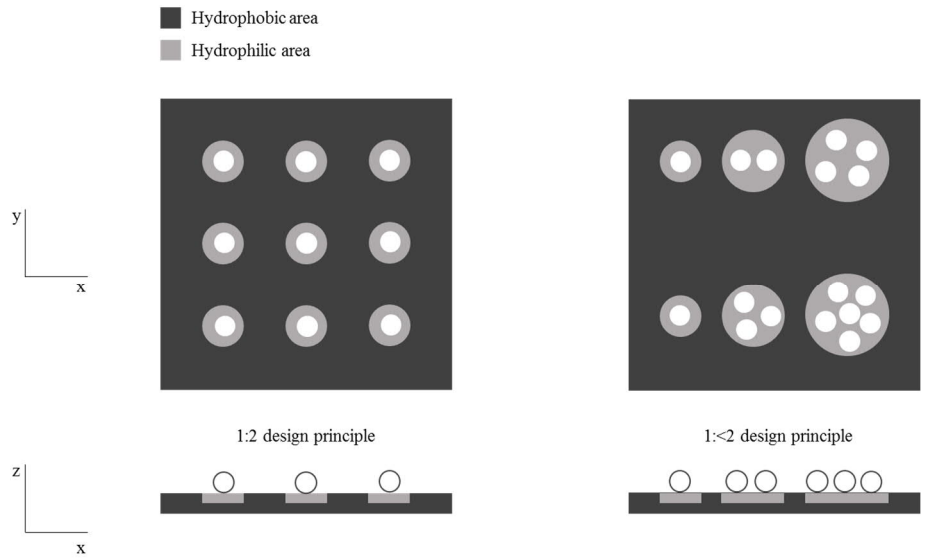

Figure 13: Schematic representation of captured objects on hydrophilic spots (grey area). Left: spots designed with twice the radius of a captured object. Right: various spots sizes where multiple particles can fit on spots larger than twice the radius of the object.

The 1-to-2 is arrived at by making spherical assumption, i.e., objects (particles and cells) are rigid non-overlapping spheres. Clearly, if the hydrophilic spot is much larger in comparison to object diameter, it can provide space for multiple objects (figure 13, right image). However, while optimal object size / spot size ratio is intuitive in this examination, the pathway for objects from seeding droplet to spots should also be discussed to construct a more solid foundation for the single cell trapping technology.

4.3. Deposition method, sedimentation, and transient capillary bridge

Typically in current single cell capture technologies based on microwells and HB/HL [10, 47], the cell seeding is based on gravitation; in practice, a cell suspension is placed on top of an array structure and passively left there until deposition. However, Chang *et al.*[27] and Li *et al.* [28] successfully deposited microdroplets on HB/HL by horizontally sliding a droplet along the surface, which inspires the adoption of similar seeding mechanism on single cell capture context; the seeding mechanism based on droplet sliding along HB/HL, depicted in figure 12b, is referred from now on as "active seeding". Essentially, active seeding mechanism is also based on gravitation, since any particle heavier than suspension medium (e.g., water) would undergo sedimentation according to Stokes' law:

$$v = \frac{2}{9}\frac{(\rho_p - \rho_f)}{\mu} g R^2 \quad (7)$$

The terminal sedimentation velocity of the particle in a fluid depends on the density of the particle and density of the fluid (ρ_p and ρ_f, respectively), dynamic viscosity (μ) of the

fluid, gravitational acceleration (g), and radius (R) of the particle. Stokes' law sets critical boundary condition to the active seeding: suspension must be lighter than the particles. Furthermore, different sized particles will sediment at different rates, since terminal sedimentation velocity is proportional to the square of particle radius. Figure 14 illustrates the active seeding mechanism.

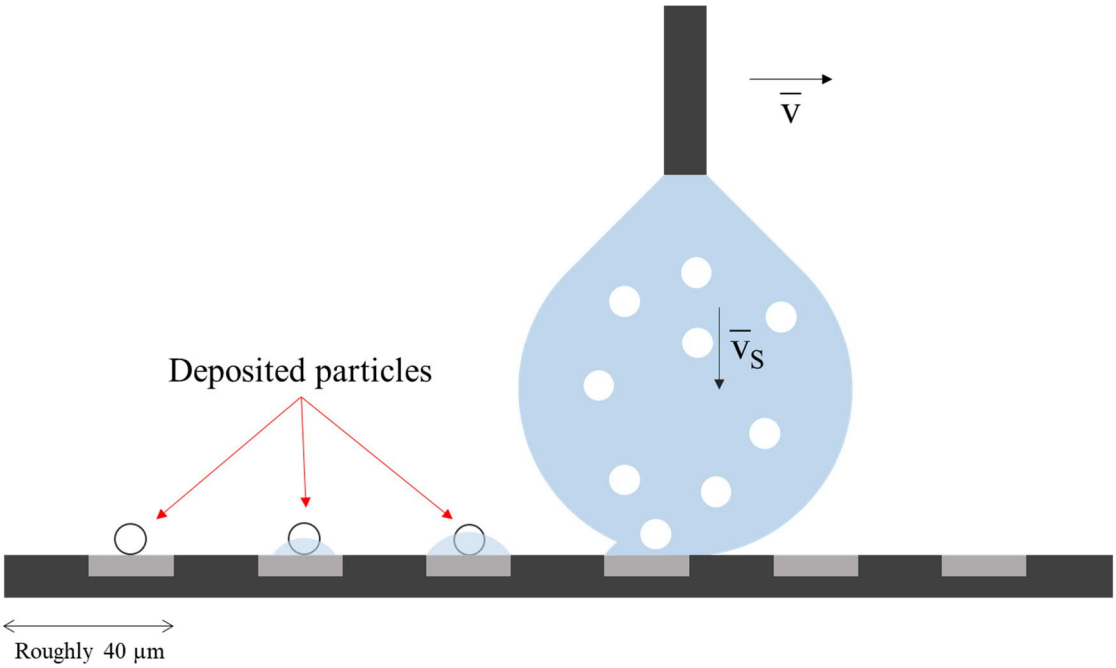

Figure 14: Schematic illustration of the active seeding mechanism. The moving droplet leaves a trace of daughter droplets and particles on hydrophilic spots. Illustration is not in scale. Rough scale bar is to provide better sense about the scale level.

The first spot from the left supports one deposited particle and shows no daughter droplet since such small droplet would have evaporated quickly. For example, following the 1-to-2 particle / spot design rule, a 10 µm diameter particle would require 20 µm diameter spot. For simplicity, we assume that daughter droplet initial shape (right after formation) is half sphere, when the volume of the daughter droplet would be $4*\pi*r^3/6$, i.e., around 2 picoliters, leading to evaporation time around 2 seconds from full droplet to fully evaporated [50]. The second and third spot from the left depicted in figure 14 show intermediate stages in daughter droplet evaporation, while fourth spot visualises the supposed simultaneous formation of daughter droplet and particle deposition. However, the event window between the initial contact of the mother droplet and spot, and the separation of a daughter droplet requires closer inspection.

The deposition event suggested here would require solid-solid interface, i.e., particle-spot interface. If sedimentation ensures that a particle would eventually fall to the bottom of

the seeding droplet, then the next requirement is a pathway from seeding droplet to the spot surface. Since the seeding droplet will wet the spot, but not the hydrophobic area around the spot, it is likely that a capillary bridge forms between the seeding droplet and spot, providing pathway for the particle in form of water channel. Dufour *et al.* demonstrated the capillary bridge formation on omniphobic surface consisting of 18 µm circular areas with 12 µm spacing (air gap) between individual "spots". Curable polymer was slid horizontally along the surface and solidified to obtain images of the capillary bridge [51]. Their experiment was different than the concept suggested here, since their hydrophilic spots were pillars rather than flat spots. However, it can be considered somewhat analogous in the capillary bridge part. Figure 15 illustrates our proposed capillary bridge formation and particle pathway in HB/HL:

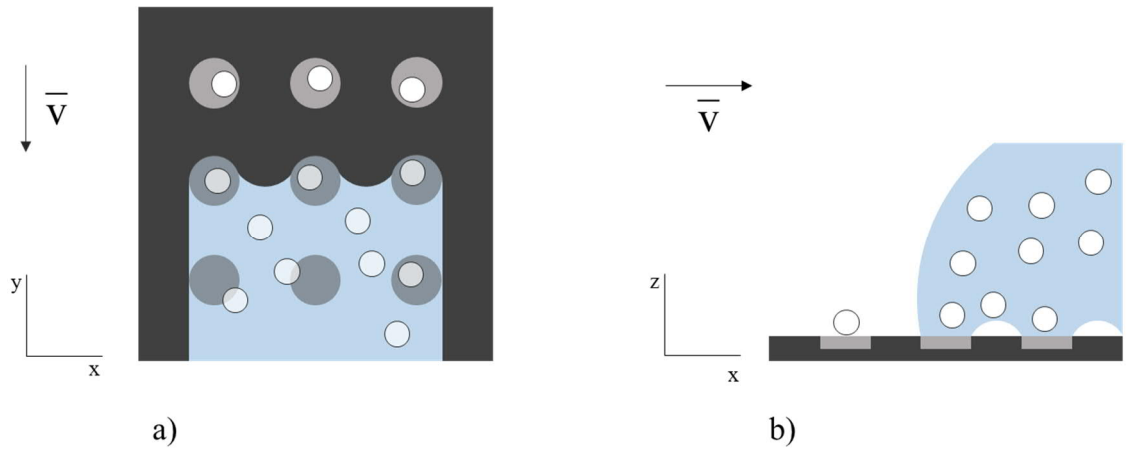

Figure 15: a) Top view of the seeding droplet moving on HB/HL. b) An illustration of temporary capillary bridge, which provides the pathway for the particle to become in contact with the hydrophilic spot.

Hypothetically a droplet moves forward and encounters hydrophilic spots, it forms a transient capillary bridges between it and the seeding droplet, providing unimpeded pathway to particle migration. Consequently, as the particle comes into proximity with hydrophilic spot, sharing solid interface, it can immobilize there. Simultaneously, the seeding droplet continues forward motion and begins to elongate until it finally snaps into quickly evaporating daughter droplet and mother droplet. One likely scenario is that particle deposition occurs at the receding end of the droplet, since any "deposited" particle would encounter desorption due to rinsing power of consecutive fluid motion (figure 15a).

Furthermore, according to particle dynamics simulation study conducted in [52] a vortex-like flow pattern is formed inside a fluid droplet moving along a solid surface. The flow pattern revolves around the center of the vortex, such that the flow direction at the upper part of the droplet is parallel to droplet moving direction, while at the bottom the flow

direction is opposite to droplet moving direction. Figure 16 illustrates the flow pattern inside a moving droplet in the active seeding context:

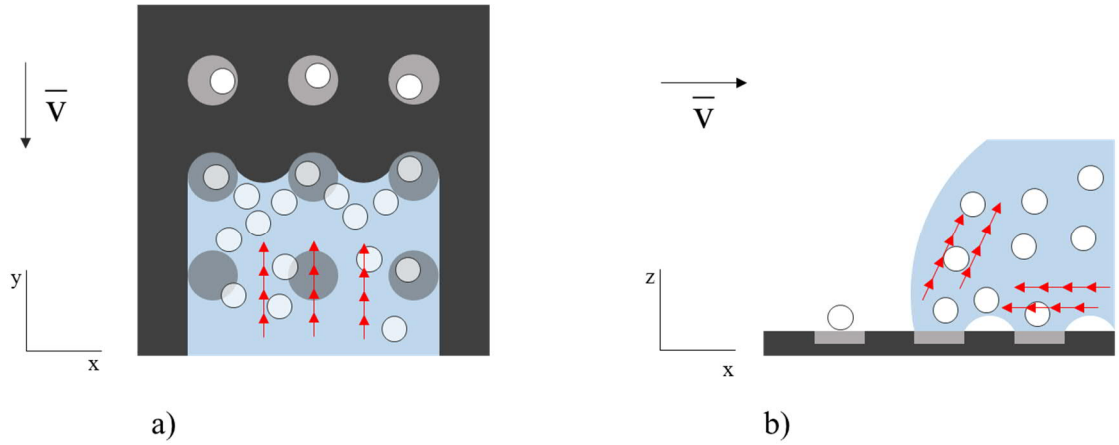

Figure 16: a) The flow pattern at the bottom of the seeding droplet is towards the receding end. b) At the receding edge, the flow pattern is upwards causing the particles to float up based on [52].

The red arrows indicates the flow direction induced by droplet forward motion, according to [52]. At the bottom, near the solid-liquid interface, the flow direction is towards the receding edge (figure 16a) which can provide a steady stream of particles to close proximity with hydrophilic spots leading to deposition; simultaneously, flow direction begins to turn at the receding edge sending the "excess" particles back to circulation (figure 16b). Similar flow pattern is typical in evaporating droplets undergoing the so-called Marangoni effect induced by a surface tension gradient [53].

When the Marangoni effect is significant, two distinct flow patterns form inside the droplet, referred as convective flow and outward flow, where the latter flow pattern occurs near the solid liquid interface. Interestingly, the outward flow region velocity profile ends at the liquid-solid-vapour triple point, while convective flow pattern velocity profile is radial, so that is has vortex center; a point (or line) where these two flow patterns meet is termed as the stagnation point. Since the outward flow ends at the solid-liquid-vapour interface at the bottom perimeter of the droplet, it causes any particles in such flow pattern, below the stagnation point, to aggregate to the bottom perimeter causing so-called coffee stain phenomenon [54, 55].

While Marangoni flow is induced by different forces in comparison to flow patterns inside a moving droplet, it is somewhat analogous. Specifically, if the incoming and the outgoing particle streams are imbalanced, then some level of particle aggregation to receding edge can occur, forming a cluster of particles. Ultimately, that would cause the

particle deposition events to take place exactly at the receding edge. Figure 17 finalizes the suggested scenario ensuing from the active seeding method.

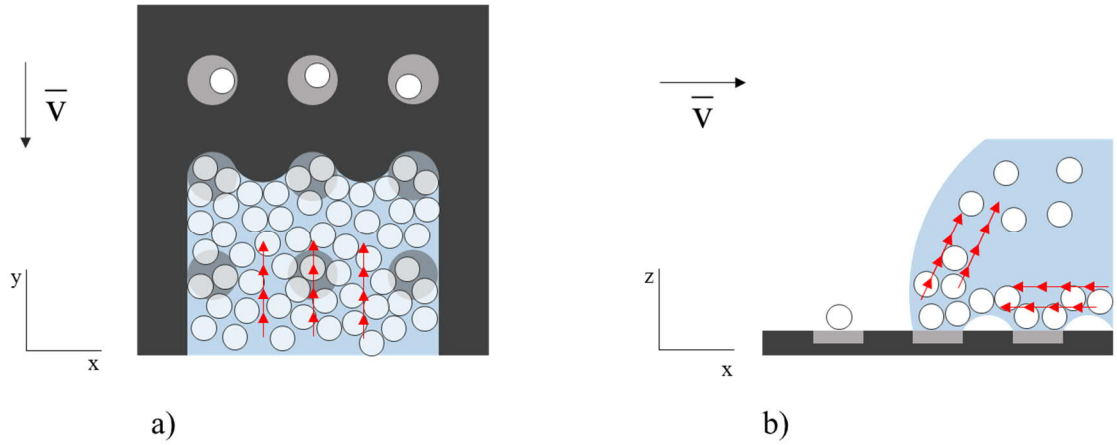

Figure 17: a) Illustration of particles aggregating to the receding edge due to vortex-like flow pattern. b) Due to the irregular shape of the droplet, the up flow rate may be slightly slower than the income flow rate, which could at least partially cause the particle aggregation to the receding edge based on [52].

We believe that the combination of radial flow pattern [52], the capillary bridge formation between mother droplet and a hydrophilic spot [51], and 1-to-2 design principle will lead to single-particle deposition. In that scenario, the inner flow pattern and sedimentation ensures that particles are situated at favourable position for deposition, while capillary bridge provides the ultimate pathway for the particle to migrate from seeding droplet to the spot; furthermore, adjusting spot size by 1-to-2 rule mitigates any double particle deposition. However, due to complexity of the model scenario, an analytical or numerical simulation would be difficult. Instead, a stochastic model is proposed to simulate the scenario in the following chapter.

4.4. Stochastic model for particle deposition: Markov chain stationary distribution

To model active seeding of particles on HB/HL, we applied a Markov chain process due to its simplicity and versatility. Markov chain is stochastic process where some sequence of random variables X_i realizes at each time i, where possible values for X_i is defined by state space χ, and the probability of each state $x \in \chi$ is determined by transition matrix P. Practically, state space defines all the possible states of the process, while transition matrix defines the transition probability between each state. An important property of Markov chain is that it is not dependent on the history of the process, i.e., the next state is only dependent on the current state; furthermore, since elements of transition matrix P are probabilities, they are non-negative and each row sums to 1.

To elaborate, consider coin toss with a fair coin, where probability of head or tails is 50-50, then the possible states are heads or tails, and the transition matrix P is:

$$P = \begin{matrix} 0.5 & 0.5 \\ 0.5 & 0.5 \end{matrix}$$

The Markov process is further visualised as transition diagram in figure 18:

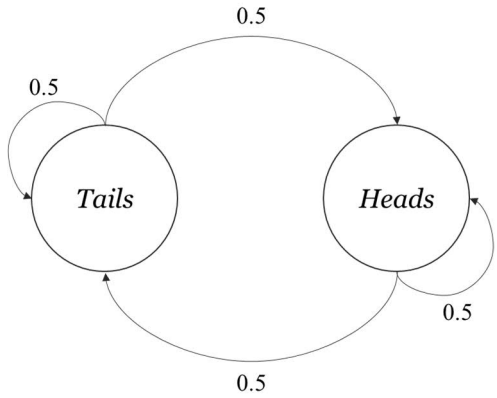

Figure 18: Markov process transition diagram for fair coin toss scenario. From any current state, the probability of heads or tails in equal: 1/2.

The transition diagram indicates that the probability between any next state is 0.5, given any starting state. As a direct consequence, there are no absorbing states, i.e., both states are recurring. If stochastic process depicted in figure 18 is driven *ad infinitum*, the stationary distribution of such process would be fifty-fifty. Stationary distribution refers to the limit distribution which is achieved in the long-term when Markov process is ran multiple iterations; specifically, after the stationary distribution is reached, the distribution does not change. [56]

Applying Markov chain model to active seeding method in HB/HL the requirement is to define state space χ and transition matrix P. The states selected are deposited particles per spot 0, 1, 2, or 3, and limited to 1-to-2 particle size:spot size scenario. Due to lack of describing equations, the probabilities of transition matrix are difficult to define. A geometric examination enables simple approach to determine transition probabilities between states. In particular, the geometric examination presented in figure 19 is based on the active seeding scenario discussed in chapter 4.3.

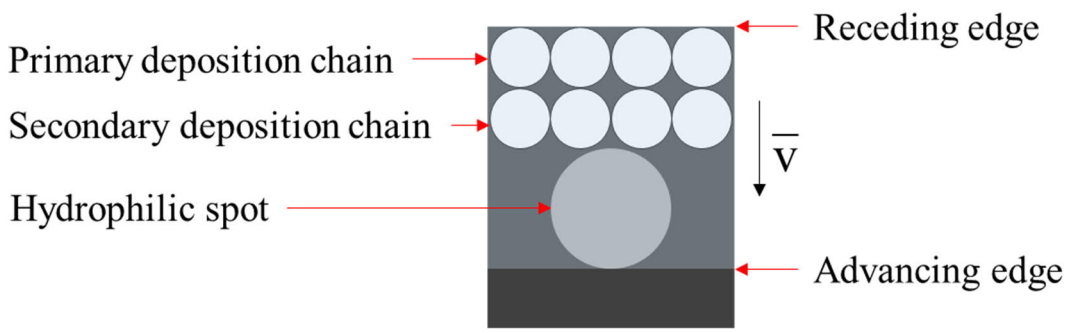

Figure 19: Starting point of the hypothesized primary and secondary deposition chains. The one unit model is assumed to generalize into multiple spot array.

It is assumed that the particle deposition occurs at the receding edge from so-called primary deposition chain. The primary deposition chain is a uniform chain of particles formed against the receding edge. The so-called secondary deposition is the next chain of particles depicted in figure 19; term "secondary" stems from the reasoning that if a particle has deposited from the secondary deposition chain, it will be pushed off by the particles situated in the consecutive chain, when those particles would occupy the spot instead. Figure 20 depicts a simple particle deposition case based on the model:

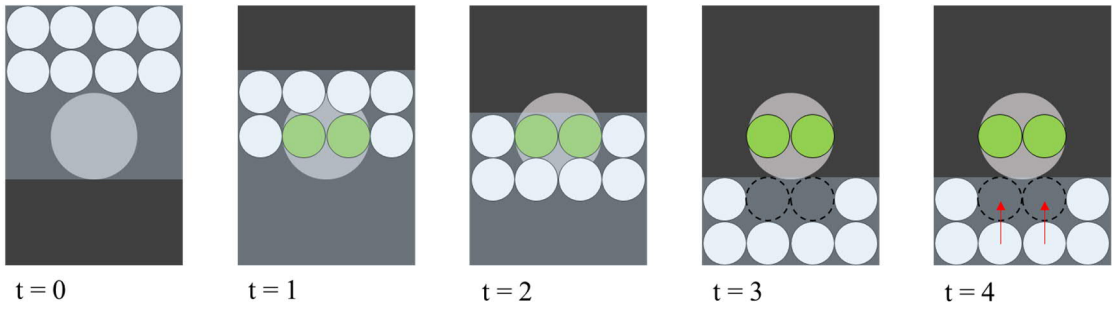

Figure 20: One particle chain-spot unit deposition process over time based on geometric examination. The time unit is arbitrary.

In the beginning, primary and secondary deposition chains (white circles) are not in contact with the spot, depicted as light grey. At t =1, secondary particle chain is in contact with the spots; however, at t = 2, primary deposition chain has pushed previous particles of. At t = 3, the mother droplet and daughter droplet has separated, leaving two particles on spot in this case; furthermore, due to two deposited particles, two vacancy sites are formed at the primary deposition chain. The vacant sites are refilled from the secondary chain, and from consecutive chains (not pictured in figure 20) before encountering next hydrophilic spot.

Since there is no control over the alignment between the spots and the particle chains, they chains are assumed to be randomly aligned. Furthermore, the primary and secondary

chain can be misaligned with respect to each other, i.e., the chains are not always perfectly aligned as in figure 20. However, rather than considering continuous, infinitesimally small differences between alignments, assume 10 discrete steps how particle chain can be horizontally aligned with respect to a spot. Furthermore, we assume that primary and secondary deposition chains are either perfectly aligned or perfectly misaligned. This leads to 20 different particle chain alignment cases with respect to hydrophilic spot. Adopting this reasoning, the probabilities for particle deposition can be determined via geometric examination. Figure 21 combines the possible alignment cases for geometric examination where the green circles marks for deposited particle.

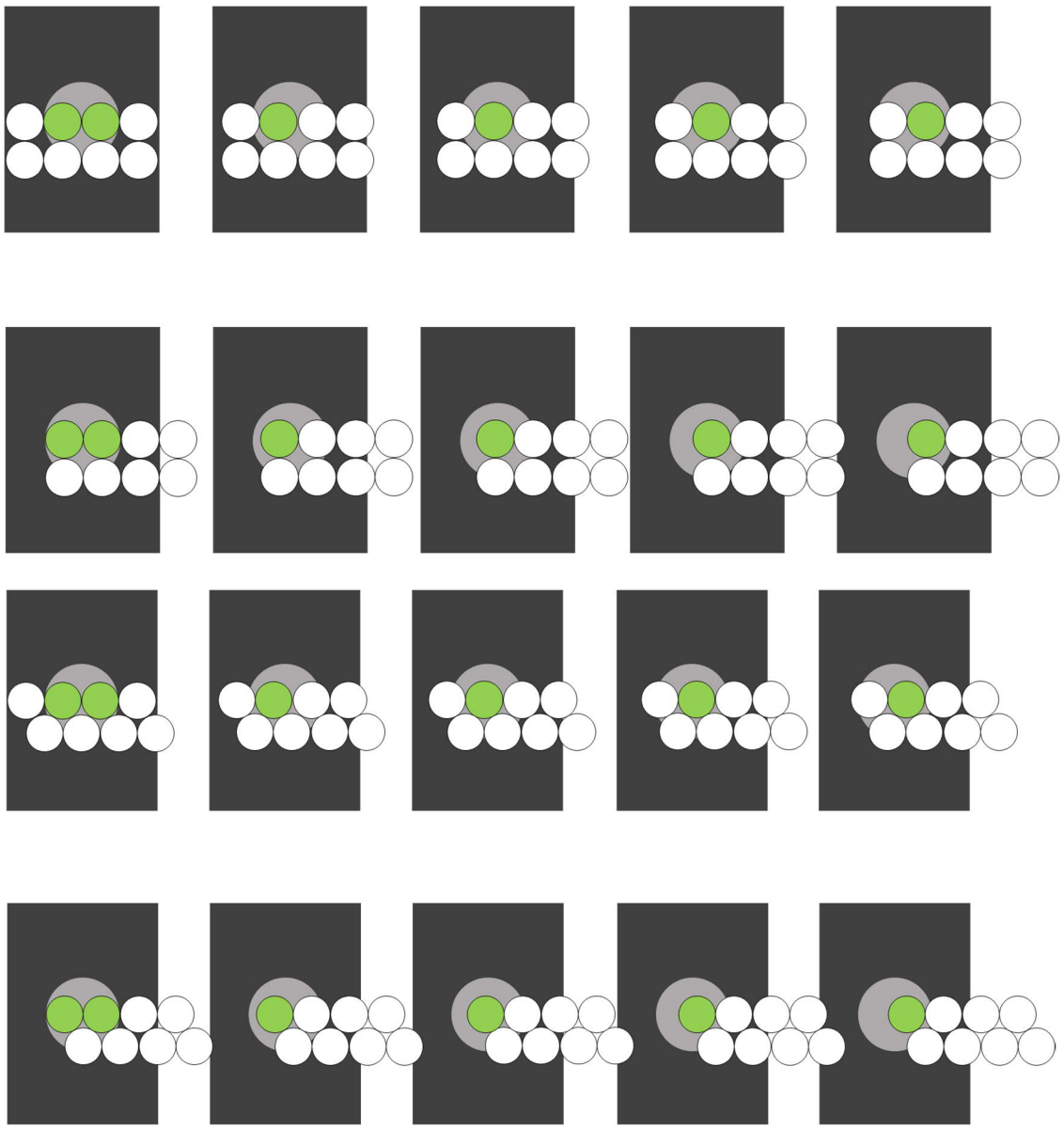

Figure 21: Model with 20 arbitrary deposition chain alignments relative to the hydrophilic spot. The probability of double particle deposition is significantly smaller than one particle deposition, since double particle deposition requires so-called perfect alignment (left-most images with two green circles side by side).

According to the geometric examination, the two particle deposition cases are rare since they require perfect alignment between the hydrophilic spot and the primary deposition chain, while single particle deposition is much more likely. In total, 16 out of 20 possibilities are single particle deposition, while only 4 out of 20 would be double particle cases. However, since deposited particle creates a vacancy to the corresponding deposition chain it must be filled before the next spot or the next deposition cannot occur. The vacancy would most likely be filled from the secondary deposition chain. We assume that the vacancy is filled with 50 % probability, which lowers the single particle deposition rate to 40 %, and double particle deposition rate to 10 %. That is, the probability that the spot remains empty is now 50%. The corresponding transition matrix P in now:

$$P = \begin{matrix} 0.5 & 0.4 & 0.1 \\ 0 & 1 & 0 \\ 0 & 0 & 1 \end{matrix}$$

And in the form of transition diagram as:

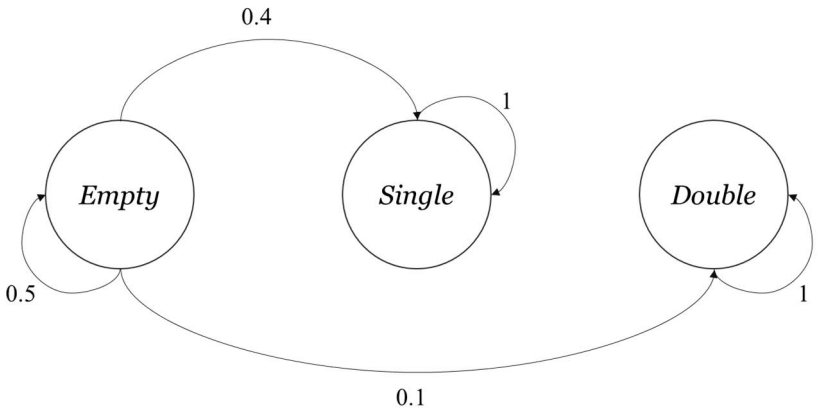

Figure 22: Markov process transition diagram of particle deposition model. Transition probabilities are based on the geometric model. The particles are assumed to completely immobilize once deposited.

However, the above transition matrix in figure 22 assumes that once particle is deposited it completely immobilizes and cannot be removed; the transition diagram above shows only one-way possibilities. The model does not take any adhesion forces into account, or the possibility that deposited particle can rinse off from the surface due to moving mother droplet. A more realistic assumption is that deposited particles can detach and end up back to the seeding droplet; consequently, an empty spot is left behind. We assume that deposited particle immobilizes completely with 50 % probability. That is, there is equal

50 % probability that deposited particle detaches from the spot. The transition matrix P becomes:

$$P = \begin{matrix} 0.5 & 0.4 & 0.1 \\ 0.5 & 0.5 & 0 \\ 0.25 & 0.25 & 0.5 \end{matrix}$$

And transition diagram can be formulated as:

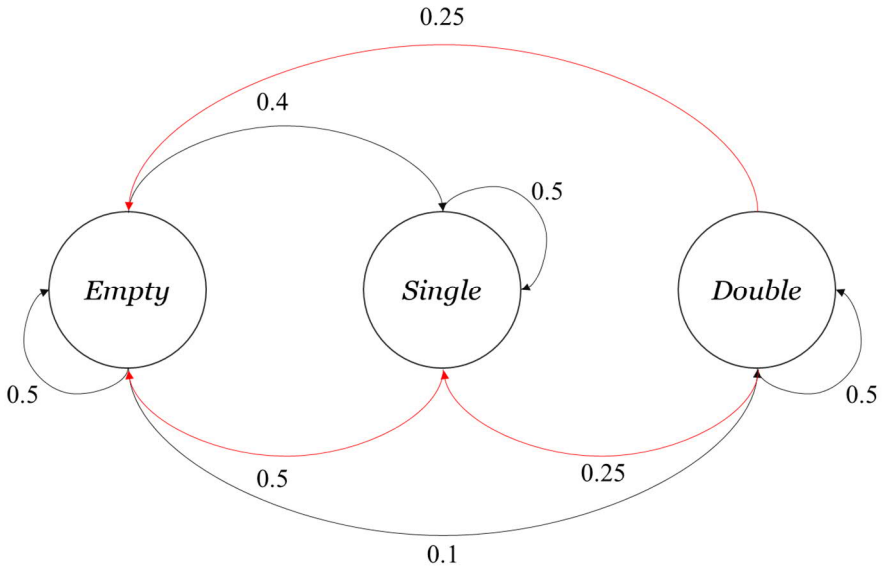

Figure 23: Markov process transition diagram on the particle deposition model. The particles are now not assumed to immobilize completely, but to detach from the spot with 50 % probability (red arrows) after deposition.

Now the transition diagram has two-way form, where the red arrows indicate detaching of particles once "deposited", while black arrows indicate deposition and complete immobilization of particles. In this form of Markov chain, it is possible to run process multiple iterations and determine the stationary distribution; here each iteration represents deposition probability on one spot, and each spot is considered to be independent from other spots in the same line. Figure 24 displays the occupancy rate distribution after 1000 iterations:

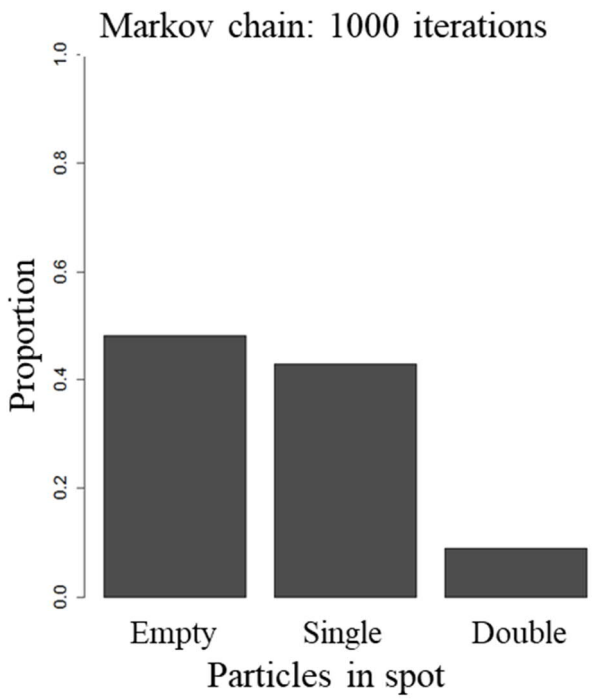

Figure 24: Simulated Markov process with 1000 iterations. The stationary distribution is 51 % empty spots, 42 % single particles, and 9 % double particles.

According to the Markov model developed here, the total occupancy rate is around 51 %, single particle occupancy rate is 42 %, and double particle occupancy rate 9 %. However, the weak assumption is the complete immobilization rate (red arrows on the transition diagram). To test the model sensitivity to the weak assumption, the transition probabilities are adjusted in 10 % increments, a 10 % increase means 10 % higher probability for once-deposited particles to completely immobilize, and vice versa. Figure 25 collects stationary distributions obtained from 1000 iterations with varying transition probabilities:

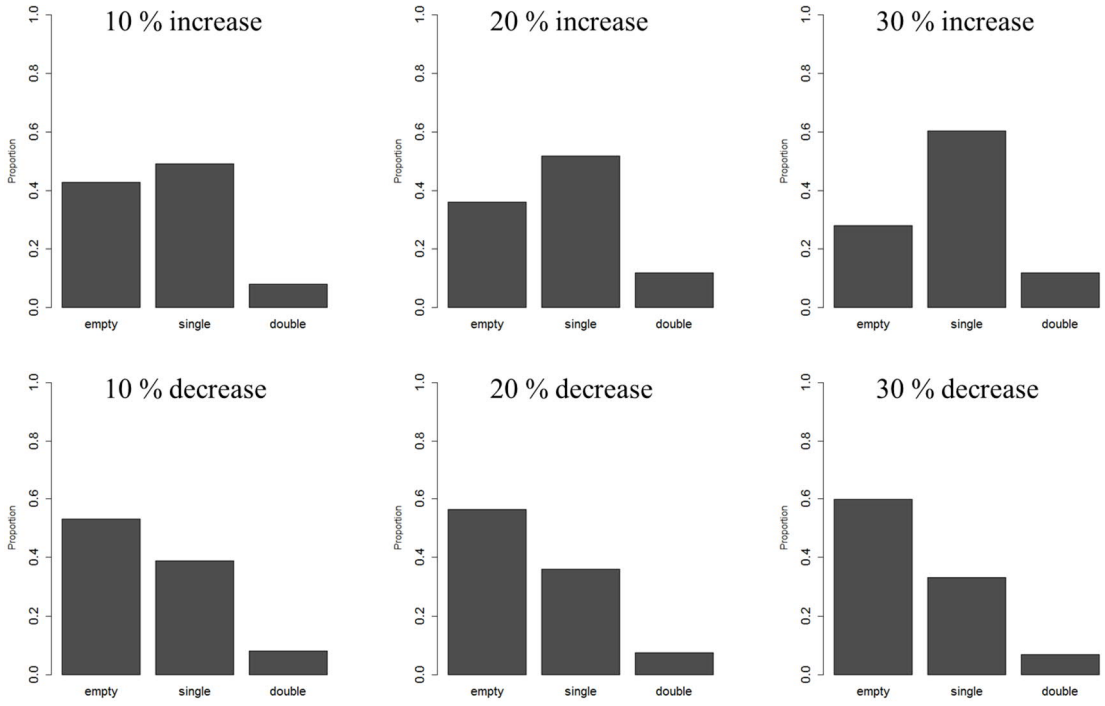

Figure 25: Markov process stationary distributions with different immobilization rates. The ratio between single and double particle deposition remains the same, while, the overall capture rate is increased. When immobilization probability is decreased, the overall capture rate decreases as well. Markov process is ran 1000 iterations in all cases.

Initial observation is that the total occupancy rate increases with higher immobilization rate. The lower three plots depict stationary distributions with lowered immobilization rate which seems to lower the total occupancy rate. However, the ratio between the single and double particle cases remains the same; furthermore, the underlying rationale of single / double ratio emerges from the geometric examination, which is considered as strong assumption here.

Finally, the Markov chain model developed here predicts around 80/20 ratio between single and double particles cases, respectively. The ratio clearly stems from the assumption derived from the geometric examination illustrated in figure 21, and is considered as strong assumption since it has some physical stand points developed earlier in chapters 4.1, 4.2, and 4.3. However, the Markov model here is partly based on weaker assumptions as well with no direct physical stand point, causing some instability to the model from total occupancy rate perspective; nevertheless, the 80/20 single / double particle ratio appears to be robust, i.e., insensitive to immobilization probability changes. Ultimately, the model suggests that the total occupancy rate will land somewhere between 70 % and 40

%, with 80/20 single / double particle ratio, when active seeding is used in spots sizes twice as large as the particle.

5. Experimental

5.1.1 Microfabrication of hydrophilic-hydrophobic black silicon

Hydrophobic hydrophilic patterning (HB/HL pattern) was achieved via one-step optical lithography process using black silicon (b-Si) as starting material. Black silicon in turn was fabricated via cryogenic deep reactive ion etching (cDRIE). Black silicon used here is achieved via process originally introduced by Sainiemi et al. [57]. The starting material is 100 mm single-side-polished (SSP) silicon wafer which is processed into b-Si via cDRIE process. The critical parameters to control b-Si surface topography is oxygen partial pressure of SF_6/O_2 plasma which is tuned so that overpassivation of the silicon substrate occurs, leading to nanograss structure [57]. The cDRIE process parameters used here are listed in the table 1 below.

Table 1: cDRIE process parameters for black silicon. Starting material is single side polished silicon wafer.

Parameter	Value [unit]
Starting material	SSP silicon wafer, 100 [mm]
Chamber pressure	10 mTorr
Platen power	6 [W]
SF_6/O_2 flowrates	40 / 18 [sccm]
Chamber temperature	-110 [ºC]
Time	7 [min]

The resulting b-Si surface demonstrates pyramid-like structure with average base width of approximately 1 µm and height around 1.5 µm. Furthermore, the resulting b-Si demonstrates hydrophilicity with apparent contact angles close to zero since silicon surface has high surface energy [58].

The surface is made superhydrophobic by depositing a thin fluoropolymer film layer onto b-Si via Plasma-enhanced Chemical Vapour Deposition (PECVD). The polymerization was done with RIE Plasmalab 80 tool, using CHF_3 as a precursor gas with 100 sccm flowrate, 50 W RF power, 250 mTorr chamber pressure, and deposition time of 5 minutes.

The resulting ca. 40 nm thick polymer film demonstrates considerably lower surface energy in comparison to b-Si, which ultimately leads to apparent contact angles around 170° [57], i.e., superhydrophobic surface.

The HB/HL pattern was done via a single photolithography step. Thick positive photoresist (AZ 4562, MicroChemicals [59]) was spin coated on the fluoropolymerized b-Si, followed by 5 minutes soft baking at 90°C with hotplate, to minimize solvent concentration. Next, the resist-coated wafer was exposed to 162 mJ/cm^2 ultraviolet light (UV) dose through a photomask. The photomask contained 21 squares of 1 cm x 1 cm with different array patterns. The array patterns consisted of circles with different diameters (22, 20, 18, 16, 14, 12, 10, 8 µm) with three different pitching (1x, 2x, and 4x, measured from circumference).

The resist development was done by immersing the wafer into AZ 351 B (MicroChemicals) positive resist developer for 6 minutes, followed by water rising and blow drying with nitrogen.

The patterning is finalised via anisotropic reactive ion etching (RIE) using O_2 plasma for 3.5 minutes using RIE Plasmalab 80 tool. The aim of RIE is to remove the fluoropolymer film from the exposed parts of the wafer, i.e., to convert the spot areas (UV exposed) back to hydrophilic, while maintaining superhydrophobicity elsewhere. Finally, the excess photoresist mask is removed by immersing the wafer into acetone (2 min, ultrasonic), acetone (1 min), isopropyl alcohol (1 min), water rinse, and blow dry with nitrogen, which completes the microfabrication part. This resist removal treatment leaves the hydrophobic area with apparent contact angle of 170°, and hydrophilic spots with apparent contact angle of 0°.

The wetting properties was measured and analysed with Biolin Scientific, model Theta – goniometer. For static contact angle measurements, a sessile water droplet was dropped on the surface; however, the prediction is that water droplet will not stay still on the superhydrophobic parts, making such measurements difficult. Advancing and receding contact angles were measured by bringing the goniometer water inlet pipe to proximity with the surface, followed by dispensing water at constant 0.025 µl/s rate, resulting as slowly growing droplet; advancing contact angle is measured over time when droplet grows, while receding contact angle is measured over time when droplet shrinks (i.e., is pumped

back to the inlet). Data was analysed and visualised with the goniometer software, provided by Biolin Scientific. The HB/HL was imaged with EBL Zeiss Supra 40 scanning electron microscope.

5.1.2. Microfabrication of hydrophilic-hydrophobic planar silicon

A HB/HL with planar spot version was made to improve imaging properties. In the planar version of HB/HL, the spots are planar silicon, and the rest is fluoropolymer coated black silicon.

The starting material is single side polished silicon wafer. Initial step is to deposit silicon dioxide (SiO_2) film to work as hard etching mask using PECVD (PECVD Plasmalab) on the wafer. PECVD operating substrate temperature was 300ºC, working pressure at 1000 mTorr, and process time 12 min. The gas flowrates were 8.5 sccm, 710 sccm, and 161.5 sccm for Silane, N_2O, and N_2, respectively.

Image reversal photolithography is initialized by priming the wafer surface with hexamethyldisilizane to promote photoresist adhesion to the surface. Wafer was spin coated with AZ 5214 E (MicroChemicals) photoresist, and soft bake at 90ºC for 2 minutes was applied. Resist-coated wafer was exposed using 27 mJ/cm^2 UV dose through the photomask in order to induce cross-linking of the photoresist on UV exposed parts, making those parts thermally stable up to 130ºC. Secondary bake is applied with hot plate operating at 120ºC, for 2 minutes, followed by flood exposure (UV exposure without a mask) using 180 mJ/cm^2 UV dose. The lithography is completed by resist development via chemical immersion to AZ 352 B. The oxide layer was removed from the parts where there is no photoresist mask via RIE (RIE Plasmalab 80 tool), followed by resist removal in acetone bath.

Black silicon is fabricated to the surface via same cDRIE process as explained in the chapter 5.1.1., using the same parameters. After the b-Si process, the excess oxide hard mask is removed in hydrofluoric-acid, which selectively attacks only SiO_2. After oxide strip, the process continues from the fluoropolymer deposition by PECVD, photolithography, and RIE with the same parameters as explained in chapter 5.1.1. The resulting HB/HL hydrophilic spots are now planar silicon and the rest is black silicon.

5.2. Seeding droplet fission and daughter droplet volume

Seeding droplet fission and volume was measured with contact angle goniometer by Biolin Scientific, model Theta. An automatic disposable tip dispenser (model C311-300, Biolin Scientific) attached to moving Z-axis holder was used to maintain 10 – 20 µl water droplet above the sample, before contact. The sample was positioned on moving XY-stage, with zero tilt in both axes. The sample consisted 10 mm x 10 mm chips with either 100, 90, 80, 70, 60, 50, 40, or 30 µm circular hydrophilic spots inside; the distance between the spots was three times (from center) the diameter of the spot.

After initialization, the droplet was brought to contact with the sample; the aim was to have as minimal liquid-solid contact area as possible, and to induce minimal deformation to the droplet. Minimal liquid-solid surface area and droplet deformation was achieved by observing droplet approach toward the substrate via live camera feed (USB 3.0 digital camera with zoom, provided by Biolin Scientific); the camera is attached horizontally, so that the camera image is perpendicular to YZ-plane.

Once the droplet is in contact with the substrate, the XY-stage is moved along Y-axis at constant velocity (seeding velocity); the seeding velocities used were 10 mm/min and 100 mm/min. The consistency of the mother droplet fission was observed and recorded with the attached camera system at 60 frames per second in order to accurately capture the individual droplet fission events. The volume of the daughter droplets were measured from the captured images; the volume was calculated using spherical cap equation:

$$V_{cap} = \frac{1}{6}\pi h(3a^2 + h^2) \qquad (8)$$

The base radius a was assumed to be equal to half of the hydrophilic spot diameter, while spherical cap height h was measured from the images using imageJ software. The daughter droplet volumes were measured for both seeding velocities, and all spot sizes.

5.3. Single particle capture

In the single particle capture experiments, the water droplet was substituted with aqueous particle suspension, otherwise the experimental setting was equipment-wise same as described in the previous section (5.2.). Three different sized particles were used, 8 µm, 10 µm, and 20 µm (diameter). Particles were polystyrene particles in aqueous solution provided by Sigma Aldrich with the following specifications provided by the vendor: 2 %

cross-linked, size standard deviation 2 %, and density of 1.05 g/cm^3, and 10 % solid concentration. The particle suspension was diluted by adding DI-water in 1:10 ratio. The approximate number of particles in the diluted solution is:

$$n_p = \frac{m_{suspension} * 0.1}{V_p * \rho_p} \rightarrow \frac{m_{suspension} * 0.1}{4 * \pi * \frac{r^3}{3} * \rho_p}$$

$$\rightarrow \frac{1g * 0.1}{4 * \pi * \frac{0.0005^3 cm^3}{3} * 1.05 \frac{g}{cm^3}} \qquad (9)$$

$$n_p \approx 1.8 * 10^8$$

Then, the approximate number of particles in the seeding droplet is the ratio of seeding droplet volume and total volume of diluted suspension multiplied with total number of particles n_p:

$$n_{p,s} = \frac{V_{seeding}}{V_{total\ suspension}} n_p \rightarrow \frac{0.01\ ml}{11\ ml} * 1.8 * 10^8$$

$$n_{p,s} \approx 160000$$

This leads to approximate concentration of 16000 particles / µl.

An approximately 10 µl particle suspension droplet was maintained on top of the patterned substrate with minimal solid-liquid contact area (ca. 0.2 mm^2), while the substrate was moving towards Y direction at constant seeding velocity (10 mm / min or 100 mm/min) for 5 mm distance per spot size. Table 2 combines all the parameters used in the experiment:

Table 2: Experiment parameters and values for particle deposition experiments.

Parameter	Values	Unit
Seeding velocity	10, 100	mm/min
Spot size (diameter)	8, 10, 12, 14, 16, 18, 20, 22, 30, 40, 50, 60, 70, 80, 90, 100	µm
Particle size (diameter)	10, 20	µm
Particle concentration	16000	particles / µl

Once the particle suspension droplet came into contact with a hydrophilic spot, a capillary bridge was formed and particle can deposit. Then, the suspension droplet was moved and held in contact for 5 mm distance, leaving around 5 mm long line of particles behind. After seeding / deposition, the suspension droplet is detached and moved on to next chip. The width of the deposited particle line was controlled by adjusting particle suspension droplet distance from the array surface; however, due to constant attaching / detaching of the particle suspension, and inaccuracies in droplet tip / array surface distance, the width will show differences between chips.

The results were evaluated with optical microscopy and a custom-made image analysis algorithm [60]. Occupancy rates were evaluated such that the number of spots in the image is calculated by multiplying number of spots in vertical direction and number of spots in horizontal direction. Number of spots in vertical direction is obtained from the image by counting the spots that fit on the image, i.e., spots that are visible within the image frame. Number of spots in horizontal direction is obtained by counting spots within the contact area / line of the suspension droplet, i.e., finding the left-most and right-most filled spots and counting the spots between them along horizontal line.

The obtained images are used as an input for the custom-made image analysis algorithm written in R. R package *EBImage* is used to manipulate the images and for image feature calculation. Image processing begins by converting the captured images into binary form where the background is represented as black and particles are represented as white. Next, the areas of separate white pixel regions are calculated which are then used as input in clustering and classification algorithms. K-nearest neighbour and k-means clustering methods are used to cluster single-, double-, and multiple particle cases accordingly. Finally, occupancy rate distribution is obtained, which is used as the primary evaluation statistic of the single particle / cell capture technology feasibility. [60]

5.4. Single cell capture

The primary cells used were peripheral blood mononuclear cells (PBMC) isolated directly from an anonymized human blood sample extracted from a patient at Helsinki University Biomedicum facilities. The ethical board permission to use patient cell samples was granted to Helsinki University Immunology Group (permission number 103/13/03/01/2016 and 147/13/03/01/16) which worked as responsible cell sample provider through the experiments. PBMC are essentially white blood cells, with average diameter around 10 - 15 µm. The second type of cells used is THP-1 cell line. THP-1 cells

are a monocytic human cell line, originated from a leukaemia patient. Both cell suspensions were prepared at Helsinki University Biomedicum facilities by a laboratory specialist.

Initially, the cells were separated from the cell medium via leucocep protocol, followed by washing and rinsing the cells in phosphate buffered saline (PBS). Then, cells were centrifuged until a cell pellet formed on the bottom of an Eppendorf tube. After that, excess PBS was removed with pipette – then rinsing and washing process was repeated three times over. The separated cells were fluorescently stained with cell tracker staining kit from ThermoFisher, using protocol recommended by the staining kit vendor [61]. Finally, the cells were counted using Bio-Rad TC20 cell counter tool. The as-received cell suspension consisted of approximately 100 000 cells / 10 µl in PBS + 0.01 % bovine serum albumin.

The cell suspension seeding was done with the same protocol as used in particle deposition explained in chapter 5.3. In addition to 10 and 100 mm/min seeding velocities, 30, 50, 70, and 90 were also used.

5.5. Imaging and microscopy

The primary characterization method to evaluate particle deposition experiments was optical microscopy. The digital images were mainly used to calculate the particle occupancy rates. All digital images regarding to particle experiments were obtained with Zeiss Axiotron microscope equipped with digital camera. Optical microscopy was performed inside Micronova cleanroom to eliminate sample contamination and to enable high quality image capturing suitable for reliable image analysis. The cell deposition experiments were imaged with EVOS FL Cell Imaging System fluorescent microscope. The staining kit used for cell tracking was CellTracker Blue CMAC Dye, which was applied to the cell suspension before cell deposition. The fluorescent microscopy and image capturing were performed in a dark room to eliminate fluorescent stain degradation.

The secondary characterization method used was scanning electron microscopy (SEM). SEM was used to investigate cell-surface phase after deposition. The used SEM model was Zeiss Supra 40 situated inside Micronova cleanroom. After each cell deposition, the corresponding sample substrate was carefully diced into smaller pieces in order them to

fit into SEM chamber. Diced sample pieces were inserted into the chamber without applying any conductive coating and the SEM chamber was pumped into vacuum. It is unknown how exactly the vacuum condition affects the cells. Nevertheless, the vacuum condition was constant over all experiments, thus the vacuum effect was assumed to be the same over all experiments allowing comparison between the experiments.

6. Results and discussion

6.1. Hydrophilic-hydrophobic patterned microarray characterization

The SEM image in figure 26 shows the consistently formed pyramid-like structures of HB/HL surface, with base width around 1 to 1.5 µm and average height between 1 to 2 µm. The non-reflecting b-Si is impossible to image with visual spectrum of light, thus no optical microscope images are available. The fluoropolymer coating does not enhance the reflectance properties of b-Si.

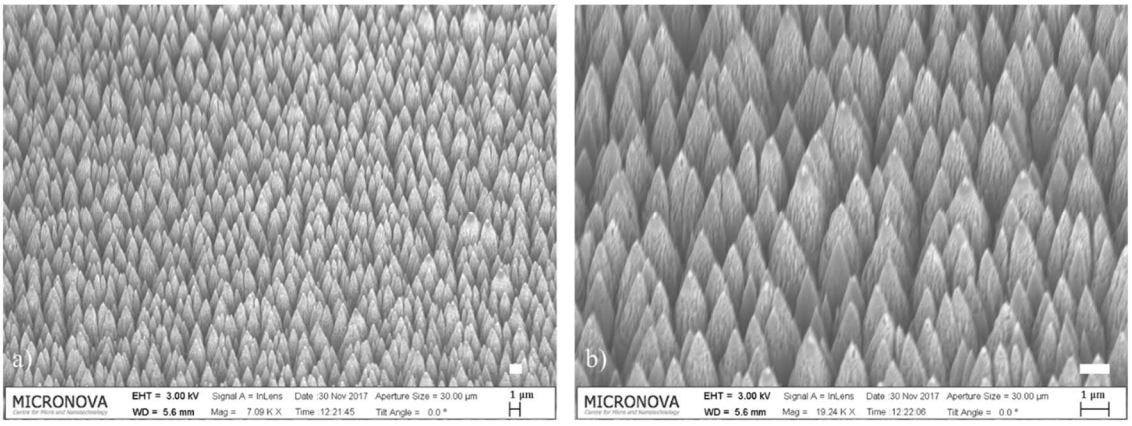

Figure 26: ab) SEM images of black silicon surface showing pyramid-like microstructure. The estimated pyramid base width is 1 to 1.5 µm and the estimated height is 1 to 2 µm.

The measured average receding contact angle on the hydrophobic area is 167°, advancing contact angle 169°, and contact angle hysteresis is 2°. This is considered as low. Contact angle measurements for the hydrophilic area (bare b-Si) proved difficult since the droplet spread on to the entire surface, hence apparent contact angle is determined to be zero degrees. According to the goniometer results, the fluoropolymer coated b-Si achieved superhydrophobic properties, which was also observable with bare eye due to water droplet completely sliding off of the surface if the wafer was even slightly tilted.

During the droplet deposition experiments, the mother droplet appeared to split into daughter droplets selectively only onto the hydrophilic spots, filling the spot area completely. Before the bridge between mother droplet and daughter droplet snapped, the mother droplet elongated and appeared to stick to the hydrophilic spot. If the forward motion was stopped manually, the droplet did not snap, and instead remained as undefined elongated shape. When the forward motion of the mother droplet caused the snapping to occur, the remaining daughter droplet adopted the form of spherical cap for a short period of time until it evaporated quickly (within a second, or so). Figure 27 shows a collection of images during the droplet deposition, demonstrating the consistent droplet

formation only to the hydrophilic spots, and the spherical cap shape of the daughter droplets. Furthermore, there is no significant visual difference in the daughter droplet size when the seeding velocity is low versus high.

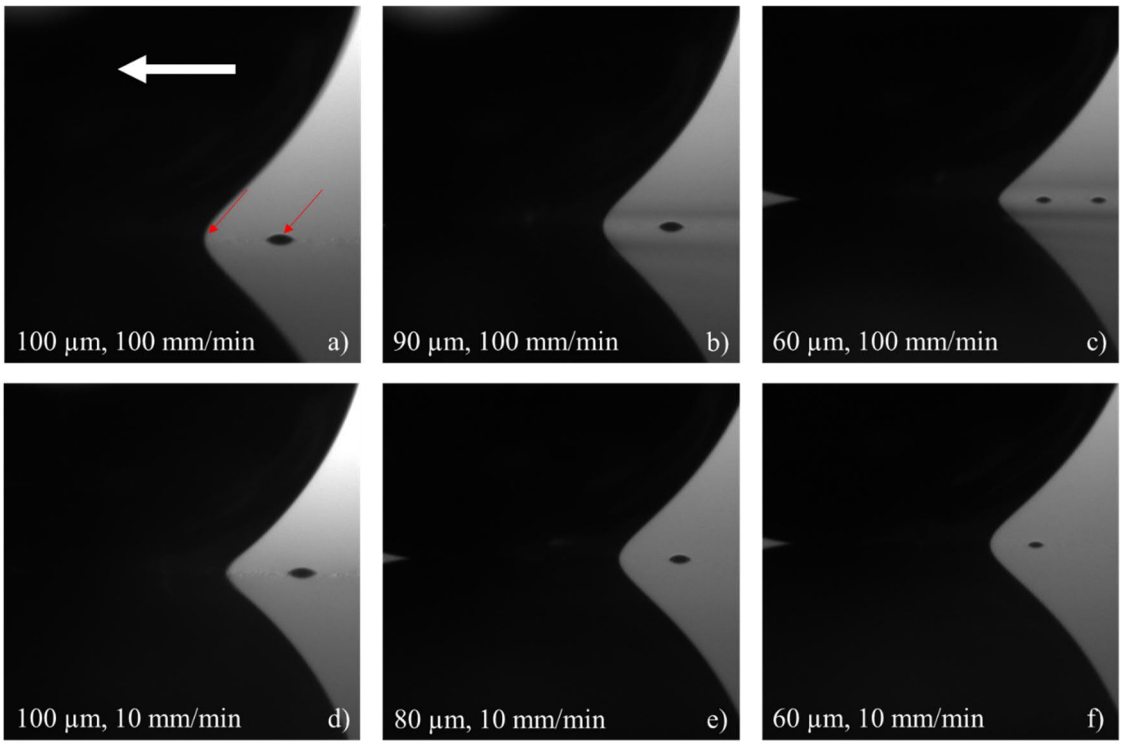

Figure 27: Collection of optical camera images right after the droplet fission. The daughter droplet forms consistently only to the hydrophilic spots. The white arrow on a) indicates the droplet movement direction. The left red arrow on image a) points to the receding edge, and the right red arrows points to the just-snapped daughter droplet deposited onto the hydrophilic spot. The white text on the bottom of each image indicates spot size and the seeding velocity used.

The volume of the daughter droplet was determined from series of still images taken with the goniometer optical camera assuming spherical cap shape. The height was measured from 5 different images per spot size to calculate the average droplet volume and standard deviation. The volume increases as a function of spot diameter. Cubed spot diameter and mean droplet volume demonstrate linear relationship, which is illustrated in the figure 28. Interestingly, the daughter droplet did not seem to be sensitive to the seeding velocity, although the limited image resolution most likely had an effect to the measuring accuracy. However, considering difference of one order of magnitude between the seeding velocities, the velocity does not demonstrate significant effect on the daughter droplet volume on this scale, since such difference should have been clearly visible with the image resolution available. This suggests that the time scale of daughter droplet "filling" is significantly smaller than the time-on-spot differences between 10 and 100 mm/min seeding velocity.

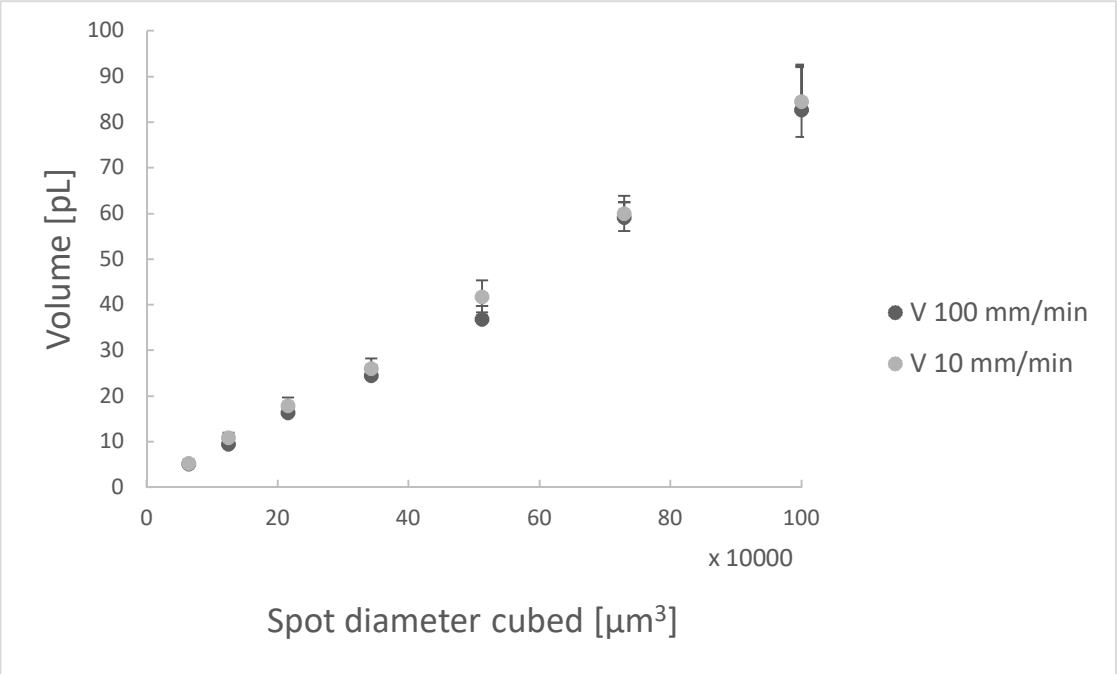

Figure 28: Daughter droplet volume as a function of spot diameter cubed displays linear relationship. The seeding velocity appears to not have any significant effect to the daughter droplet volume.

The 100 mm/min seeding velocity seems to generate slightly smaller droplets, which would be an opposite observation to findings in [28] where droplet volume is larger at higher seeding velocities. In [28], the droplet volume appeared rather constant between 60 and 200 mm/min seeding velocities, and only began to increase after that, and stabilize at 500 mm/min and above [28]. Also in that light, the droplet should not be expected to be different between 10 mm/min and 100 mm/min seeding velocities used here.

Overall, the droplet deposition experiments confirmed the validity of our pattered b-Si as a feasible material to systematically deposit well defined microdroplets on specified locations. Furthermore, the active seeding method functioned consistently and provided control over the mother droplet sliding velocity. The systematic daughter droplet deposition is best observed form a video, captured during deposition experiment; additionally, the consistency is also observable from the images obtained from the same experiment, represented in figure 27.

6.2. Single particle capture

In particle deposition trials most of the hydrophilic spots contained one or more particles after the so-called active seeding. Figure 29 shows a collection of images resulting from deposition trials with 10 mm/min seeding velocity and different spots sizes, using 10 µm polystyrene particles. For example, 30 µm spots depicted in figure 29a seems to confine

one or maximum of four particles per spots, while 80 µm spots depicted in figure 29f contains ten or more particles per spot. Clearly the spot size limits the amount of particles on a single spot.

Figure 30 depicts images from deposition trials with 100 mm/min seeding velocity with same spot size interval as used in trials depicted in figure 29. The particle size is 10 µm. By comparing for example figure 29d and figure 30d, in figure 29d nearly all of the spots are completely filled with multiple particles while same sized spots in figure 30d are clearly not as full. Total fill rate was calculated by dividing the number of spots with any number of particles with total number of spots within the seeding droplet trace. In 80 µm spots, the fill rate was nearly 100% in both seeding velocities, and at slow seeding velocity the fill rate remained at near 100% from largest to smallest spot size. By contrast, in high seeding velocity trials, the fill rate seems to drop as the spots size decreases, and at 30 µm (figure 30a) spots, the fill rate is only about 50%.

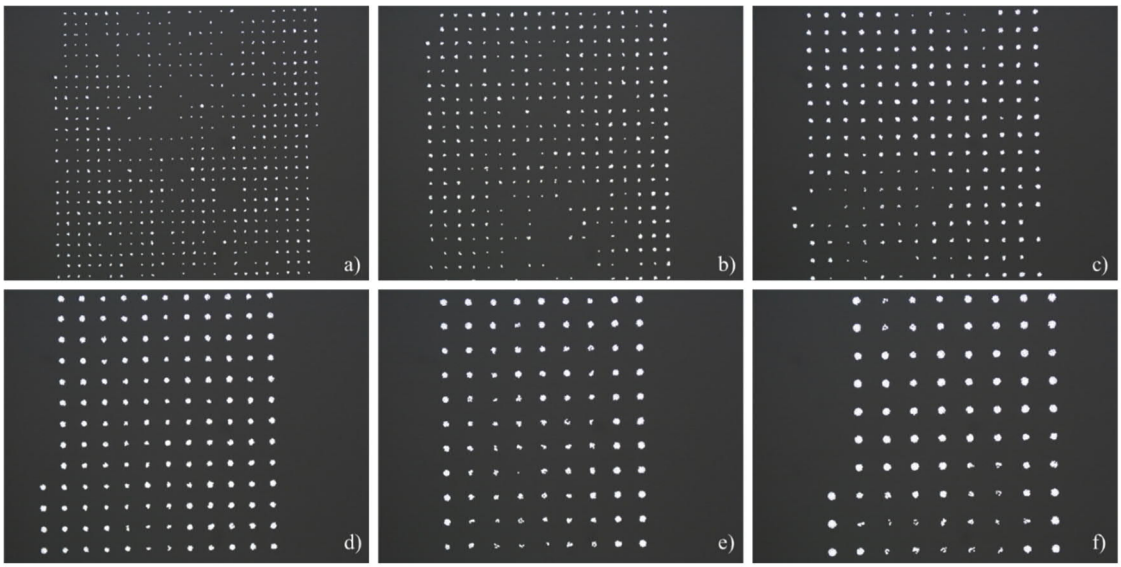

Figure 29: Collection of optical microscopy images (5X magnification) of deposited 10 µm particles by using 10 mm/min seeding velocity. The spot size from a) to f) is 30, 40, 50, 60, 70, and 80 µm respectively. The image collection displays that the spot size limits the amount of particles per spot and that the fill rate is constant in all images. This indicates that the fill rate is independent from spot size at 10 mm/min seeding velocity.

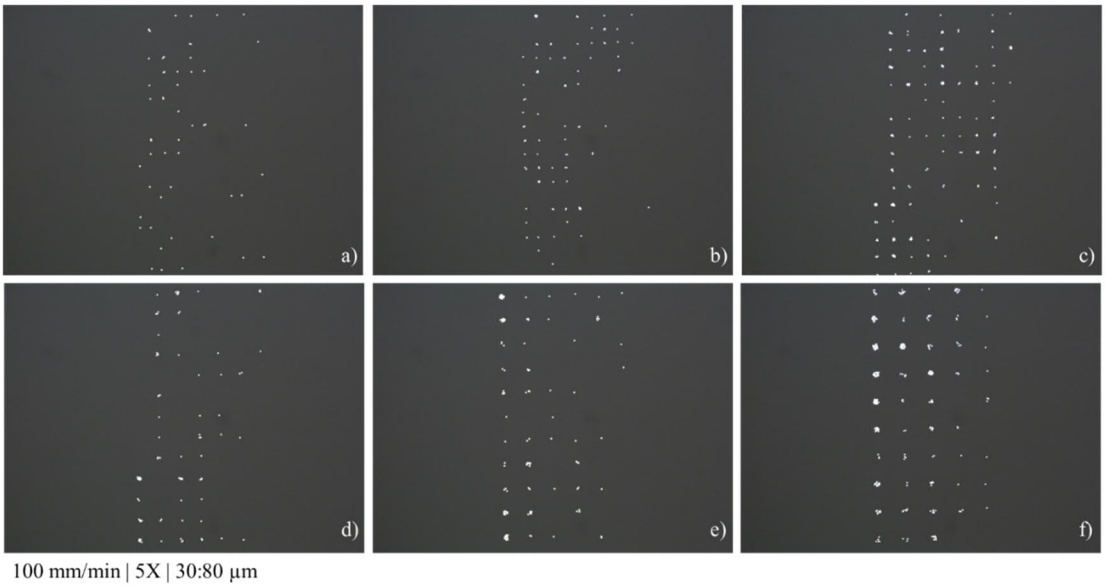

Figure 30: Collection of optical microscopy images (5X magnification) of deposited 10 µm particles by using 100 mm/min seeding velocity. The spot size from a) to f) is 30, 40, 50, 60, 70, and 80 µm respectively. The fill rate is approximately constant and independent on spot size between all images from a) to f).

To examine the underlying cause behind the differences between fill rates using different seeding velocities, time-on-spot and deposition frequency plots were formulated. Figure 31 depicts mother droplet time-on-spot as a function of spot size and seeding frequency as a function of spot size. The difference in time-on-spot is one decade between the used seeding velocities, consequently the frequency difference is one decade. The frequency is calculated by multiplying time-on-spot and seeding velocity, and it can interpreted as droplet generation rate. High droplet generation rate and low time-on-spot in high seeding velocity can be associated to the time window when the transient capillary bridge between the mother droplet and each hydrophilic spot is open. Since the capillary bridge is supposed to be the only physical pathway for particle migration, it is clear that the time window between opening and closing of the capillary bridge is related to the absolute number of particles that can migrate. According to these results here, the previous reasoning seems reasonable, since short time capillary bridge results in lower number of particles per spot, which can be observed by comparing figures 29 and 30, and corresponding time-on-spot and droplet generation plots in figure 31.

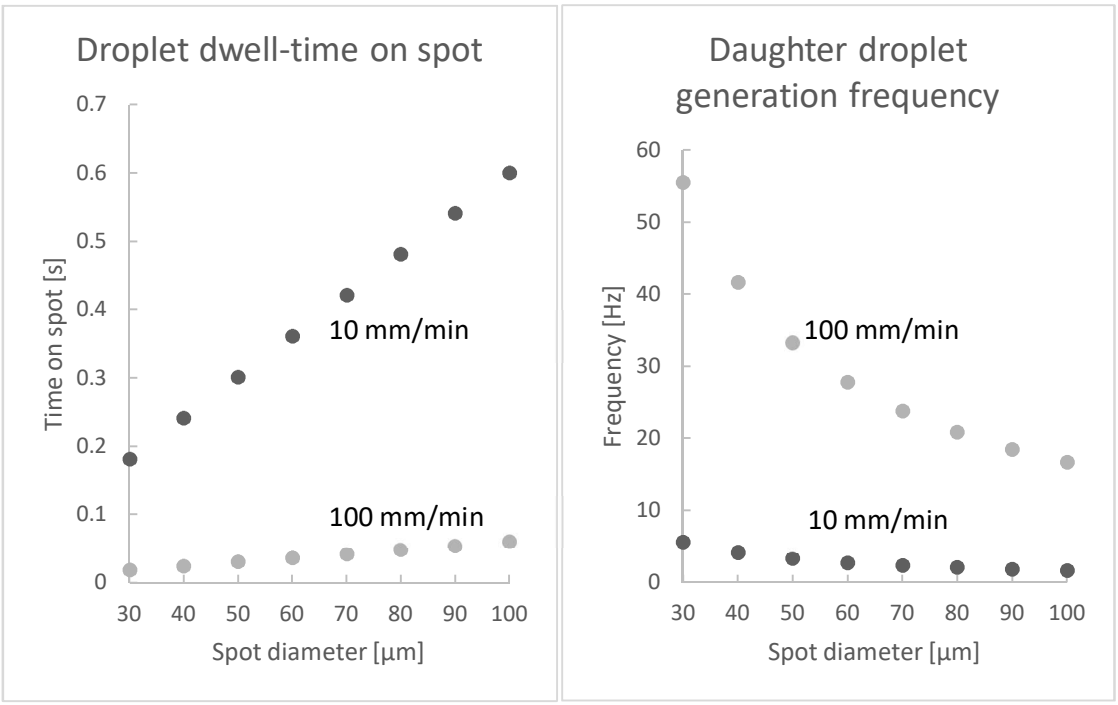

Figure 31: a) Seeding droplet time on spot. In slower seeding velocity the droplet spends more time on spot. b) Daughter droplet generation frequency (time on spot multiplied with seeding velocity) demonstrates significant difference between seeding velocities with smaller spot sizes. The difference decreases when spot size increases.

According to these results, the active seeding mechanism paired with HB/HL appears to be a feasible method for particle deposition. The spot size clearly provides control in terms of limiting the number of particles within one spot, while seeding velocity can be interpreted as HB/HL efficiency. According to these experiments, the spot size appears to be superior parameter to control number of objects captured per spot, and it is insensitive to the seeding velocity. Seeding velocity can also be used as a control parameter to adjust number of particles per spot; however, it is sensitive to spot size, and due to high droplet generation rate (short open capillary bridge time window), the efficiency can diminish at small spot sizes.

The next set of experiments investigated the optimization of the particle size / spot size ratio. Figure 32 depicts two images from particle deposition trials where 10 µm particles were captured on 20 µm hydrophilic spots (i.e., 1 to 2 ratio), with seeding velocity of 10 mm/min and 100 mm/min. Bare eye observation reveals that the total fill rate is approximately twice as high at low seeding velocity (figure 32a), compared to high seeding velocity (figure 32b). This result is consistent with the previous trials with larger spot sizes.

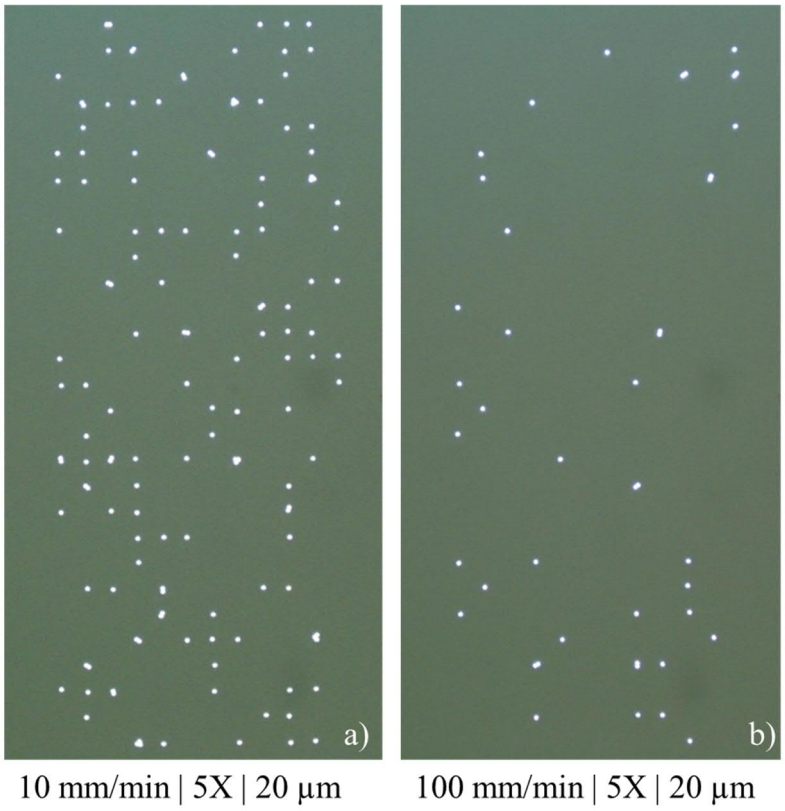

Figure 32: Optical microscopy images (5X magnification) of deposited 10 µm polystyrene particles on 20 µm hydrophilic spots. a) Using 10 mm/min seeding velocity approximately half of the spots are occupied by particles. b) Using 100 mm/min seeding velocity most of the spots are empty, and the fill rate is significantly lower in comparison to slow seeding velocity seeding in a).

The particle capture distributions are illustrated in figure 33 obtained via particle recognition and counting via image analysis. The results show that approximately 27% of the spots contained single particle at 10 mm/min seeding velocity, while the corresponding statistic was 9 % in 100 mm/min seeding velocity. This result indicates that the single particle capture efficiency is three times higher at low seeding velocity, in comparison to high seeding velocity. Furthermore, the number of doubles and triplets were relatively low and the ratio between singles and doubles were approximately 80/20 in both trials, independent of particle and spot size as long as the ratio between them was 1:2.

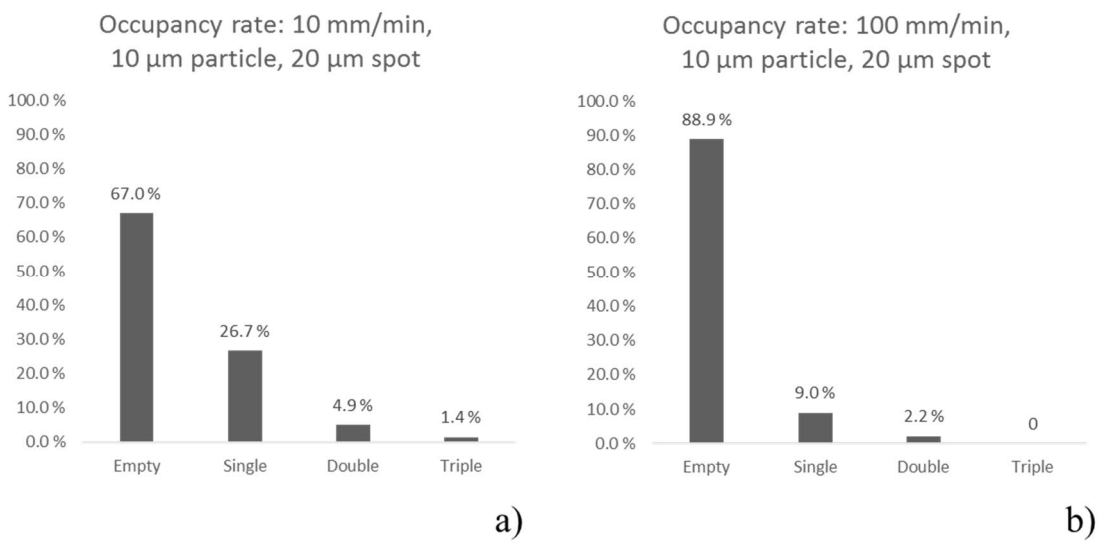

Figure 33: a) Occupancy rate using 10 mm/min seeding velocity, 10 µm particles, and 20 µm hydrophilic spots. b) Occupancy rate using 100 mm/min seeding velocity, 10 µm particles, and 20 µm hydrophilic spots.

Results from Particle deposition trials with 20 µm particles are collected in figure 34. The 1-to-2 ratio trial with factor of two increase in particle and spot sizes resulted similar distribution (figure 34a) than 10 µm to 20 µm experiments. However, even after multiple trials, the double particle cases were completely mitigated, and only single particles were observed. This did not directly translate into improved overall fill rate as it decreased from 33% to 23%. However, the single-particle occupancy rate remained at the same level and dropped only from 26.7% to 23%. The lack of double particles could partly be due to smaller standard deviation in large particle diameter, in comparison to smaller particle diameter, which was observed some times, but not measured.

Increasing the spot size by 10 µm appeared to increase the fill rate (figure 34b) from 23% to 69%. Single particle cases represented 54% of the total distribution, while the ratio between single and double cases was roughly 75/25, respectively. Nevertheless, the 1 to 2 ratio experiment with larger particles provided consistent results and provided further evidence of spot size working as superior control parameter in terms of adjusting number of objects captured per spot.

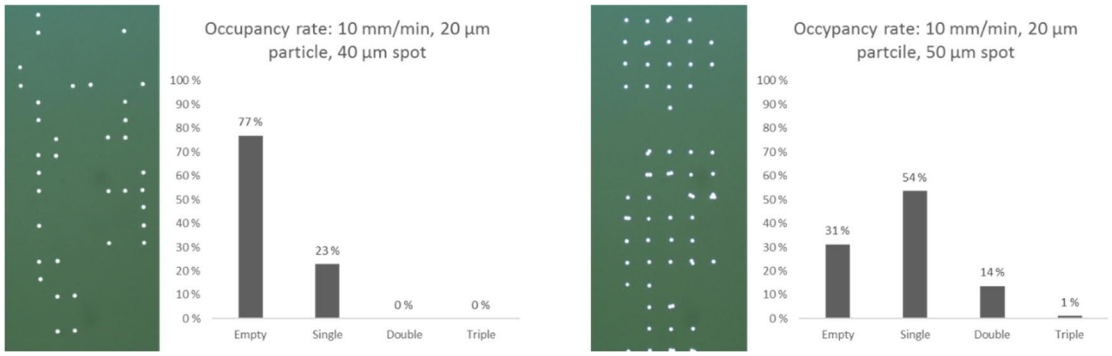

Figure 34: Composite images of optical microscope images and occupancy rate diagrams. Left: Occupancy rate using 10 mm/min seeding velocity, 20 µm particles, and 40 µm spots showing zero double and multiple particle depositions. Right: Occupancy rate using 10 mm/min seeding velocity, 20 µm particles, and 50 µm spots demonstrates extremely high single cell occupancy rate, but showing high double particle occupancy rate, too.

The comparison between empirical occupancy rate distribution, distribution predicted by Markov model, and distribution predicted by Poisson distribution with expected value 0.5 is presented in figure 35. The two distributions, empirical and simulated, shows clear similarities between one other. The Markov model which was adjusted with 30% reduced particle immobilization probability seems to work best. The reduced immobilization probability represents the event where once "immobilized" particle do not necessarily stick to the spot permanently, but is prone to rinsing effect by the receding edge. However, such event was not observed in any of the experiments due to lack of suitable imaging equipment. Markov model and Poisson distribution predict almost identical occupancy rate distributions when expected value is fixed to 0.5 in Poisson distribution. The triple-particle state was not defined in the Markov model, thus it does not predict it unlike Poisson process (figure 35). These results suggest that the particle deposition events are independent, since independence is a key assumption in Poisson distribution and a key property of Markov chain model.

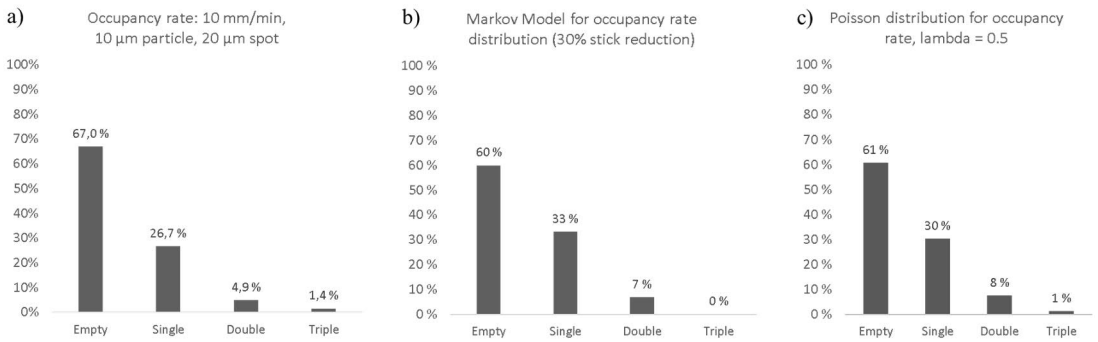

Figure 35: Comparing empirical (a), Markov model predicted (b), and Poisson distribution with expected value 0.5 (c) occupancy rate distributions. The comparison displays high similarity between the distributions.

The assumed particle chain formation to the receding edge of the seeding droplet was indirectly confirmed by imaging evaporating sessile droplet on HB/HL. While it does not represent the moving droplet case, it shows that particles tend to form chains which could be counted, starting from the receding edge of the droplet. Figure 36 shows images and points out the so-called primary and secondary deposition chains, which are the first underlying assumptions in the Markov model geometric examination (figure 19). One clear difference is that the shape of the receding edge is not straight and constant, instead it is arc-like and changes over time.

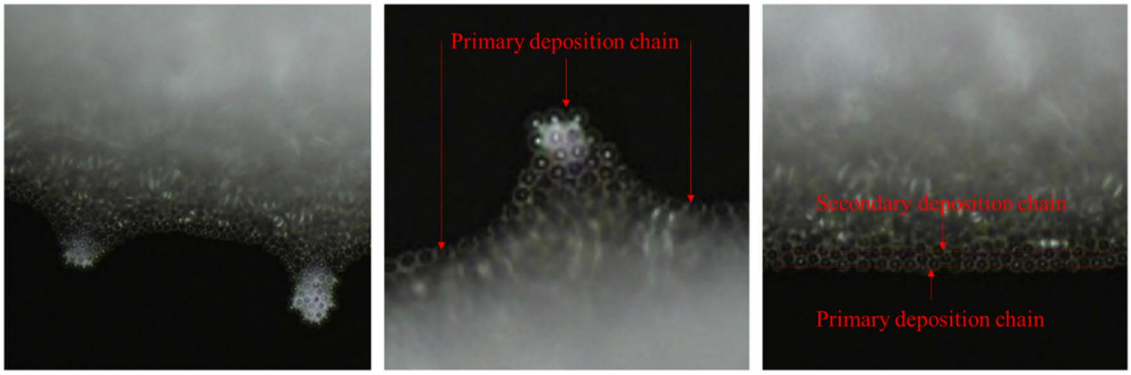

Figure 36: Optical microscopy images of an evaporating water droplet containing 10 µm particles. Left: an overview image depicting the elongated droplet from the points where the droplet has attached to the hydrophilic spots. Center: close-up image displaying the continuous primary deposition chain. Right: Overview image showing the primary and secondary deposition chain layered side-by-side.

The comprehensive particle capture experiments provide clear evidence that HB/HL can be used as a single particle capture device. Furthermore, the investigation provided new knowledge how to adjust the number of particles captured per spot. The spot size works as a robust parameter to limit the amount of particles per spot to one, and it simultaneously mitigates double and multiple particle cases. If the particles to-be-captured are well defined and consistent in terms of size (diameter), the 1 to 2 design principle can eliminate the double cases completely, and selectively capture only single objects. The Markov model did not predict such a case; however, if the geometric examination is reviewed and the discretization interval increased from 10 to 100, it already increases the single/double ratio significantly. It can be further deducted that by increasing the discretization interval from 1 to infinity, the amount of doubles approaches but never reaches zero.

Seeding velocity clearly has an effect on the single particle occupancy rate as well. Moreover, seeding velocity has significant effect on the fill rate of the HB/HL array. The higher the seeding velocity, the lower the fill rate was. This can be attributed to the differences in time-in-spot and droplet generation rates, which directly translate into differences in

the existence time of the transient capillary bridge between the mother droplet and the hydrophilic spot(s). The shorter time window can be a significant factor in terms of particle migration, i.e., the particles have less time to move from the mother droplet to the spot. However, such particle migration events were not directly observed.

The particle size has direct effect to the terminal sedimentation velocity according to Stokes's law (equation 7). Stokes's law was applied to elaborate a scenario, where sedimentation is the only driver which brings particles to proximity with the surface (leading to deposition). Results for 10 µm particles and 10 mm/min seeding velocity are collected in the table 3 below.

Table 3: Calculating maximum distance for 10 µm particle in the scenario when sedimentation would be the driving force in particle deposition, using Stokes's law (equation 7). Maximum distance is only 0.62 µm, when mother droplet lingers 0.24 seconds on top of a spot (10 mm/min seeding velocity).

Particle radius	0,000005	m
g	9,81	m/s^2
Particle density	1050	kg/m^3
Water density	1000	kg/m^3
Water viscosity	0,00105	kg/ms
Terminal velocity	**2,60**	**µm/s**
Number of 20 µm spots in line	250	
Seeding velocity	10	mm/min
Mother droplet time-on-spot	0,24	s
Sedimentation distance	**0,62**	**µm**

For successful deposition, the particle would have to be within 0.6 µm range should the sedimentation be the only factor driving particles downwards. This range it is ten times smaller when 100 mm/min seeding velocity is used. Same distance for 20 micrometer particle is 2.5 µm. This result gives more confidence to the proposed deposition chain formation to the receding edge of the seeding droplet due to forward motion induced flow pattern within the droplet. That is, the particles linger and possibly agglomerate to the far

bottom end of the seeding droplet where they are ready to migrate on to a spot when the transient capillary bridge is formed.

6.3. Single cell capture

Using HB/HL as a single cell capture device is expected to obey similar underlying factors that governs the HB/HL performance as a single polymer sphere capture device. However, there are few critical differences between polystyrene particles and cell which requires some consideration. First, the polystyrene particles are rigid, while cells as deformable. Second, the polystyrene particle surface is non-adhesive and its surface is well defined, while cell surface is complex and varies between cell types. In their natural environment (i.e., blood circulation), white blood cells are supposed to flow freely without attaching to blood vein walls when the host is healthy. However, when local inflammation occurs, the blood vein wall surface undergoes such change in surface chemistry from that local part that it tends to immobilize passing white blood cells. Furthermore, the initial triggering of some adhesion molecules extending from white blood cell is sensitive to shear forces which is related to blood flow rate.

Figure 37 depicts an optical microscopy image of a peripheral blood mononuclear cell (PBMC) suspension droplet released on top of a HB/HL. The white circular objects (figure 37, some indicated with red arrow) are white blood cells, and by comparing the size of each cell, the difference in diameter is clearly visible. In general, peripheral blood mononuclear cell population diameter is approximately normally distributed [62, 63]. According to particle capture test, the non-uniform size distribution can pose a challenge in terms of finding optimal spot size to selectively capture single cells only.

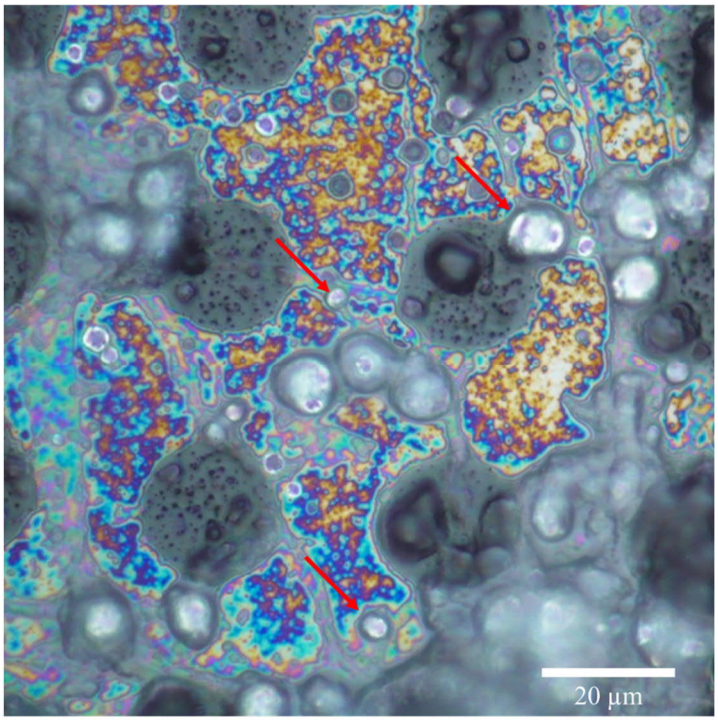

Figure 37: Sessile PBMC suspension droplet on HB/HL surface. Circular white items are cells. Red arrows point different size cells, which shows that the cell size distribution is non-uniform.

6.3.1. Single cell capture using primary cells and black silicon (experiment 1).

Figure 38 shows a collection of fluorescent microscopy images from single PBMC capture trials of the first experimental round. The spot size was kept constant at 20 µm, while seeding velocities were 10, 30, 50, and 70 mm/min, from figure 38a to figure38d respectively. The seeding velocity effect on fill rate can be clearly observed and it appears consistent with similar particle capture experiments. Another observation is that at lowest seeding velocity (figure 38a) some of the cells seems to form bridges between consequent spots, while at higher velocities number of such bridges is lower.

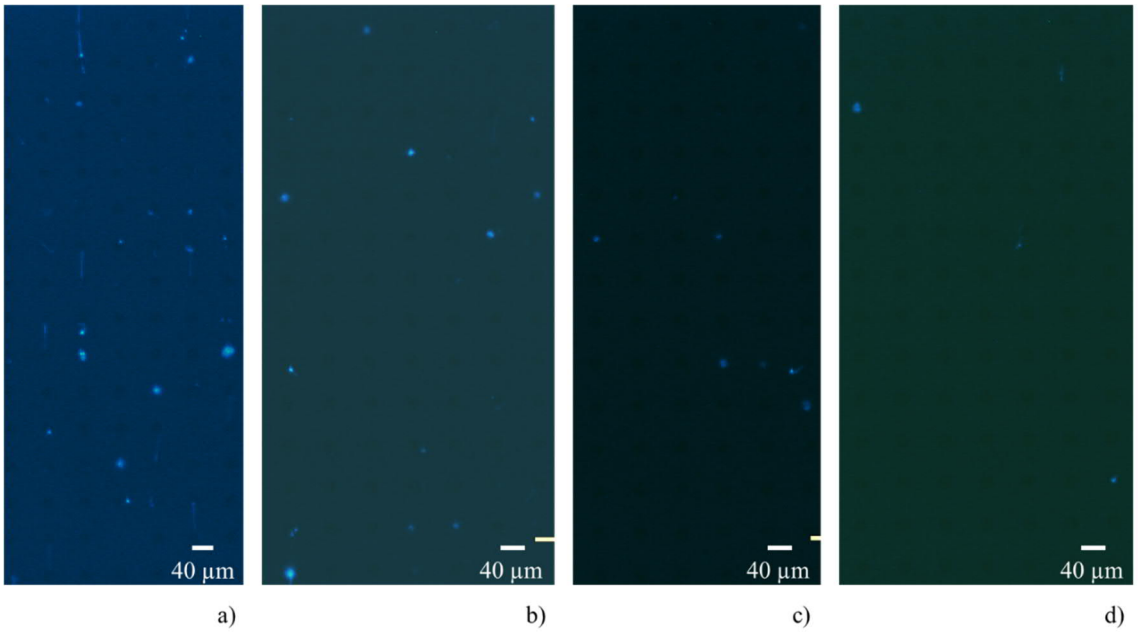

Figure 38: Fluorescent microscopy images of PBMC deposited on 20 µm hydrophilic b-Si spots. a) 10 mm/min seeding velocity. b) 30 mm/min seeding velocity. c) 50 mm/min seeding velocity. d) 70 mm/min seeding velocity. Occupancy rate decreases when seeding velocity increases.

The single cell occupancy rate as a function of seeding velocity is presented in figure 39. In this experiment, the single cell occupancy rate (and fill rate) seem to decrease linearly as a function on seeding velocity. However, the lack of data prevents robust conclusion about the relationship between seeding velocity and single cell occupancy rate from this experiment. Nevertheless, according to particle capture experiments the decrease in filling rate at higher seeding velocities seems sensible result.

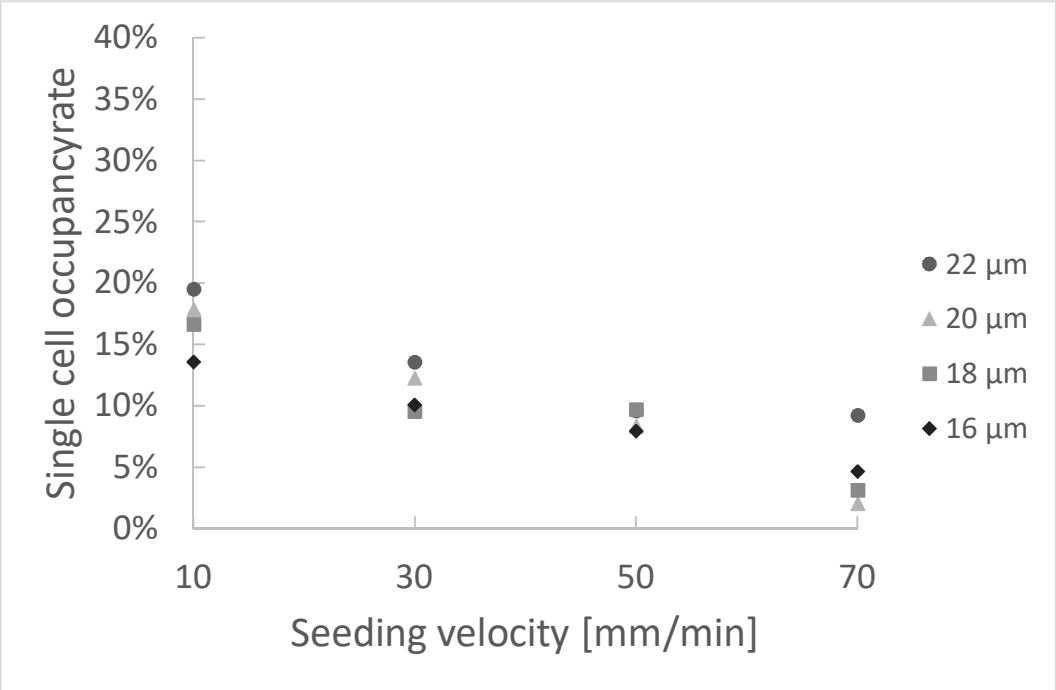

Figure 39: Physical experiment of single cell occupancy rate as a function on seeding velocity showing decreasing trend when seeding velocity increases. The single cell occupancy rate does not display so clear linear effect as a function of spot size. Legend indicates the spot size.

The spot size seems to have a minor effect into the occupancy rate. An averaged single cell occupancy rate was used to increase the statistical power of the analysis. A linear regression analysis was performed and 95% confidence intervals (CI) was calculated for intercept, slope, and coefficient of determination. Figure 40 shows the scatter plot and the fitted regression line.

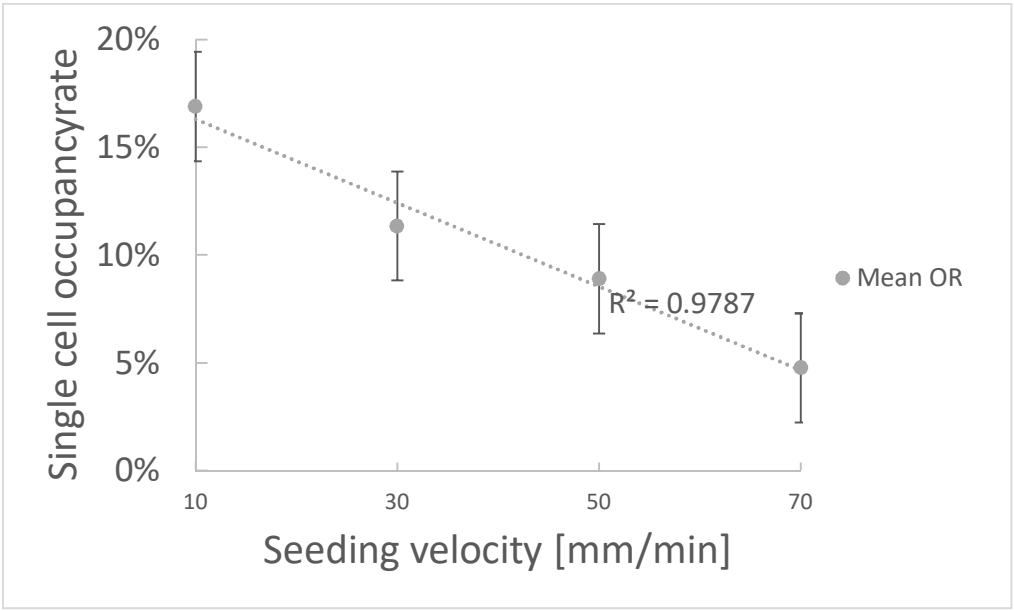

Figure 40: Physical experiment of average single-cell occupancy rate between spot sizes 22, 20, 18, and 16 µm predicted with univariate linear regression using seeding velocity as predictor. Dashed line is the fitted linear regression line. Single cell occupancy rate shows clear linear dependence on seeding velocity.

The regression coefficient for the slope is -0.19 (CI -0.28 : -0.10) which indicates that the occupancy rate drops by 0.20 when velocity increases by one. The slope is statistically significant with p-value 0.01. Coefficient of determination is extremely high 0.97 (CI 0.96 : 0.99), which indicates that seeding velocity is a critical factor affecting to single cell occupancy rate. This high coefficient of determination is rare, but considering the context, seeding velocity is the only known variable, since spot size functions more a limiting factor than true variable. Also, the underlying physical phenomenon supports this relationship. Moreover, the result indicates that the process is systematic rather than random.

6.3.2. Single cell capture using PBMC cell line and black silicon (experiment 2).

The second round of single-cell capture experiments was a replication of the first experiment round. The aim was to confirm the previous results, and on the other hand to investigate the cell-surface phase when the deposition process is complete. The images from second round of experiments with same experimental setting as round one are presented in figure 41. Figure 41a to figure 41d are images from PBMC deposition trials with seeding velocity of 10 mm/min, and spot sizes 22 µm, 20 µm, 18 µm, and 16 µm, from a to d, where 22 µm spots size seems best in term of single cell occupancy rate (and fill rate). Figure 41e to figure 41h depicts images from similar cell deposition trials with 50 mm/min seeding velocity. Interestingly, the fill rate is now significantly higher with high seeding velocity, in comparison to low seeding velocity, opposite to previous observations.

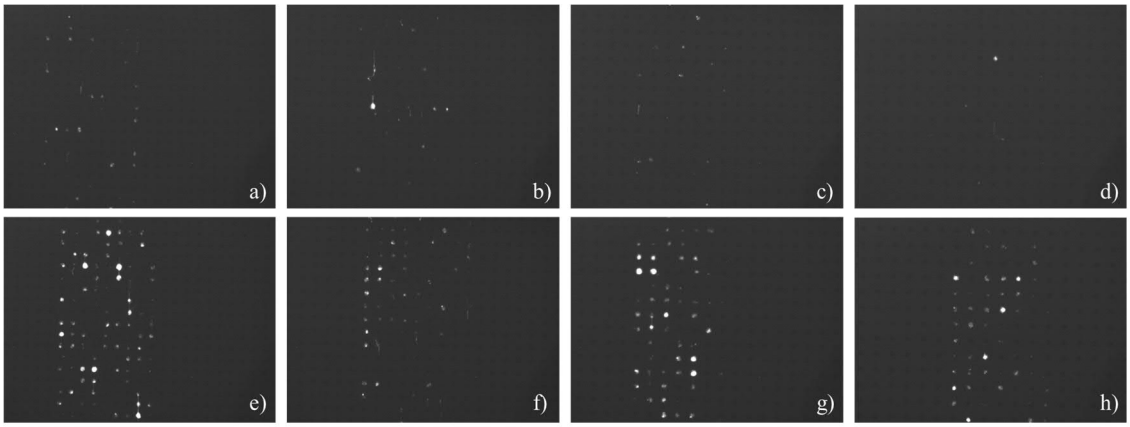

Figure 41: Deposited PBMC on hydrophilic b-Si spots. a) 22 µm spot size. b) 20 µm spot size. c) 18 µm spot size. d) 16 µm spot size. a, b, c, and d) seeding velocity 10 mm/min. e) spot size 22 µm. f) spot size 20 µm. g) spot size 18 µm. h) spot size 16 µm. e, f, g, h) seeding velocity 50 mm/min.

The calculated single cell occupancy rate as a function of seeding velocity from the round two experiments are presented n figure 42. The mean values are calculated from at least three data points per velocity / spot size pair. The relative standard deviations are in the range of 5 – 10 % (error bars not drawn in plot). The lowest (10 mm/min) seeding velocity seem to result poor occupancy rate and as such it remains in its own class, while 30 mm/min and above seeding velocities are within the same range relative to each other and result high occupancy rates. Furthermore, the spot size displays slightly inconsistent behaviour, but overall stays tightly grouped except on the highest seeding velocity case.

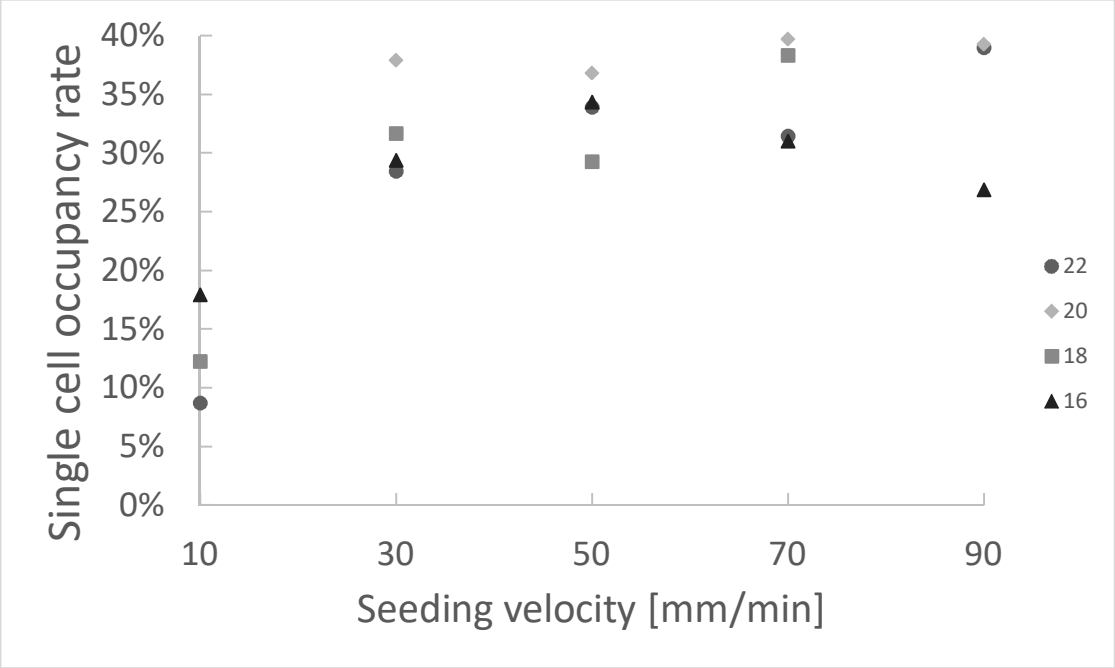

Figure 42: Physical experiment of single cell occupancy rate as a function of velocity and different spot sizes. The relationship do not demonstrate clear linear relationship between single cell occupancy rate and seeding velocity.

Increasing seeding velocity beyond 30 mm/min does not demonstrate any improvement in terms of single cell occupancy rate. Increased seeding velocity most likely translates into increased flow rate inside the seeding droplet, which could induce higher shear stress in the cell-substrate system, analogous to a fluid flow in a pipe. However, some literature sources claims that leukocyte (one type of white blood cell) adhesion is decreased when shear stress is increased [64], while some sources claims the opposite [65]. The discrepancy can be attributed to the complex nature of white blood cell adhesion in general, and that more than one type of adhesion molecules are involved in the cell adhesion / leukocyte extravasation [66, 67].

Another scenario is that since the experiments were carried from slowest-to-fastest order, the 10 mm/min are biased due to low time of cell sedimentation, i.e., there are fewer cells on the bottom of the mother droplet where the cells migrate to the spot. However, the cell suspension was pumped in-and-out between changing the seeding velocities to avoid such bias caused by sedimentation time.

Linear regression analysis was conducted for average single cell occupancy rate predicted by seeding velocity. Regression coefficient for the slope is 0.07 (CI -0.06 : 0.2) which means that the velocity has only a minuscule effect on occupancy rate. Furthermore, confidence intervals have opposite signs, which indicates that this is not a statistically significant finding, since it would mean that the relationship can be negative or positive. The adequately high coefficient of determination 0.49 demonstrate confidence intervals from 0.05 to 0.96, which can be interpret such that either the model explains everything or nothing. This result does not support linear relationship between seeding velocity and single cell occupancy rate. Instead, these results support uniform distribution of single cell occupancy rate at seeding velocity interval from 10 to 90 mm/min. Figure 43 displays scatter plot and fitted regression line with standard error bars.

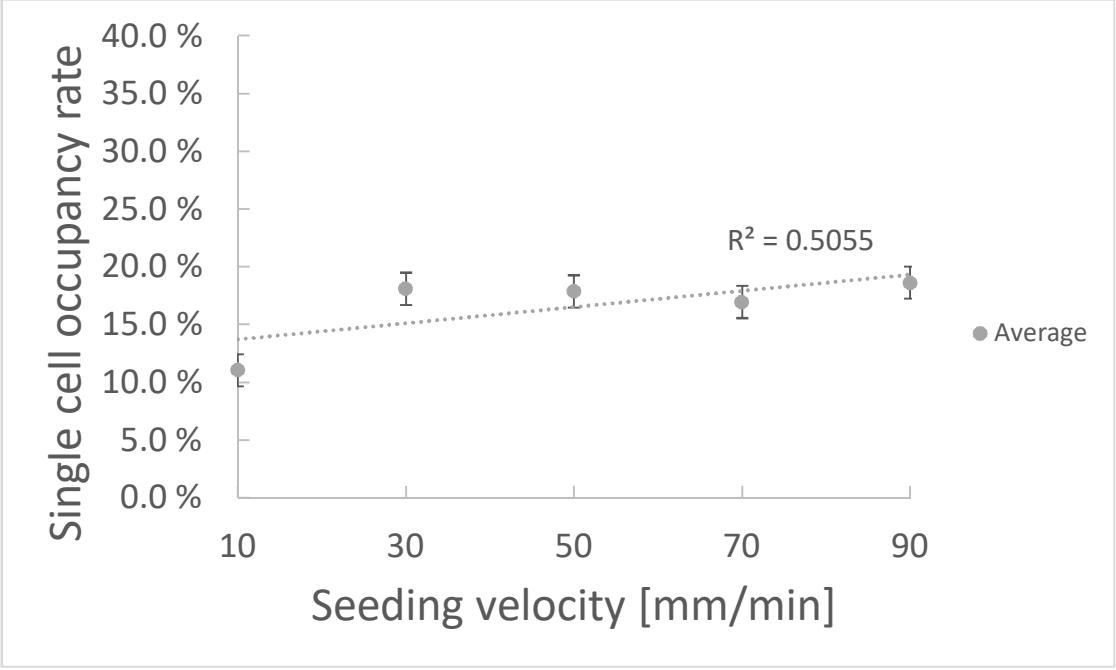

Figure 43: Physical experiment of average occupancy rate between 22, 20, 18, and 16 µm spots predicted by seeding velocity using linear regression. Dashed line is the fitted regression line. In this experiment, the single cell occupancy rate do not demonstrate systematic linear dependence: R^2 = 0.50 (95% CI: 0.05 – 0.96).

Closer look of a cell on a hydrophilic spot was obtained with SEM. Figure 44 depicts SEM images (taken one day after the deposition) from cell deposition trials of experiment

round one, where the white arrow indicates the movement direction of the seeding droplet. The captured cell is immobilized to the edge of the hydrophilic spot (lighter grey areas represents hydrophilic spots), while some extrusion extends to consequent spot and stops there.

The extrusion extends along the seeding direction. The hypothesis is that, once the cell has migrated from the mother droplet to a spot via capillary bridge, the forward motion of the seeding droplet continues; and, any extrusion can continue along until encountering next spot in line, after which the extrusion tip is immobilized onto it. The extrusion poses inter cellular contamination risk which is critical to avoid in single cell analysis. Cell bridging can be avoided by increasing the distance between spots, and at 4x spacing bridges between spots did not occur. Furthermore, the extrusion seems to lay on top of black silicon spikes (figure 44a and b), i.e., it is not conformal, while the cell on the spot appears to be penetrated by the black silicon spikes and / or obtained the black silicon spike topography.

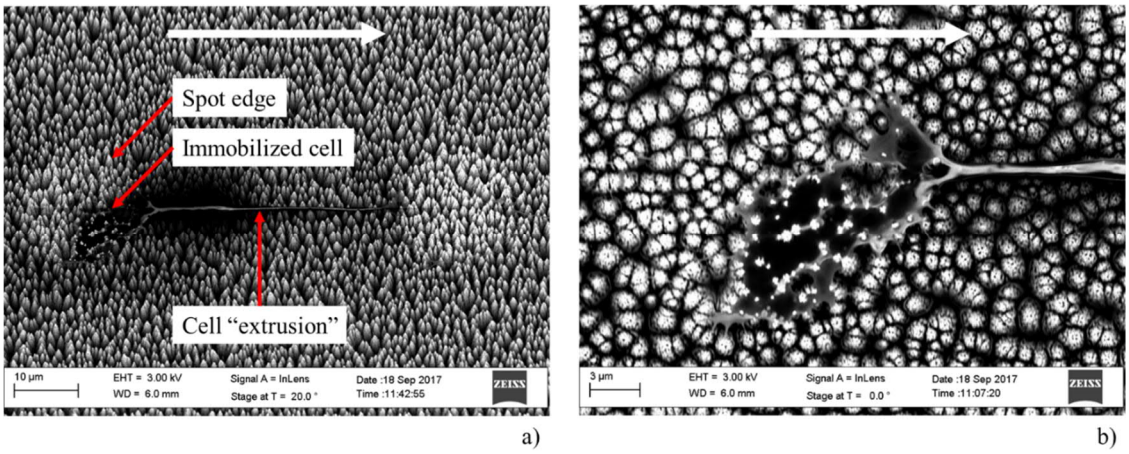

Figure 44: SEM images of deposited PBMC 24 hours after the deposition. a) (20º tilt) White arrow indicates the seeding direction. Single immobilized cell is visible in the left spot, while some type of extrusion is extending to the right spot. b) (0º tilt, top view) close-up image of the deposited PBMC is possibly penetrated by the b-Si nano-spikes. Some minor extrusions are visible in the back-end of the cell, which are possibly initial anchoring points.

Should the black silicon nanospikes induce mechanical penetration of the cell, the cell would undergo cell lysis, i.e., cell would die [68]. SEM images presented in figure 45 from experiment round two were obtained immediately after the cell deposition to investigate the cell evolution on HB/HL over time. The cells were typically situated closer to the edge of hydrophilic and hydrophobic area rather than at the centre of the spot. Cells in figure 45a and 45b have retained their spherical shape; however, the tilted SEM image

in figure 45b reveals that the cell has begun to adopt the black silicon spike topography and sank into pyramid trenches.

According to [69], bacteria cell lysis rate increases over time, i.e., initially, the entire bacterial cell population is alive, and they are gradually lysed on top of black silicon substrate. While bacteria and cells are not directly analogous, the possibility of black silicon induced cell lysis cannot be neglected without further confirmation. Furthermore, the black silicon induced mechanical cell lysis could be beneficial in single cell analysis application, since cell would have to be lysed to expose the mRNA from the nucleus.

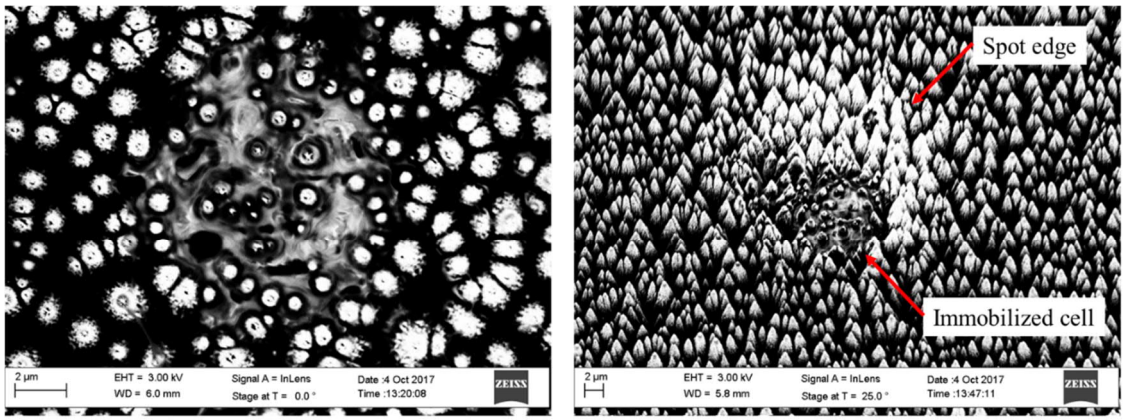

Figure 45: SEM images of deposited PBMC immediately after the cell deposition. a) (0° tilt) PBMC has retained its spherical shape. b) (25° tilt) The deposited cell has possibly been penetrated by b-Si nanospikes and begun to adopt the underlying topography.

6.3.3. Single cell capture using THP-1 cell line and planar silicon (experiment 3).

Third round of experiments investigated the alternative HB/HL where the hydrophilic spots were planar silicon instead of black silicon. Furthermore, the cells used in round three were from THP-1 cell line. Figure 46 presents a collection of images with 20 µm spots size and various seeding velocities (from a) to e), 10, 30, 50, 70, and 90 mm/min, respectively). With planar spots, the cell seemed to be more centred with respect to the spot. Furthermore, cells appeared more circular, i.e., retained their original shape, when compared to black silicon experiments. However, the experiment round 1 and 2 used primary white blood cells, while cells from cell line were used in round 3 deposition trials.

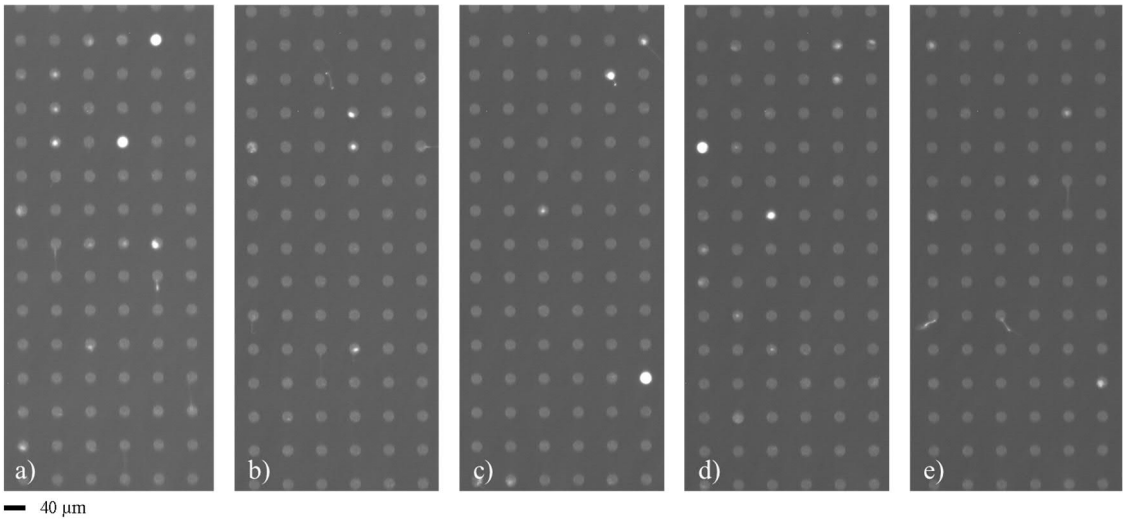

Figure 46: Fluorescent microscopy images of THP-1 cells deposited on hydrophilic planar-Si spots. a) 10 mm/min seeding velocity. b) 30 mm/min seeding velocity. c) 50 mm/min seeding velocity. d) 70 mm/min seeding velocity. e) 90 mm/min seeding velocity. Single cell occupancy rate does not show any significant trend when seeding velocity increases.

The single cell occupancy rates are calculated and presented in the figure 47. This time the occupancy rate decreases when seeding velocity is increased from 10 mm/min to 50 mm/min, which is consistent with particle deposition trials. At 70 mm/min and 90 mm/min the occupancy rate seems to increase: however, the standard deviation is quite high and inconsistent between the seeding velocities which is possibly due to low sample number (three sample images per seeding velocity). Nevertheless, the single cell occupancy rate stays around 10 %, which is about twice as low as in particle deposition trials, and at least three times lower in comparison to best results from single cell capture experiments on round two (figure 42). Few to no doubles at all (or multiple) were encountered in round 3 experiments. A linear model was fitted to this data as well. The results did not indicate anything statistically significant (coefficient of determination 0.34, CI 0 – 0.97), suggesting that the relationship is non-linear. This results is consistent with the second experiment round.

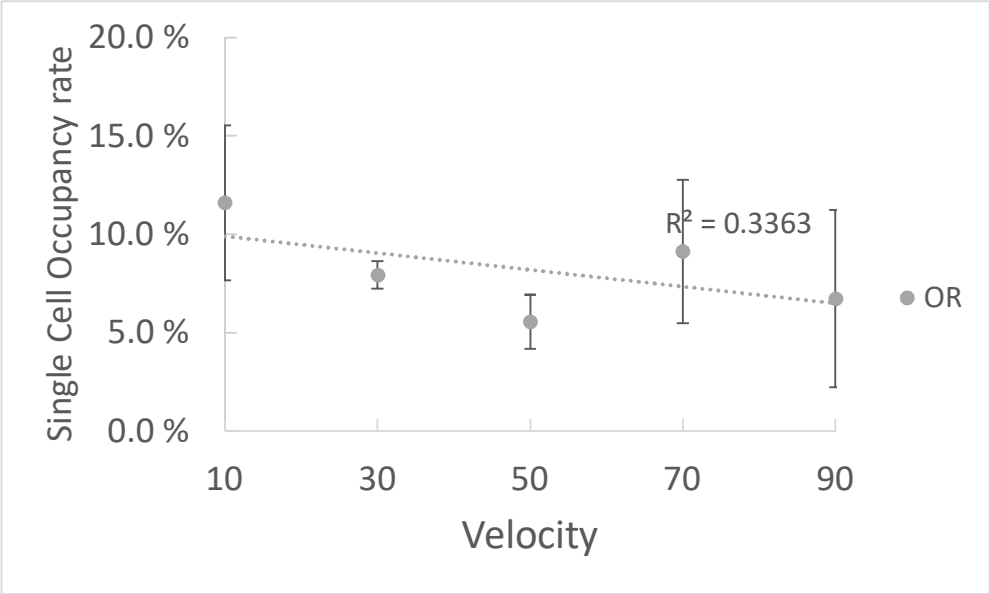

Figure 47: Physical experiment of mean single cell occupancy rate in 20 µm planar-Si spots predicted by seeding velocity using univariate linear regression. There is no systematic linear dependence between the single cell occupancy rate and seeding velocity.

SEM images depicted in figure 48 confirm that the cells are mostly situated at the centre of the spots. Figure 48b shows three typical scenarios on planar version of HB/HL after cell deposition: 1) the cells are at the centre, 2) the cell(s) is at the spot edge, 3) an extrusion from a cell is extending to next spot in the line. The most significant difference is that the cells are mostly intact, and obviously not penetrated by black silicon spikes. In that sense, the planar version on the HB/HL device is more gentle in terms of device-induced cell damage. Furthermore, these results confirm that the planar version of HB/HL works well as a selective single cell capture device when the spot size is appropriately designed.

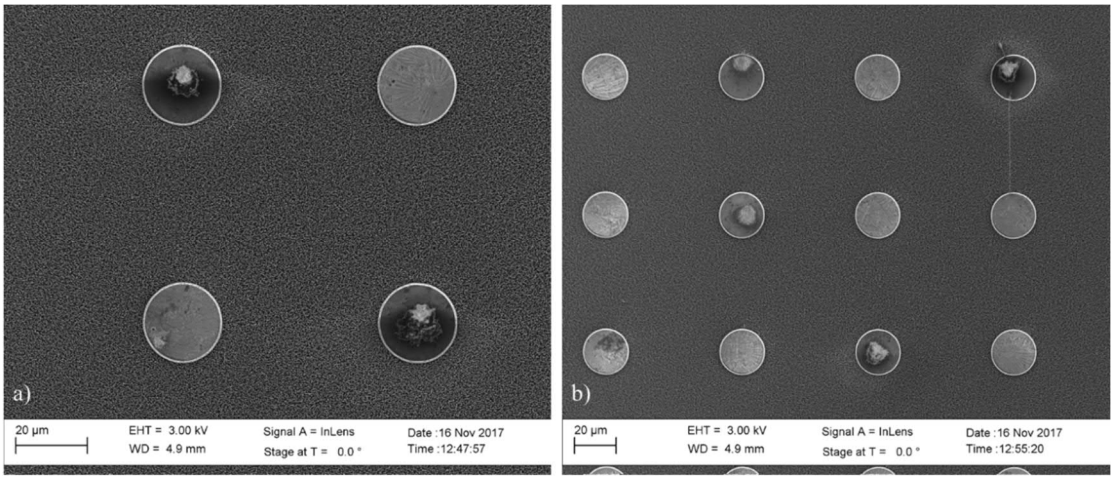

Figure 48: SEM image of THP-1 cells deposited on hydrophilic planar-Si spots. a) THP-1 cells retain their spherical shape and are centered with respect to the spot. b) In planar-Si spots, the cell extrusions are less prevalent in comparison to b-Si spots.

Additional spot geometries were tested. Figure 49 shows two elliptical spots, both containing a single cell. The ellipse dimensions are roughly 10 µm measured at widest point, and 40 µm measured at the tallest point. The seeding direction in figure 49 is from bottom to up. Curiously, both cells have partly adopted the underlying spot geometry, while completely remaining within the hydrophilic spot boundaries. Intuitively by examining the image, it appears that that the cells have slid on the surface, and pressed against the spot edges. However, this is not always the case, since most of the cells remain at the centre of a circular spot. Another possible scenario is that the cells have adopted the form upon the initial contact with the surface. Should the slide scenario be more prevalent, it would mean that more cells should be at the spot edges, which is not the case in the circular spots.

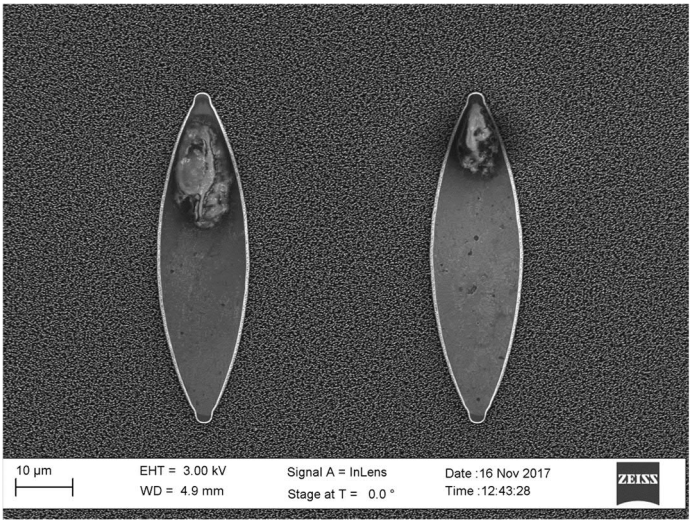

Figure 49: SEM image of deposited THP-1 cells using elliptical hydrophilic planar-Si spots. The maximum width of the ellipse is 10 µm and maximum length is 20 µm. Seeding direction is from bottom to top. THP-1 cells have adopted the underlying planar shape in this observation.

6.3.4. Single cell capture using THP-1 cell line and planar silicon with 4x pitch (experiment 4).

The fourth round of experiments replicated third round experiments, except the spot pitching was doubled from 2x to 4x. The calculations of occupancy rate distribution for 20 µm and 22 µm spots are presented in figure 50. Again the occupancy rate decreases when velocity increases, until at 70 mm / min goes up a notch. This is consistent with rounds two and three. Regression analysis does not support linear relationship (coefficient of determination confidence intervals from 0 to 0.98). The difference in occupancy rate between 20 and 22 µm spot is not statistically significant either since the error bars are overlapping (figure 50). Furthermore, any cell extrusions that occurred at low seeding

velocities did not reach the consequent spot in line in 4x pitching, instead the extrusions were curled randomly on the hydrophobic region. These results are consistent with the round two and three by confirming that the relationship is non-linear with this seeding velocity interval. Instead, the distribution appears uniform over the interval. According to Wilcoxon rank sum test the occupancy rate difference between experiment round three and four is statistically significant with p-value 0.008 (one-sided test). This result suggest that the 4x (median 13 %) pitching enables higher single cell occupancy rates in comparison to 2x pitching (median 7.0 %) when spot size is 20 µm.

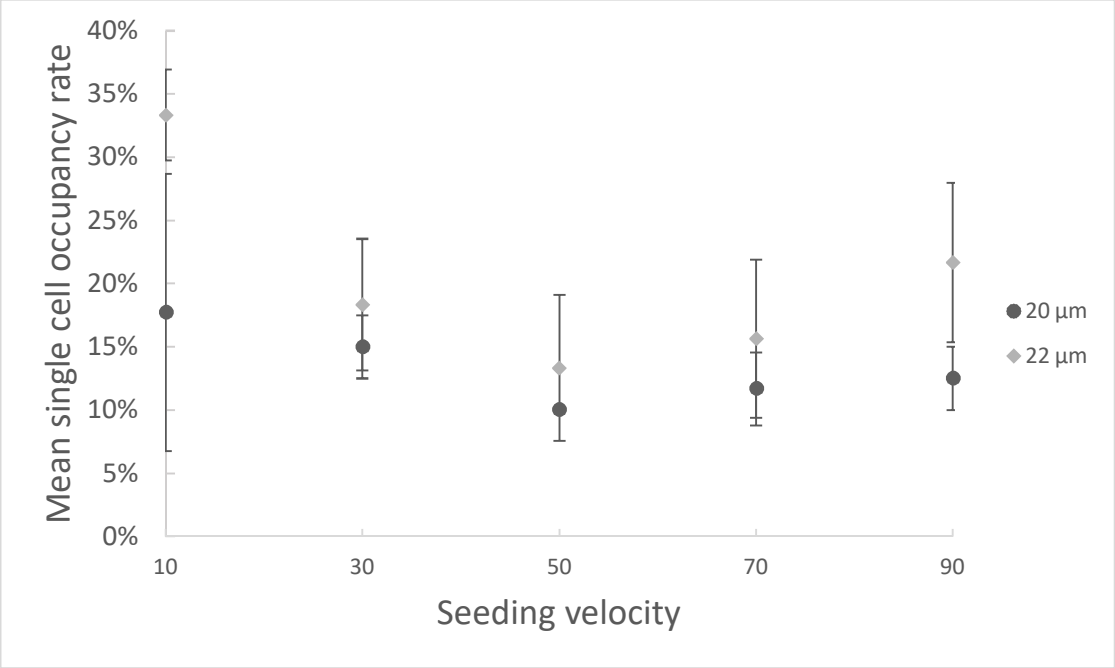

Figure 50: Physical experiment of mean single cell occupancy rate as a function of seeding velocity using hydrophilic planar-Si spots with 4x pitch. Seeding velocty do not demonstrate systematic linear dependence. There is mean difference between occupancy rates using 20 µm and 22 µm spots, but it is not statistically significant.

6.3.5. Single cell capture using THP-1 cell line and black silicon (experiment 5).

Fifth round of experiments replicated experiment round three and four. However, instead on using planar version of HB/HL, an all-black silicon HB/HL was used to study the effect of black silicon nanograss to THP-1 cell line cells. That is, the results between experiments three, four, and five are comparable. Figure 51 presents a collection of images where THP-1 cells are deposited on 22 µm spots using different seeding velocities (from a) to e), 10, 30, 50, 70, and 90 mm/min, respectively). Curiously, it appears clear that the velocity effect is now opposite in comparison to results from experiment three

and four, i.e., the occupancy rate is lowest at low velocity (figure 51a) and highest at highest velocity (figure 51e).

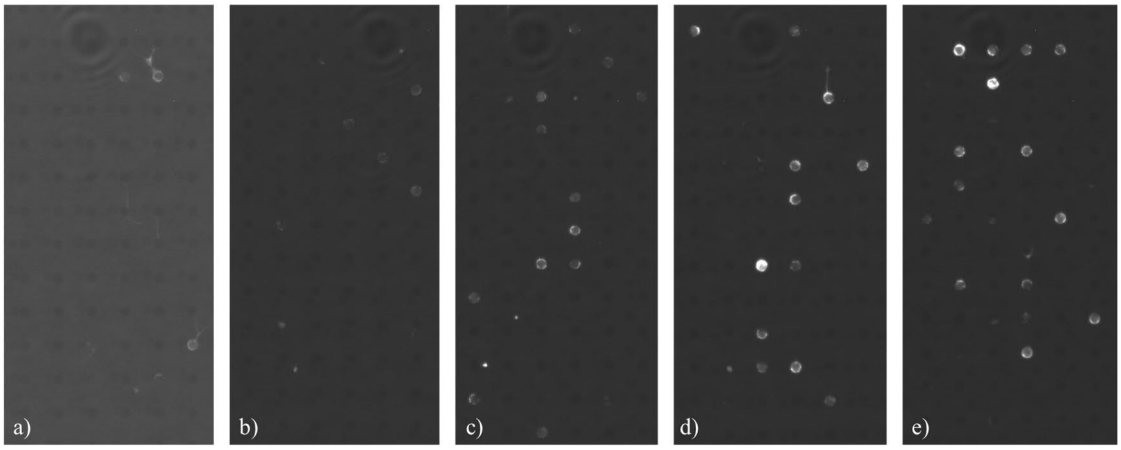

Figure 51: Fluorescent microscopy images of THP-1 cells deposited on 22 µm hydrophilic b-Si spots. a) 10 mm/min seeding velocity. b) 30 mm/min seeding velocity. c) 50 mm/min seeding velocity. d) 70 mm/min seeding velocity. e) 90 mm/min seeding velocity. Occupancy rate demonstrates clear increase as the seeding velocity increases.

Regression analysis plot is presented in figure 52. The slope regression coefficient is 0.3 (CI 0.2 : 0.38) and it is statistically significant with p-value 0.002. The interpretation is that when seeding velocity is increase by one, the occupancy rate increases by 0.3 within this seeding velocity interval. The coefficient of determination is extremely high 0.97 (CI 0.95 : 0.99) which indicates that in this experimental setting, the seeding velocity is critical factor affecting to the occupancy rate. This results supports that the relationship is linear and that the process can be systematically controlled by adjusting the seeding velocity. However, the velocity effect modification is only 0.3, which sets the maximum obtainable occupancy rate to 27 % (at maximum seeding velocity).

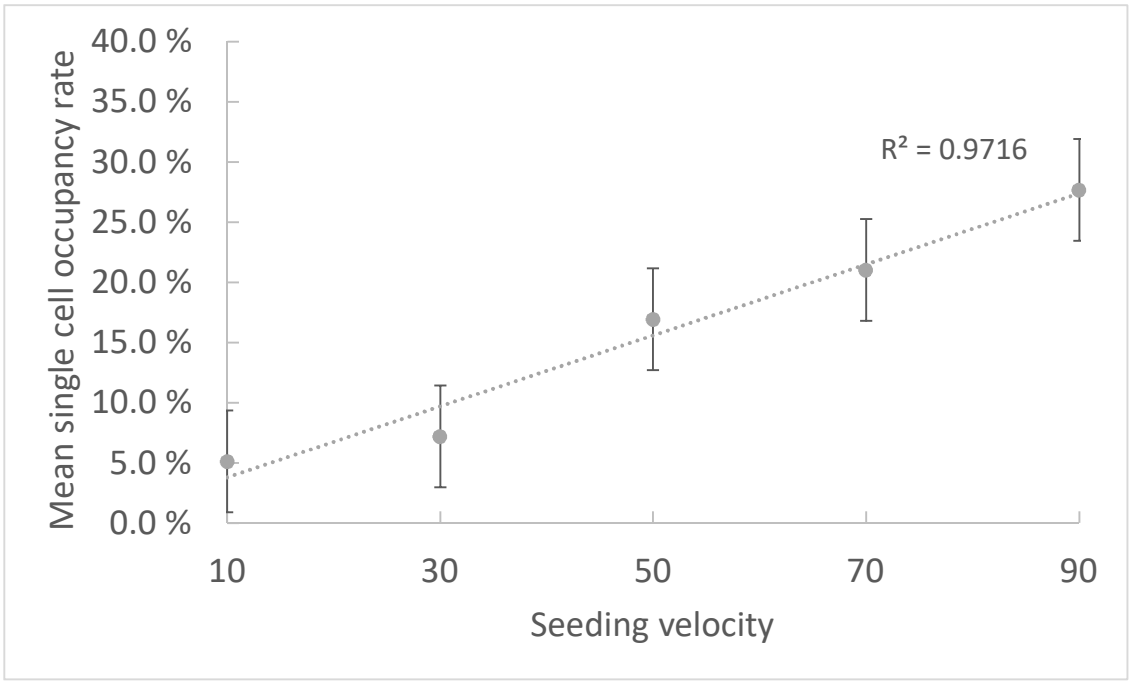

Figure 52: Physical experiment of mean single cell occupancy rate on 22 µm b-Si spots modeled with univariate linear regression using seeding velocity as predictor shows clear systematic linear dependence. Single cell occupancy rate increases when the seeding velocity increases.

Furthermore, this result obtained with b-Si is completely different in comparison to results obtained with the planar version in experiment 3 and 4. That is, the seeding velocity effect is linear when b-Si is used, but it is non-linear when planar version is used. Interestingly, in the cell capture experiment 1, the linear relationship is statistically significant, but the slope sign is opposite. The only *de facto* difference is that different cell types are used: healthy PBMC primary cells in round one, and THP-1 cancer cell line in experiment round 5. This could possibly be an interesting finding in terms of cell adhesion response to a well-defined surface, from cell biology perspective.

Another significant difference is that the THP-1 cells apparently spread to the entire spot area when the substrate is black silicon (figure 51), unlike when planar version of HB/HL is used, the THP-1 cells are mostly intact and spherical (figure 46 and 48). SEM images depicted in figure 53 shows that the cells are indeed filling the entire spot area. Furthermore, figure 53b shows that the THP-1 cells are possibly penetrated by the black silicon spikes. The black silicon induced mechanical damage could lead to cell lysis of THP-1 cells, similar to primary PBMC cells. Zooming closer to the edge of hydrophilic and hydrophobic area (figure 53a subset) reveals that some cell matter is extending to the hydrophobic part as thin lines. Curiously, the lines have propagated and extended via black silicon tips, analogous to suspension bridge connecting two cliff sides. The extensions are thin, roughly 100 nanometres. Typically, the thin extensions are at the spot proximity,

and have not reached other spots. Similar extension were not detected in the planar HB/HL version.

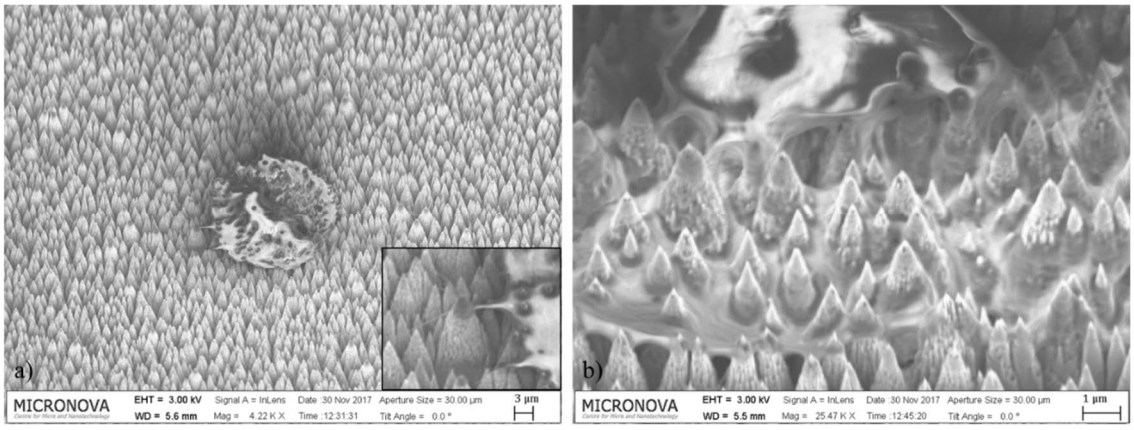

Figure 53: SEM images of THP-1 cell deposited on hydrophilic b-Si spot. a) THP-1 cell appears to adopt the circular shape of the spot and fill it entirely. Inset image of a) close-up image from the spot edge displaying cell extrusion extending to hydrophobic part. b) Close-up SEM image showing that the cell has most likely been penetrated by b-Si nano-spikes.

The difference in the response (opposite) to the seeding velocity between black silicon and planar silicon surfaces could possibly be attributed to the surface roughness. By analogy Velcro strip against a Velcro counterpart versus against a household mirror; even at relatively high velocities the Velcro would immobilize to the counterpart, and it would slip on a mirror. However, the Velcro could immobilize to the mirror surface with low velocities.

The cell surface is not smooth, instead it contains extensions, such as microvilli, used to initialize anchoring the endothelial cells in the blood circulation system. Furthermore, in the blood circulation system, the surface chemistry can be locally changed due to inflammation, for example, promoting cell adhesion and aggregation to that specific spot [70]. Thus, the planar silicon could mimic the blood vein wall in regular conditions allowing cells to slip on it, while black silicon surface could represent more a surface which promotes the cell adhesion to it. However, that alone does not explain the increase in the occupancy rate as a function of seeding velocity in the black silicon surface.

The increase could be attributed to the hypothesis about increased number of cells in the deposition region, i.e., at the receding edge (figure 17a and b). Based on the literature, the flow inside the seeding droplet is proportional to the forward velocity of the seeding droplet [52]. Thus, at higher velocities the absolute number of cells in the deposition region is increased, which could lead to the increased number of deposited cells in the black silicon HB/HL, since black silicon immobilizes cells effectively (cell spreading is an indicator

of this as well). The benefits of increased number of cells in the deposition region are possibly not realized in planar silicon HB/HL due to increased slipping effect at higher seeding velocities, i.e., decreased immobilization rate.

6.4. Summary of the results

The results are summarized in table 4 below. In the table 4 velocity column, the velocity value outside the brackets indicates the velocity that the best occupancy rate was obtained. The spot size value also refers to the spot size that the best OR was obtained.

Table 4: Summary of the results from the deposition experiments. Velocity value outside the brackets is the velocity which the best occupancy rate was achieved. Spot size and pitch values are the values which the best occupancy rate was achieved. Best occupancy is the best single-particle / single-cell occupancy rate achieved.

Experiment ID	**Cell / particle type**	**HB/HL**	**Velocity [mm/min]**	**Spot size [µm]**	**pitch**	**Best Occupancy**
P1	Polystyrene, 10 µm	b-Si	10 (100)	20	2x	27 %
P2	Polystyrene, 20 µm	b-Si	10 (100)	50	2x	54 %
C1	PBMC	b-Si	50 (10,30,70)	22	2x	19.5 %
C2	PBMC	b-Si	50 (10,30,70,90)	22	2x	24 %
C3	THP-1	planar-Si	10 (10,30,70,90)	20	2x	11.6 %
C4	THP-1	planar-Si	10 (10,30,70,90)	22	4x	33 %
C5	THP-1	b-Si	90 (10,30,70,90)	22	2x	27.7 %

Occupancy rates between the particle capture and cell capture do not show too radical differences, expect that 20 µm particles with 50 µm spots reached as high as 54 % occupancy rate. The lowest OR (11.6 %) was obtained with planar silicon version of HB/HL. Interestingly, by adjusting the spot pithing, the OR increased significantly when planar HB/HL was used to capture THP-1 cells. This difference was also statistically significant, according to Wilcoxon rank sum test. The 33 % (standard deviation 4 %) OR was highest obtained single cell occupancy rate in these experiments.

On average, the single cell occupancy rate was over 20 % which could be considered as a good result when compared to other single cell technologies. For example, in microwell based technologies [9, 44], the single cell occupancy rate was under 20 % at best. Droplet

microfluidics-based technologies typically remain in the 1% - 10 % single cell occupancy rate [8, 46]. Furthermore, the number of multiple cells on a spot was efficiently mitigated by adjusting the spot size, and similar single-to-double ratios was achieved than in comparable technologies [8, 9, 44, 46]. The underlying factor limiting the amount of cells per spot or well appears to stem simply from the size of the spot or well, therefore, microwell and hydrophilic spot designs share at least one common design rule.

The difference between b-Si and planar version single cell occupancy rate response to seeding velocity is curious. B-Si version show linear relationship between seeding velocity and occupancy rate, while planar version does not. That makes planar version less controlled design. One of the main difference in these designs is the surface roughness, which possibly causes the cell to slip and slide on planar silicon, while cell would stick and immobilize more easily on rough black silicon. On the other hand, while b-Si possibly immobilizes cell more efficiently, the mechanically induced damage to the cell could be a significant drawback. Planar version seems not to induce mechanical damage to the captured cells.

In summary, b-Si can reach up to 27 % occupancy rates with THP-1 cell line, and the occupancy rate can be controlled by adjusting seeding velocity. However, nanospikes possibly damage the cells and in the worst-case scenario prevents the use of b-Si as a single cell capture technology. Planar silicon version of HB/HL can reach up to 33 % single cell occupancy rates with THP-1 cell line, but the occupancy rate appears to not respond to the seeding velocity in a systematic fashion. The flat surface of planar silicon does not seem to induce any visible mechanical damage, which makes the planar silicon a more feasible candidate as a single cell capture technology in this comparison. The vacuum during SEM imaging most likely has some type of effect to cells. However, the cells were also imaged separately with microscope without going into vacuum and similar differences in terms of nano-spike penetration was observed which suggest that the conclusions from the SEM images are valid on those parts. Furthermore, the vacuum condition was same on all SEM imaging sessions and was not assumed to cause bias between the images in terms of environmental factor.

7. Conclusions

The aim of this thesis was to investigate feasibility of microfabricated patterned hydrophobic hydrophilic surface using black silicon and planar silicon as a single cell capture technology. The microfabrication process to manufacture patterned hydrophilic hydrophobic surface used here provided consistently functioning single particle / single cell capture devices. A specific 1-to-2 design rule, referring to cell size / spot size ratio, to limit the number of cells per spot to one was found to be a robust factor. The resulting single cell ratio to double cell ratio was at least as good as corresponding single cell capture technologies based on micro well technology. Hydrophilic spots used here were circular shaped; however, more exotic designs were also studied, and elliptical shaped spots provided excellent results in terms of selective single cell capture as well. The shape factor could possibly be further optimized in future.

A special seeding method was also developed in this thesis. The so-called active seeding method provided additional control to the overall efficiency of the HB/HL device. In the black silicon version of HB/HL, single cell occupancy rate responded linearly to the seeding velocity in such way that by decreasing the seeding velocity the resulting occupancy rate increased when PBMC (primary) cells was used. Interestingly, the response was opposite when THP-1 (cancer cell line) cells was used, i.e., the occupancy rate increased when seeding velocity was increased. Both results were statistically significant with 95% confidence interval. The underlying cause could be attributed to the different cell type, and thus difference in adhesion mechanism between the cells.

The active seeding method and the velocity control did not provide any statistically significant control over the occupancy rate efficiency when planar version of HB/HL was used. The seeding velocity did not demonstrate apparent improvement in terms of occupancy rate. However, the distance between the hydrophilic spots showed statistically significant difference in occupancy rate. Quadruple pitching resulted almost 40 % higher median occupancy rate in comparison to double pitching.

Black silicon version of HB/HL possibly induces mechanical damage and consequent cell lysis to the captured cell. This effect was observed from SEM images, where black silicon nanograss penetrated the cells. The cell penetration was not observed in planar silicon version. Instead, in planar silicon HB/HL, the cells appeared intact and non-spread in SEM images. This could possibly be a significant drawback for black silicon version.

However, to conduct single cell analysis, the captured cells would have to be lysed in any case to expose the RNA, thus the possible mechanical cell lysis could be advantageous in the best-case scenario. In that case, the cross contamination due to too early release of RNA should be investigated.

Nevertheless, significant drawback suffered by b-Si and planar version is the possibility of cross contamination in the actual single cell analysis which could be further boosted by the nanograss induced damage. In the microwell based technologies that is an issue which is continuously addressed. In the microwell base concept [9] one of the most significant invention is the stick-and-remove membrane which prevents the cross contamination. In this literature research here, no similar solutions were found for hydrophilic spot based technologies.

Thus, conducting single cell analysis with hydrophilic spot based technology is the next essential step to proceed toward functioning single-cell analysis device based on HB/HL. Simultaneously, new concepts and ideas to address cross contamination between the captured cells should be focused. Furthermore, the concrete approach to collect the mRNA from the captured and lysed cells is still unanswered. One possibility is to attach the oligonucleotides to the hydrophilic spots, which would require finding of a feasible linker between silicon / black silicon surface and the oligo tag. Such tag should also be cleavable from the surface once the mRNA is attached to the oligo, in order to harvest and conduct the single cell analysis.

This work provided proof of concept of microfabricated HB/HL capabilities of working as a single cell capture device. They display similar capture efficiency as current microwell and microfluidic based technologies. However, single-cell analysis was not performed, thus this work does not provide confirmation on the feasibility of HB/HL as a part of single-cell RNA-analysis protocol. Therefore, the next essential step is to conduct single cell analysis with the cells captured using this technology to obtain further proof of concept. That requires active development of series of protocols to capture the RNA with oligonucleotides after the cells are deposited on the HB/HL.

8. References

[1] Yuan, Guo-Cheng, et al. "Challenges and emerging directions in single-cell analysis." *Genome biology* 18.1 (2017): 84.

[2] Proserpio, Valentina, and Tapio Lönnberg. "Single-cell technologies are revolutionizing the approach to rare cells." *Immunology & Cell Biology* 94.3 (2016): 225-229.

[3] Saadatpour, Assieh, et al. "Single-cell analysis in cancer genomics." *Trends in Genetics* 31.10 (2015): 576-586.

[4] Sibo Zhu, et al. "Advances in single-cell RNA sequencing and its applications in cancer research." Oncotarget, 2017, Vol. 8, (No. 32), pp: 53763-53779.

[5] Khoo, Bee Luan, et al. "Single-cell profiling approaches to probing tumor heterogeneity." *International journal of cancer* 139.2 (2016): 243-255.

[6] Chung, Woosung, et al. "Single-cell RNA-seq enables comprehensive tumour and immune cell profiling in primary breast cancer." *Nature communications* 8 (2017): 15081.

[7] Rapolas Zilionis, et al. "Single-cell barcoding and sequencing using droplet microfluidics." Nature Protocols. Vol. 12 No. 1. 2017.

[8] Macosko, Evan Z., et al. "Highly parallel genome-wide expression profiling of individual cells using nanoliter droplets." Cell 161.5 (2015): 1202-1214.

[9] Todd M Gierhan, et al. "Seq-well: portable, low-cost RNA sequencing of single cell ar high throughput." Nature Methods. Vol. 14 No.4. 2017.

[10] Jacqueline R. Rettig and Albert Folch. "Large-scale single-cell trapping and imaging using microwell arrays." Anal. Chem. 2005, 77, 5628-5634.

[11] Pierre-Gilles de Gennes, Francoise Brochard-Wyart, David Quere. "Capillarity and Wetting Phenomena: Drops, Bubbles, Pearls, Waves." ISBN-13: 978-0387005928.

[12] Luuk. K. Koopal. "Wetting of Solid Surfaces: fundamentals and charge effects." Advances in Colloid and Interface Science 179-182 (2012) 29-42.

[13] Malcom E. Schrader. Young-Dupre Revisited. Langmuir 1995, 11, 3585-3589

[14]] R.E. Johnson and R.H. Dettre, "Contact Angle Hysteresis II. Contact Angle Measure-ments on Rough Surfaces", in: F.M. Fowkes (ed.), Contact Angle, Wettability,

and Adhesion, pp. 136–144, Advances in Chemistry Series 43, American Chemical Society, Washington D.C., 1964.

[15] Bormashenko, Edward Yu.. (2013). “Wetting of Real Surfaces – Bullets”. (pp. 71). De Gruyter

[16] A. B. D. Cassie and S. Baxter. ”Wettability of Poroous Surfaces.” 1944. Royal Society of Chemistry.

[17] Aurélie LaFuma and David Quéré. “Superhydrophobic states.” Nature Materials, Vol 2, JULY 2003.

[18] Kerstin Koch, et al. “Fabrication of Artificial Lotus leaves and significance of hierarchical structure for superhydrophobicity and low adhesion.” Soft Matter, 2009, 5, 1386 – 1393.

[19] Hans J. Ensikat. “Superhydrophobicity in perfection: the outstanding properties of the lotus leaf.” Beilstein J Nanotechnol. 2011; 2: 152–161.

[20] W. Barthlott, C. Neinhuis. “Purity of the sacred lotus, or escape from contamination in biological surfaces.” Planta (1997) 202: 1±8.

[21] Sami Franssila. “Introduction to Microfabrication”. ISBN:9781119990413. DOI:10.1002/9781119990413. 2010.

[22] Qi, Dianpeng, et al. "Simple approach to wafer-scale self-cleaning antireflective silicon surfaces." Langmuir 25.14 (2009): 7769-7772.

[23] Sainiemi, Lauri, et al. "Non-reflecting silicon and polymer surfaces by plasma etching and replication." Advanced materials 23.1 (2011): 122-126.

[24] Gilman, John J. "Direct measurements of the surface energies of crystals." Journal of applied physics 31.12 (1960): 2208-2218.

[25] Song, Dong, et al. "Selectively splitting a droplet using superhydrophobic stripes on hydrophilic surfaces." Physical Chemistry Chemical Physics 17.21 (2015): 13800-13803.

[26] Macdougall, G., and C. Ockrent. "Surface energy relations in liquid/solid systems I. The adhesion of liquids to solids and a new method of determining the surface tension of liquids." Proc. R. Soc. Lond. A 180.981 (1942): 151-173.

[27] Chang, Bo, et al. "Sliding droplets on hydrophilic/superhydrophobic patterned surfaces for liquid deposition." Applied Physics Letters 108.15 (2016): 154102.

[28] Li, Huizeng, et al. "Splitting a droplet for femtoliter liquid patterns and single cell isolation." ACS applied materials & interfaces 7.17 (2015): 9060-9065.

[29] Chen, Daniel S., and Mark M. Davis. "Molecular and functional analysis using live cell microarrays." Current opinion in chemical biology 10.1 (2006): 28-34.

[30] Uttamchandani, Mahesh, et al. "Small molecule microarrays: recent advances and applications." Current opinion in chemical biology 9.1 (2005): 4-13.

[31] Hacia, Joseph G., et al. "Determination of ancestral alleles for human single-nucleotide polymorphisms using high-density oligonucleotide arrays." Nature genetics 22.2 (1999): 164.

[32] Dufva, Martin. "Introduction to microarray technology." DNA Microarrays for Biomedical Research. Humana Press, 2009. 1-22.

[33] Heller, Michael J. "DNA microarray technology: devices, systems, and applications." Annual review of biomedical engineering 4.1 (2002): 129-153.

[34] Caroline Thureau. An overview of Illumina's Microarrays Product used in Clinical Settings. 2010. Seminar presentation.

[35] Fischer, Daniel. "On Statistical Methods in Prostate Cancer Genomics." Academic dissertation. University of Tampere. (2017). ISBN 978-952-93-8212-5

[36] Wang, Daojing, and Steven Bodovitz. "Single cell analysis: the new frontier in 'omics'." Trends in biotechnology 28.6 (2010): 281-290.

[37] Chen, Chun-Liang, et al. "Single-cell analysis of circulating tumor cells identifies cumulative expression patterns of EMT-related genes in metastatic prostate cancer." The Prostate 73.8 (2013): 813-826.

[38] McHale, Cliona M., et al. "Analysis of the transcriptome in molecular epidemiology studies." Environmental and molecular mutagenesis 54.7 (2013): 500-517.

[39] Heath, James R., Antoni Ribas, and Paul S. Mischel. "Single-cell analysis tools for drug discovery and development." Nature reviews Drug discovery 15.3 (2016): 204.

[40] Mata, Alvaro, Aaron J. Fleischman, and Shuvo Roy. "Characterization of polydimethylsiloxane (PDMS) properties for biomedical micro/nanosystems." Biomedical microdevices 7.4 (2005): 281-293.

[41] Merckmillipore.com. (2018). Validated Cell Types with Scepter™ 2.0 Cell Counter | Life Science Research | Merck. [online] Available at: http://www.merckmillipore.com/FI/en/life-science-research/cell-analysis-flow-cytometry/scepter-cell-counter/validated-cell-types/VIib.qB.VKQAAAFApA4.1ab8,nav?ReferrerURL=https%3A%2F%2Fwww.google.fi%2F

[42] Morin, Ryan D., et al. "Profiling the HeLa S3 transcriptome using randomly primed cDNA and massively parallel short-read sequencing." Biotechniques 45.1 (2008): 81.

[43] Illumina.com. (2018). Ultra-Low-Input and Single-Cell RNA-Seq. [online] Available at: https://www.illumina.com/techniques/sequencing/rna-sequencing/ultra-low-input-single-cell-rna-seq.html

[44] Bose, Sayantan, et al. "Scalable microfluidics for single-cell RNA printing and sequencing." Genome biology 16.1 (2015): 120.

[45] Teh, Shia-Yen, et al. "Droplet microfluidics." Lab on a Chip 8.2 (2008): 198-220.

[46] Rotem, Assaf, et al. "High-throughput single-cell labeling (Hi-SCL) for RNA-Seq using drop-based microfluidics." PloS one 10.5 (2015): e0116328.

[47] Ishizaki, Takahiro, Nagahiro Saito, and Osamu Takai. "Correlation of cell adhesive behaviors on superhydrophobic, superhydrophilic, and micropatterned superhydrophobic/superhydrophilic surfaces to their surface chemistry." *Langmuir* 26.11 (2010): 8147-8154.

[48] Jogia, Gabriella E., et al. "Droplet Microarray Based on Superhydrophobic-Superhydrophilic Patterns for Single Cell Analysis." Microarrays 5.4 (2016): 28.

[49] Feng, Wenqian, et al. "Surface Patterning via Thiol-Yne Click Chemistry: An Extremely Fast and Versatile Approach to Superhydrophilic-Superhydrophobic Micropatterns." Advanced Materials Interfaces 1.7 (2014).

[50] Talbot, E. L., et al. "Evaporation of picoliter droplets on surfaces with a range of wettabilities and thermal conductivities." Physical Review E 85.6 (2012): 061604.

[51] Dufour, Renaud, et al. "Zipping effect on omniphobic surfaces for controlled deposition of minute amounts of fluid or colloids." Small 8.8 (2012): 1229-1236.

[52] Li, Zhen, et al. "Three dimensional flow structures in a moving droplet on substrate: A dissipative particle dynamics study." Physics of Fluids 25.7 (2013): 072103.

[53] Karbalaei, Alireza, Ranganathan Kumar, and Hyoung Jin Cho. "Thermocapillarity in microfluidics—a review." Micromachines 7.1 (2016): 13.

[54] Xu, Xuefeng, Jianbin Luo, and Dan Guo. "Radial-velocity profile along the surface of evaporating liquid droplets." Soft Matter 8.21 (2012): 5797-5803.

[55] Deegan, Robert D., et al. "Capillary flow as the cause of ring stains from dried liquid drops." Nature 389.6653 (1997): 827.

[56] Levin, David A., and Yuval Peres. Markov chains and mixing times. Vol. 107. American Mathematical Soc., 2017.

[57] Sainiemi, Lauri, et al. "Non-reflecting silicon and polymer surfaces by plasma etching and replication." Advanced materials 23.1 (2011): 122-126.

[58] Jaccodine, R. J. "Surface energy of germanium and silicon." Journal of The Electrochemical Society 110.6 (1963): 524-527.

[59] Microchemicals.com. (2018). Photoresist AZ 4562 Photoresists MicroChemicals GmbH. [online] Available at: https://www.microchemicals.com/products/photoresists/az_4562.html

[60] Paavo R. Automated Image Analysis of Single-cell Trapping Occupancy Rate Using K-Means clustering and K-nearest neighbouring algorithms with R. 2017.

[61] ThermoFischer. (2018). [online] Available at: https://www.thermofisher.com/order/catalog/product/C34552 [Accessed 29 Mar. 2018].

[62] Orflo Technologies. Blood Cell Analysis with the Moxi Z. Application note. 2011.

[63] Zhang, Hongyan, et al. "A size amplified immune magnetic microbeads strategy in the rapid detection of circulating tumor cells." Chemical Communications 50.53 (2014): 7024-7027.

[64] Lawrence, Michael B., et al. "Threshold levels of fluid shear promote leukocyte adhesion through selectins (CD62L, P, E)." The Journal of cell biology 136.3 (1997): 717-727.

[65] Simon, Scott I., and Harry L. Goldsmith. "Leukocyte adhesion dynamics in shear flow." Annals of biomedical engineering 30.3 (2002): 315-332.

[66] Dong, Cheng, and Xiao X. Lei. "Biomechanics of cell rolling: shear flow, cell-surface adhesion, and cell deformability." Journal of biomechanics 33.1 (2000): 35-43.

[67] Marie-Dominique Filippi. Mechanism of Diapedesis: Importance of the Transcellular Route. Advances in Immunology. Volume 129, 2016, Pages 25-53.

[68] Brown, Robert B., and Julie Audet. "Current techniques for single-cell lysis." Journal of the Royal Society Interface 5.Suppl 2 (2008): S131-S138.

[69] Ivanova, Elena P., et al. "Bactericidal activity of black silicon." Nature communications 4 (2013): 2838.

[70] Granger DN, Senchenkova E. Inflammation and the Microcirculation. San Rafael (CA): Morgan & Claypool Life Sciences; 2010.